KU LEUVEN

ARENBERG DOCTORAL SCHOOL
Faculty of Engineering Science

Active control of turbulent axisymmetric jets using zero-net-mass-flux actuation

Asim Önder

Supervisor:
Prof. dr. ir. Johan Meyers

Dissertation presented in partial
fulfillment of the requirements for the
degree of Doctor in Engineering

December 2014

Active control of turbulent axisymmetric jets using zero-net-mass-flux actuation

Asim ÖNDER

Examination committee:
Prof. dr. ir. Carlo Vandecasteele, chair
Prof. dr. ir. Johan Meyers, supervisor
Prof. dr. ir. Eric v.d. Bulck, co-supervisor
Prof. dr. Moritz Diehl
Prof. dr. ir. Stefan Vandewalle
Prof. dr. ir. Rob J.M. Bastiaans
(Technische Universiteit Eindhoven)
Prof. dr. ir. Joris Degroote
(Universiteit Gent)

Dissertation presented in partial fulfillment of the requirements for the degree of Doctor in Engineering

December 2014

Uitgegeven in eigen beheer, Asim Önder, Celestijnenlaan 300 box 2421, B-3001 Heverlee (Belgium)

ISBN 978-94-6018-934-0
D/2014/7515/157

Preface

This thesis is the result of my PhD research at the Division of Applied Mechanics and Energy Conversion (TME) of the Department of Mechanical Engineering, KU Leuven. It studies the control of a fundamental turbulent flow with state-of-the-art numerical methodologies. I have been fascinated with turbulent flows ever since I took the first course on the topic during my master studies in Germany. Therefore, I truly enjoyed working on this PhD project, which deals with many aspects of turbulent flows in great detail. Despite my strong interest, finishing this thesis would be impossible without the precious help and advise of the following people.

First of all, I am deeply grateful to my supervisor, Prof. Johan Meyers, for giving me the opportunity to work on this interesting PhD project. He was generous in spending time for my guidance, and I benefited tremendously from his problem-solving skills and his insightful analyses. He was in full understanding of complexities concerning the topic, and was aware of very long turnaround times. Therefore, he was always patient and supportive. I really appreciate this. I am also grateful that he gave me the freedom to explore new research directions. With his immense knowledge, he helped me to find my way in these new directions and eventually come up with new research ideas. Furthermore, he also played a key role in my growing as a scientist, as I learned a lot from him about scientific writing, and presenting the essence of the scientific material.

I would like to thank also my co-promoter Prof. Eric van den Bulck and Prof. Maarten Vanierschot for our insightful meetings on jet-flow control with synthetic jets. These meetings significantly increased my understanding of the practical side of the problem.

I would like to extend my gratitude to all members of my examination committee for spending their valuable time to rigorously revise my text. Their comments and suggestions definitely improved the overall quality of the work.

This project would be impossible without the support of Geert Jan Bex, Jan Ooghe, Martijn Oldenhof and Ingrid B. Roig from ICTS department in Leuven and people from *Tier1* help-desk in Gent. I'm truly grateful that they gave me the opportunity to become a pilot user on the Flanders' first *Tier1* supercomputer in Gent, and afterwards on the new *Tier2* infrastructure in Leuven. They always responded quickly to my problems, and assisted me patiently throughout my intensive HPC calculations.

It was a pleasure for me to work at TME and to meet many friendly, fun and inspiring colleges. I am grateful to all of them for these incredible years and for their friendship. In particular, I would like to thank to the current and former members of TFSO group, and my current and former officemates. I have to mention especially the names of Vladimir, Jay, Sara, Peng, Shijie, Joris, Lieven and Ruben, as I'm truly indebted to them for their direct contributions to my research. I am also grateful to Geert and Dries for translating my abstract to Dutch. Furthermore, I would like express my sincere gratitude to Kathleen, Frieda, and Valerie for being very helpful in administrative matters.

I've been fortunate to have a great group of friends during my stay in Belgium. The list is long but I have to particularly thank Korcan, M.Ali, Deniz, Onur K., Onur A., Zeynep, Emre, Ercan and Taylan for being good companions over these years. I also would like to thank all members of Beverly P. (especially Nico and Partick for introducing me to the team), and all members of Ball B. I greatly enjoyed the friendly sports environment and team-building activities.

Last but not least, my deep appreciation goes to all my family members, especially my sister Ceren, my brother Can and my cousin Gizem, for their understanding of my absence for this PhD study abroad, and for their support in many ways. Most importantly, I owe my deepest gratitude to my parents Gonca Önder and Süleyman Önder for the continuous and unconditional trust, patience, support and love they showed me over the years. This thesis is dedicated to them.

Asim Önder
Leuven, December 2014

Abstract

Turbulent axisymmetric jets are found in many environmental and technological flows. This wide range of applicability has triggered numerous studies on jet-flow control over the years. A topic of major interest has been increasing the mixing rate between the injected fluid and stagnant ambient fluid around the jet, with, e.g., possible applications towards cleaner combustion with less carbon emissions, or more efficient pollutant and waste-water discharge. An effective approach to enhance the jet mixing is using active flow control with unsteady actuators with the aim to manipulate dynamic vortical features dominating the mixing. Such controls can be driven in frequency regimes where the jet is most sensitive, and therefore yield better performance with an order of magnitude less energy consumption than steady blowing or suctioning actuators.

In this dissertation, a flexible, high-bandwidth active control method is studied using zero-net-mass-flux (ZNMF) actuators. The primary objective is to enhance the mixing properties in axisymmetric jet flows. ZNMF fluidic actuators are highly attractive, as they don't require any external fluid source, and are cheap, easy-built and lightweight. The main challenge for the applicability of these tools in jet flow control is the intricate interaction of the control means (miniature vortex rings shed with the actuation frequency) with the main jet flow. The understanding on control effects resulting from this interaction is still very limited. Therefore, the optimal configurations for a better performance is yet to be explored. In order to gain more insight about control mechanisms and improve the mixing properties, a numerical flow control and optimization framework is developed in OpenFOAM®, and ZNMF-actuated axisymmetric jets are extensively studied using high-fidelity DNS simulations.

In the first part of this dissertation, the focus was on computational improvements in OpenFOAM®. The transient solver based on the iterative PISO scheme is replaced with a classical non-iterative incremental projection scheme. This modification allowed a 45% cost reduction in time-stepping while keeping the same order of accuracy in velocity fields. Furthermore, a parallelization of statistical averaging in DNS simulations was proposed to enhance OpenFOAM®'s applicability on high performance computers, and overcome scaling issues. The method is based on ensemble averaging applied on a set of statistically independent simulations, and yields about 20% performance improvement on 624 processors.

In a second part, a set of DNS simulations of a low-speed round jet at $\Re_D = 2000$ are performed using various actuation frequencies. Three ZNMF actuators are driven in phase, and modelled using sinusoidal velocity boundary conditions on small elliptic regions located in the surrounding wall of the jet orifice. These actuation regions have an area of around 0.5% of the jet inlet cross-section. The actuation velocity is selected to be equal to the inlet velocity of the jet, which produced an actuation with a momentum ratio of 0.49%. ZNMF actuation is capable of introducing significant changes to the flow despite this very low momentum ratio. Hexagram-like flow patterns resulting from the control-main flow interaction are identified. Two mechanisms lead to these patterns, i.e., (i) self-deformation of the jet's primary vortex rings initiated by the intrusion of miniature vortex rings, and (ii) production of side jets by the development and subsequent detachment of secondary streamwise vortex pairs. The control effect is strongest when the jet is actuated with the jet preferred mode. Such an actuation yields favourable changes in key mixing measures like entrainment and centreline decay rate. However, increased coherence in the flow is observed to delay the fine-scale transition, and can be detrimental to molecular mixing. Furthermore, high frequency actuation is found to suppress the mechanisms leading to large-scale structure growth and turbulent kinetic energy production. Thus, high-frequency ZNMF actuation can be beneficial for jet-noise reduction, and therefore can be interesting for further research.

In the last part of this dissertation, multi-frequency actuation is investigated by conducting an optimal distributed control study to maximize enstrophy. Controls are modelled as twelve small forcing regions, that are distributed evenly around the jet circumference. A gradient-based optimizer using the continuous adjoint method and DNS simulations is developed in OpenFOAM®. As this study is the first application for the optimization of unsteady flows in OpenFOAM®, particular attention is paid to the presentation of mathematical and algorithmic details. Additionally, the limitation of the adjoint methodology for chaotic and noise-amplifier flows like turbulent jets is addressed. Optimizations are conducted for two different initial conditions up to around ten outer iterations, and improved mixing of about 10% is obtained. Optimized control signals are found to be composed of additional low value multi-frequency components, and they produce flow fields with slightly enhanced irregularity and mixedness.

Beknopte samenvatting

Turbulente axisymmetrische straalstromingen komen vaak voor in het milieu of in technologische toepassingen. Het brede toepassingsgebied van deze stromingen leidde tot talrijke studies over de controle van straalstromingen. Van groot belang is het verhogen van de mengsnelheid tussen het geïnjecteerde fluïdum en het rond de straalstroming stilstaande omgevingsfluïdum, bijvoorbeeld voor praktische doeleinden zoals een zuiverdere verbranding met minder koolstofemissies of een efficiëntere lozing van polluenten en afvalwater. Een efficiënte manier om de menging te bevorderen, is het aanwenden van actieve stromingscontrole via tijdsvariërende actuatoren met als doel de dynamische vortexfenomenen die de menging domineren, te manipuleren. Zulke actuatoren kunnen gestuurd worden in frequentieregimes waar de straalstroming het meest gevoelig is en leveren daaarom een betere performantie op met een ordegrootte minder energieverbruik dan stationaire blaas- en zuigactuatoren.

In dit proefschrift wordt een flexibele hoge-brandbreedte actieve controlemethode bestudeerd, op basis van 'zero-net-mass-flux' (ZNMF) actuatoren. Het primaire objectief is de mengingseigenschappen in axisymmetrische straalstromingen te verbeteren. ZNMF fluïdische actuatoren zijn erg aantrekkelijk vermits ze geen enkele externe fluïdumbron vereisen. Bovendien zijn ze goedkoop, eenvoudig op te bouwen en licht van gewicht. De voornaamste uitdaging voor de toepasbaarheid van deze tools in straalstromingscontrole is de complexe interactie van de controlemiddelen (miniscule vortexringen afgestoten met de actuatiefrequentie) met de hoofdstroom. Het huidige begrip inzake controle-effecten resulterend uit die interactie is erg beperkt. Daarom zullen optimale configraties voor een betere performantie nog onderzocht moeten worden. Om meer inzicht te winnen rondom de controlemechanismen en de mengingseigenschappen te verbeteren, wordt een numeriek kader voor stromingscontrole- en optimalisatie in OpenFOAM® ontwikkeld en worden ZNMF geactueerde axisymmetrische straalstromingen intensief bestudeerd op basis van hoog betrouwbare DNS-simulaties.

In het eerste gedeelte van dit proefschrift ligt de focus op computationele verbeteringen in OpenFOAM®. De transiënte solver gebaseerd op het iteratieve PISO-schema werd vervangen door een klassiek niet-iteratief incrementeel projectieschema. Deze aanpassing maakt een kostreductie in tijdstappen van vijfenveertig procent mogelijk, terwijl dezelfde orde van nauwkeurigheid in de snelheidsvelden behouden blijft. Bovendien werd een parallellisatie van statistische uitmiddeling in DNS-simulaties voorgesteld om de toepasbaarheid van OpenFOAM® op hoog performante computers te bevorderen en schaalbaarheidsproblemen te overkomen. De methode is gebaseerd op ensemble uitmiddeling toegepast op een set van statische onafhankelijke simulaties, en resulteert in een performantietoename van ongeveer twintig procent op 624 processoren.

In het tweede gedeelte wordt een reeks DNS-simulaties van een lage-snelheids ronde straalstroming uitgevoerd op $\Re_D = 2000$, voor verschillende actuatiefrequenties. Drie ZNMF actuatoren wordt in fase aangestuurd en gemodelleerd via sinusoïdale snelheidsrandvoorwaarden op elleptische zones gelegen in de omgevende wand van de opening. Deze actuatiezones hebben een oppervlakte van ongeveer een halve procent van de inlaatdoorsnede. De actuatiesnelheid wordt gelijk aan de inlaatsnelheid van de straalstroming gekozen, hetgeen een actuatie met een momentumverhouding van 0.49 procent voorbrengt. ZNMF actuatie laat toe significante veranderingen aan de stroming te introduceren, ondanks deze zeer lage momentumverhouding. Hexagramachtige stromingspatronen resulterende uit de interactie tussen controle en hoofdstroom zijn identificeerbaar. Twee mechanismen leiden tot deze patronen: (1) zelfdeformatie van primaire vortexringen in de straalstromingen, geinitieerd door de intrusie van miniscule vortexringen en (2) productie van ‘side jets’ door de ontwikkeling en vervolgens loshechting van secundaire stroomafwaartse vortexparen. Het controle-efect is het sterkst wanneer de straalstroming geactueerd wordt met de preferentiemode van de stroming. Een dergelijke actuatie resulteert in gunstige wijzigingen in belangrijke mengingsmaatstaven zoals meesleuring en centrumlijn afnamesnelheid. Er wordt echter ook een verhoogde coherentie in de stroming waargenomen die de fijne-schaal transitie uitstelt en nadelig kan zijn voor de moleculaire menging. Verder wordt vastgesteld dat de mechanismen die tot de groei van grote-schaal structuren en turbulente kinetische energieproductie leiden, onderdrukt worden door hoog frequentie actuatie. Bijgevolg kan hoog frequentie ZNMF actuatie voordelig zijn voor lawaaireductie en dus interessant zijn voor verder onderzoek.

In het laatste gedeelte van deze dissertatie, wordt multifrequentie acuatie onderzocht door een studie uit te voeren naar optimaal verdeelde controle om enstrofie te maximaliseren. De actuatoren worden gemodelleerd als twaalf kleine controlezones die gelijkmatig rondom de straalomtrek verdeeld

zijn. Een gradiëntgebaseerde optimalisator steunende op de continue adjoint methode en DNS-simulaties werd binnen OpenFOAM® ontwikkeld. Omdat deze studie de eerste toepassing is van optimalisatie van transiënte stromen in OpenFOAM®, wordt in het bijzonder aandacht geschonken aan de presentatie van mathematische en algoritmische details. Bovendien worden de beperkingen van de adjointmethodologie voor chaotische en ruisversterkende stromingen zoals turbulente straalstromingen behandeld. Optimalisaties worden uitgevoerd voor twee verschillende beginvoorwaarden tot ongeveer tien uitwendige iteraties en een verbetering in menging van ongeveer tien procent wordt verkregen. Geoptimaliseerde controlesignalen blijken te bestaan uit bijkomstige multi-frequentiecomponenten van lage waarde en produceren snelheidsvelden met een licht verbeterde onregelmatigheid en mengingstoestand.

Nomenclature

Acronyms

CFD	Computational Fluid Dynamics
DNS	Direct Numerical Simulation
KH	Kelvin–Helmholtz
LES	Large-Eddy Simulation
LU	Lower Upper
PDE	Partial differential equation
PISO	Pressure implicit with splitting of operator
QDR	Quad data rate
RANS	Reynolds-Averaged Navier–Stokes Equations
RMS	Root mean square
ZNMF	Zero-net-mass-flux

Greek Symbols

α	Angle between the jet axis and the actuator axis
ϕ	Control field
δt	Time step size
Δ	Filter width
Γ_i	Inlet boundary
Γ_o	Outlet boundary

Γ_r	Lateral boundary
Γ_w	Wall boundary
κ	Local entrainment rate
Ω	Domain of interest
Ω_c	Control domain
Ω_s	Sensor domain
$\partial\Omega$	Domain boundary
$\partial\Omega_c$	Control boundary
θ	Implicitness parameter
θ_0	Momentum thickness of the boundary layer
$\boldsymbol{\omega}$	Vorticity
$\boldsymbol{\xi}$	Adjoint velocity
$\boldsymbol{\phi}^h$	Discretized control field

Roman Symbols

$\dot{m}(x)$	Mass flux through transverse planes
$\mathcal{J}$	Cost functional
$\tilde{\mathcal{J}}$	Reduced cost functional
$\mathcal{L}$	Lagrangian
$\mathbf{g}$	Specified velocity on a Dirichlet boundary
$\mathbf{f}$	Body force
$\mathbf{u}$	Velocity
$\mathcal{F}_0$	Initial forcing
Ma	Mach number
Re_D	Reynolds number w.r.t. inlet diameter
St_θ	Strouhal number w.r.t. momentum thickness
St_D	Strouhal number w.r.t. inlet diameter

Sc	Schmidt number
St_{pm}	Jet preferred mode
$\tilde{\mathbf{u}}$	Intermediate velocity
$\boldsymbol{F}_c$	Reynolds-averaged total flux of the scalar quantity
$\boldsymbol{n}$	Normal of the boundary
c	Passive scalar
C_c	Passive scalar on the jet centreline
c_d	Specified passive scalar on a Dirichlet boundary
C_μ	Momentum ratio of the ZNMF actuator
D	Diameter of the jet inlet
E_g	Parallel efficiency of grid partitioning
f	Frequency
f_a	Actuation frequency
$G(\cdot)$	Gaussian filter kernel
H	Helicity density
k	Turbulent kinetic energy
k_c	Turbulent kinetic energy on the jet centreline
L	Length of the computational domain
m	Azimuthal wavenumber
p	Gauge pressure
P_{ns}	Projection operator for incompressible Navier–Stokes equations
Q	The second invariant of the velocity-gradient tensor
q	Adjoint pressure
R	Total number of members in an ensemble
S_g	Speed-up of grid partitioning

t	Time
T_d	Decorrelation timescale
T_i	Initialization timescale
T_s	Sampling timescale
U_a	Actuation amplitude
u_a	Actuation velocity
U_c	Axial velocity on the jet centreline
U_J	Inlet bulk velocity of the jet
u'_J	RMS of random perturbations

Subscripts

r	Radial direction
x	Axial direction

Miscellaneous Symbols

$\langle\cdot\rangle$	Ensemble averaging

Contents

List of Figures

List of Tables

Chapter 1

Introduction

The turbulent jet flow dispatched through an axisymmetric nozzle or orifice (cf. Figure 1.1) is a prototype for many flows in industrial applications such as combustion chambers, jet or auto–mobile engines, as well as for environmental flows such as jet streams in the atmosphere, and dispersion of pollutants. Because of this practical relevance, the jet flow has received considerable technological and scientific attention. Despite major interest, certain fundamental aspects about this representative free shear flow are yet to be understood. The precise nature of coherent structure interactions [8], the accurate prediction of noise sources [41] or the exact mechanisms for turbulent jet mixing [93] are just a few of the remaining puzzles. Consequently, studying the mechanisms in the flow and controlling them to achieve better flow properties are still a very exciting subject of research.

Among various flow control objectives, enhancing the turbulent mixing rate in jet flows is of prominent industrial importance. Augmentation of the mixing rate yields cleaner and more efficient combustion that can lead more economic designs emitting less environmentally hazardous pollutants. Mixing augmentation is a highly challenging nonlinear multi–scale control problem [35] where all relevant scales of turbulent motion should be properly addressed by controls. Large-scale events occur with characteristic low frequencies where fines scale motions are typically observed in high-frequency regimes.

Zero-net-mass-flux (ZNMF) or synthetic-jet actuators are fluidic actuators known for their high bandwidth capabilities [44], and therefore, they are promising tools for mixing enhancement studies. The fluid in a cavity is modulated using an oscillatory driver, e.g. an elastic diaphragm, attached to the bottom wall. Any control signal can easily be induced on the driver, and

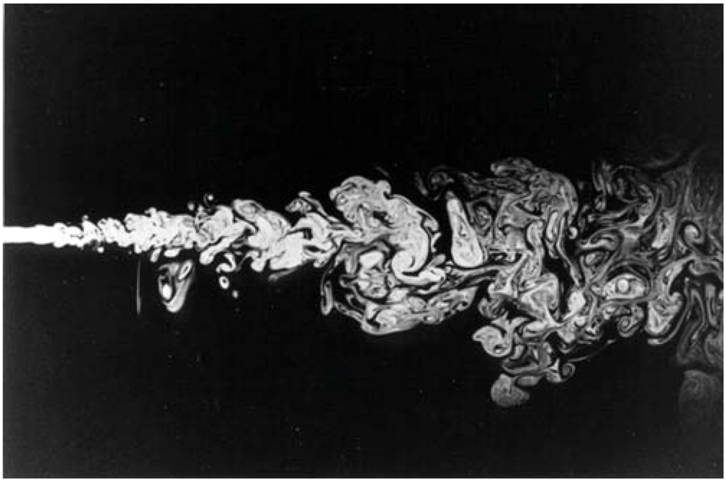

Figure 1.1: Cross-section of a turbulent axisymmetric jet flow visualized using Laser-induced fluorescence. The Reynolds number is approximately 2300. Reproduced from Dimotakis, Lye & Papantoniou [36].

complex waveforms can be produced. The operation of the device is illustrated in Figure 1.2a. When the driver expels the fluid upwards (cf. Ia in Figure 1.2a), the fluid is ejected through a thin slot or orifice at the top wall and a synthetic jet featuring a train of vortex rings is formed (cf. Ib in Figure 1.2a). During the suction phase, the mechanism is reversed. The driver increases the volume of the cavity (cf. IIa Figure 1.2a), produces low pressure in the cavity, and therefore the ambient fluid is entrained into the cavity from all directions surrounding the cavity wall (cf. IIb Figure 1.2a).

If ZNMF actuators are applied in jet-flow control, they can be placed where the jet is most sensitive to perturbations, e.g., around the jet inlet, and directed towards the main jet (cf. Figure 1.2b). In this control configuration, miniature vortex rings shedding with the control frequency, penetrate into the main jet and impose the control effect. The main challenge for the applicability of these fluidic ZNMF actuators is this intricate interaction of miniature vortex rings with the main jet flow. The understanding on control effects resulting from this interaction is very limited. Therefore, the optimal configurations for best performance is still to be explored.

In the current dissertation, we numerically study ZNMF oscillatory actuation to enhance mixing properties of turbulent axisymmetric jet flows. To this end, we perform Direct Numerical Simulation (DNS) studies of actuated axisymmetric jets using OpenFOAM®, an open–source Finite Volume library. OpenFOAM® is

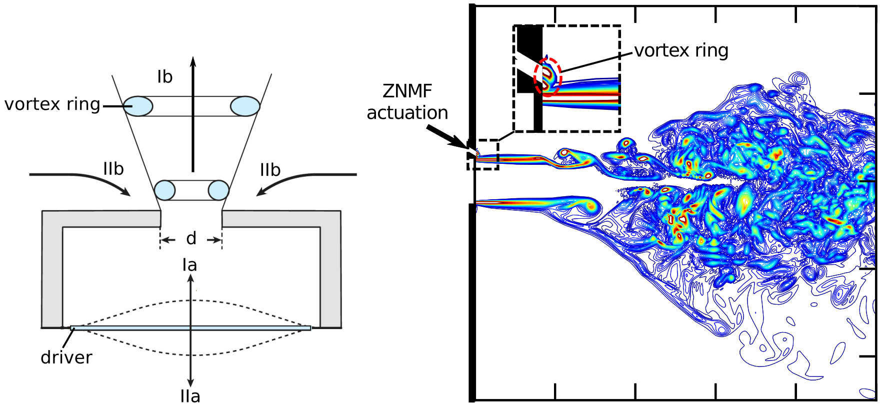

(a) ZNMF actuator (b) Jet control with ZNMF actuators

Figure 1.2: ZNMF actuator and its application to a turbulent jet. (a): Schematic diagram describing the working principle. Adapted from Cattafesta & Sheplak [24]. (b): DNS snapshot of a turbulent jet controlled with a numerically modelled ZNMF actuator. Actuator is in the blowing phase as it can be seen by an ejected miniature vortex ring. Image is adapted from Chapter 4.

a generic software package designed for unstructured grids. Thus, all the tools developed in the current study can be applied to more specialized industrial applications with complex geometries.

In a first phase, the research focuses on the development of a cost–effective numerical code for DNS of round jets. This computationally very demanding study required some improvements in OpenFOAM®. In a second phase, the response of round jet flows to multiple ZNMF actuation is analysed in detail. The focus of this phase is on the modification of vortex dynamics and transport properties. In the last phase, an attempt is made to increase the jet mixing by optimizing high-bandwidth signals. To this end, an optimizer using a continuous adjoint methodology is implemented into OpenFOAM®.

In the next sections, the context and goals of this study are elaborated. Firstly, the state-of-the-art in active flow control and optimization is given in Section 1.1, which is followed by a brief introduction to turbulent axisymmetric jet flows in Section 1.2. Subsequently, the jet-flow control efforts and synthetic jet actuators are reviewed in Section 1.3. Then, the need for optimization in jet control is discussed in Section 1.4. Finally, objectives and the outline of the work are given in Section 1.5 and 1.6.

1.1 State-of-the-art in active flow control

With the experimental visualization of orderly structures in high Reynolds number turbulent flows by pioneering works of Crow and Champagne [29], and Brown and Roshko [18], scientists and engineers dissolved the belief that turbulence is a totally random phenomenon. This new understanding immediately revolutionized flow control strategies. Simple control designs, targeting the mean properties of flows, have been replaced with more sophisticated unsteady methods aiming to manipulate quasi–periodic large–scale coherent motions. These new innovative control designs can be driven in frequency regimes where the flows are most sensitive and therefore yield better performance with an order of magnitude less energy consumption than steady blowing/suctioning actuators. Therefore, this new era in flow control, termed also modern flow control [68], has a huge potential to improve somewhat saturated engineering designs using steady active controls or passive geometrical modifications.

The main challenge in modern flow control is the lack of predictive methods. Overall progress mainly depends on empirical parametric explorations, as the dynamics of deterministic coherent events and their interaction with random background turbulence is still not very well understood. Moreover, the interaction of unsteady controls with coherent structures is extremely complex and hard to analyse. Due to these limitations in physical insight, knowledge of optimum placement and optimal driving signals is inaccessible a–priori. Thus, a large number of experiments has to be conducted to explore the potential control parameter space. This parameter space can have a huge dimension considering the non–linear multi–scale character of turbulent flows. As a result, the overall effort is overshadowed by costly experiments that not always lead to satisfactory results.

In the last decades, Computational Fluid Dynamics (CFD) established itself as a strong alternative to study unsteady actuation, and overcome design barriers related to limited understanding of turbulence dynamics. Nowadays, advances in high performance computing allow the high–fidelity description of turbulent flow phenomena within a feasible time frame. Increased realism in simulations has triggered countless efforts to design modern active controls. In terms of flow control, CFD provides several advantages over experiments.

The primary advantage of numerical simulations is that they enable easy modelling of actuators. Actuators are frequently modelled as simple oscillating boundary conditions. Additionally, they can also be modelled as distributed actuation over the domain. Such an actuation may not even have a direct counter–part in real life applications, but it can be very useful to test the receptivity and controllability of the flow.

Moreover, a very detailed analysis of flow response is possible thanks to Large-Eddy Simulation (LES) or Direct Numerical Simulation (DNS) methodologies. Instantaneous large–scale vortical structures can be visualized with kinematic identifiers based on the velocity gradient tensor [66], and their evolution can be carefully studied, a technology still not available in most experimental set–ups.

Furthermore, CFD can also be merged into flow optimization algorithms. In this way actuation signals can be improved significantly. Flow optimization using CFD has a long history. Passive control designs have been improved over the years using shape or topology optimization methods that require only a modest description of the flow, e.g. by Reynolds-Averaged Navier–Stokes Equations (RANS) [73, 101, 38]. Nevertheless, the tendency to replace passive control means with more complex active control devices required also a transition in flow optimization efforts. Optimal control techniques using adjoint methods have become increasingly popular for unsteady flows in the last decades. Here, turbulent flow states in four dimensions are needed for Large–Eddy Simulations (LES) or Direct Numerical Simulations (DNS) [11, 116, 33, 46]. Optimal control allows an automatic control design by optimizing a cost functional describing the interested flow property. These techniques have a huge potential to overcome the limited understanding in turbulent flows.

1.2 Turbulent axisymmetric jet

This section is devoted to the presentation of round jet flow basics. The turbulent round jet is a prime example of fundamental flows that received considerable technological and scientific attention. In its most basic setting, a round jet flow occurs when a momentum carrying fluid is dispatched through a circular orifice or nozzle into quiescent ambient fluid of the same type. This simple canonical form can be found in many industrial applications. Because of this practical relevance, engineers still actively study this fundamental flow.

In addition to practical concerns, the turbulent jet is also commonly studied by fundamental turbulence researchers as its experimental set-up is relatively inexpensive and easy to build. The flow is rich in terms of large-scale coherent dynamics, and it is comparably easier to educe orderly motion. Therefore, modern turbulence research produced considerable output about the dynamics of the flow, e.g. [28, 29, 61]. Moreover, also classical turbulence research, approaching flow from a statistical perspective, keeps investigating round jets. A very recent example can be found in [110].

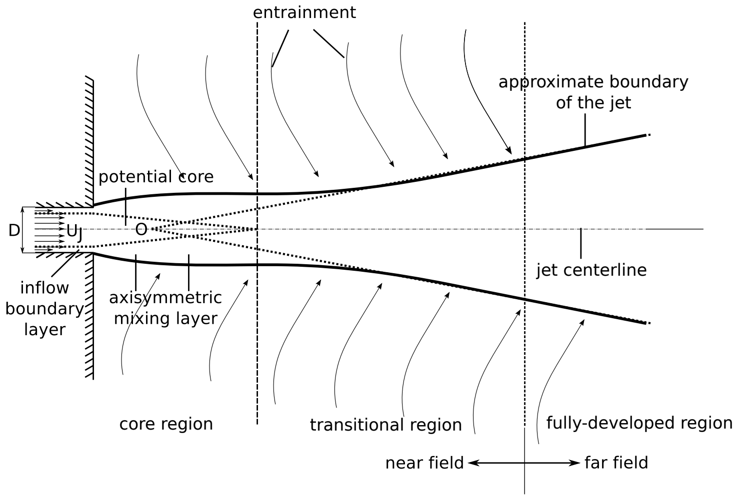

Figure 1.3: A descriptive sketch of a round jet flow. Sizes and jet boundaries are indicative only.

The intention in this section is to briefly introduce fundamentals of jet flow, before control efforts are reviewed in Sections 1.3 and 1.4. First, a flow description and related terminology are introduced in Section 1.2.1. Subsequently, large-scale dynamics and the main structural modes are reviewed in Section 1.2.2. Finally, numerical studies are introduced in Section 1.2.3.

1.2.1 Flow description

A free, incompressible, isothermal, non–swirling jet is considered. A descriptive sketch is given in Figure 1.3. The flow is produced by a continuous supply of a stream into an infinite stagnant environment free from boundaries. The inflow occurs through a circular opening surrounded by solid walls and contains a thick nearly uniform core and a thin boundary layer. The flow is statistically stationary and the mean fields are axisymmetric.

A round jet is conventionally divided into two sections: the near field and the far field. In the near field, usually classified as the region below $x < 30D$, where D is a jet diameter, a further classification into two zones, the core region and the transitional region, is used [84]. In the core region, nearly irrotational flow at the jet center is gradually reduced by a growing axisymmetric mixing layer. This irrotational core, having a constant undiminished velocity at the jet centreline, forms a cone termed the potential core, extends usually up to

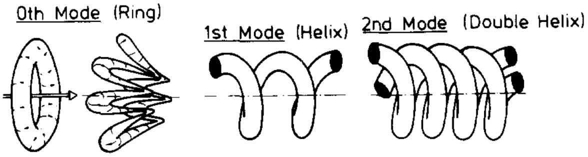

Figure 1.4: Structural modes in the core region of a round jet. Reproduced from Fiedler [40].

$x \approx 5D$. Following the potential core, in the transitional region, turbulence at the jet boundaries develops further and approaches the jet centreline, and the centreline velocity starts to decay. Further downstream, turbulence becomes fully developed. Here, the far field is reached where the velocity and turbulent quantities are assumed to be self similar.

In this work, only the near field of the jet is considered. This is an obvious choice from the control point of view, as the jets are most sensitive in the near field and therefore control effects are most pronounced here. Moreover, the changes in the near field are also relevant in the far field as they can be carried out to the far field with the convective transport. The latest studies show that jets do not forget their origin and initial perturbations play significant role in the far field dynamics [8].

1.2.2 Review of large–scale dynamics

In round jet flows, vortical features in the core region originate from inflow perturbations [58]. These perturbations are first amplified by Kelvin–Helmholtz (KH) instability and result in instability waves. Subsequently, these KH waves roll-up into ring or helical vortices, which appear alternatively, and compete with each other to take their share from base flow kinetic energy. Moving downstream, primary vortices further deform and secondary structures aligned with streamwise direction are formed. Now each step is discussed in more detail.

The initial development of perturbations in the shear (mixing) layer can be described with linear stability theory, and it can be shown that the jet is unstable to a wide range of frequencies. In this region, the most amplified frequency for an axisymmetric perturbation scales with the momentum thickness of the boundary layer θ_0. Its value is calculated using normal mode analysis and found $\mathrm{St}_\theta = fD/\theta_0 = 0.017$ [88]. This most amplified frequency is termed *shear layer mode.* Unlike mixing layers, a round jet with a thin boundary layer, i.e. $\theta_0 \ll D$, is also unstable to a number of helical modes, e.g. see [104] and references therein.

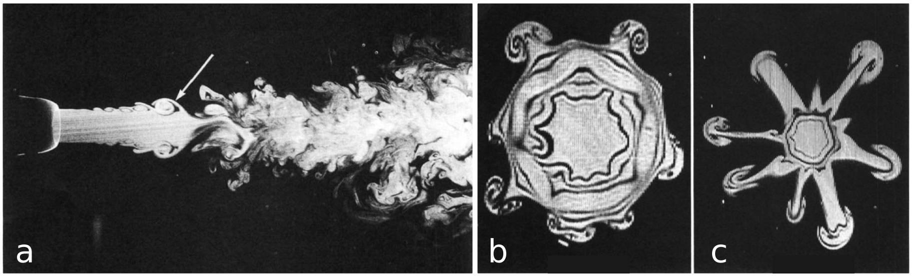

Figure 1.5: (a): Streamwise view of a jet at $\mathrm{Re}_D = 5500$. The arrow indicates a streamwise structure at $x/D = 3.5$. (b): Ring region at $x/D = 3.5$. Mushroom shaped vortices are cross-sections of streamwise vortex pairs. (c): Braid region at $x/D = 3.5$ at different time instance. Reproduced from Liepmann & Gharib [82].

Depending on the energy in the azimuthal modes (0th, 1st or 2nd mode), instability waves can evolve into toroidal or helical vortices (see Figure 1.4). The shear layer further grows inwards with the roll–up or amalgamation of these vortices. At the end of the potential core, the shear layer reaches its maximum size and columnar effects become important. An additional length scale, the jet diameter D, becomes dominant in the flow development. At this location, the evolution of vortical structures is highly non–linear. Therefore, linear theory cannot predict the most amplified frequencies at the end of potential core and literature is based on experimental observations.

Crow and Champagne [29] were the first who made an attempt to determine the most amplified frequency at the end of the potential core. They applied a monochromatic excitation and measured the passage frequencies towards the end of the potential core. The highest amplification is observed by an excitation with a frequency of $\mathrm{St}_D = fD/U_J = 0.3$. Since then, this frequency is called the *jet preferred* or *column mode*. Following Crow and Champagne, numerous researchers investigated the preferred mode and found different values. There is a big scatter in the measured frequencies due to the different measurement techniques and extreme sensitivity of the jet to background disturbances. For a detailed discussion check Ref. [53, 61]. If these effects are minimized by very careful experimentation, the preferred mode frequency can be linked to the momentum thickness as described by [58] and references therein. Below a critical value $D/2\theta_0 \approx 120$, it exhibits approximately proportional behaviour with respect to $D/2\theta_0$, and is a fraction of the dominant shear layer frequency. Above this critical value, the preferred mode frequency is independent from the initial shear layer thickness and locks to a value of about $\mathrm{St}_D = 0.42$ as measured by [37]. The reason for this behaviour is still unknown today.

As in mixing layers [75, 10, 17], secondary streamwise structures are also observed in round jets [119, 3, 81]. When a primary vortex ring grows, it develops azimuthal instabilites known as Widnall instabilities [118]. These instabilities deform the ring into a wavy structure (see Figure 1.4, 0th mode). The peak sides of the wavy rings stretches the strain field in the braid regions and creates streamwise vorticity. Further deformation of primary rings concentrate this streamwise vorticity into pairs of counter–rotating circular vortices (see Figure 1.5), a mechanism known from planar mixing layers [16]. These streamwise vortices play a prominent role in entraining the ambient fluid into the jet core [82], and therefore their manipulation is of major interest as we will discuss in Section 1.3.

1.2.3 Numerical predictions

The initial decades of jet dynamics research were driven only by experiments. Thanks to modern supercomputing, high–fidelity numerical simulations that can accurately predict the dynamics of the jet flow, started to play an increasing role in the jet research. Initial attempts were based on Direct Numerical Simulations confronting the challenging task of resolving all the relevant scales of turbulence. Therefore, these studies covered low–Reynolds number transitional jets, e.g. $\mathrm{Re}_D = 3600$ by Freund [41], and $\mathrm{Re}_D = 2400$ by Boersma et al. [13]. Thanks to the geometric simplicity, standard staggered finite volume methods [56] or high–order compact finite difference methods [80], all formulated in cylindrical coordinates, were natural choices. Following the success of DNS studies jet researchers moved towards high Reynolds number cases using Large–Eddy Simulations and the advancements in subgrid–scale modelling. For various attempts in this area please check [30, 14, 71].

The works listed above studied jet flows almost exclusively in idealized geometries with dedicated numerics. In the current work, one of the goals is to conceptually test the extendibility of numerical jet research to more flexible geometries using generic unstructured collocated finite–volume numerics. Although we will still limit the focus on simple geometries, the framework will be directly transferable to more realistic engineering geometries.

The simulation method of choice is Direct Numerical Simulations because of two main reasons. First, DNS is a model–free approach and therefore allows for maximum realism in simulations. Secondly, low Reynolds number jets have less background turbulence. This significantly aids in the flow diagnostics and the understanding of the flow mechanisms.

1.3 Jet-flow control

It is well known that the flow field of a round jet is completely determined by upstream conditions [93]. Especially the near field development is very sensitive to the inlet profile and its perturbations [71]. Due to the convective nature of the axisymmetric jet, modifications in the near field may also be carried out to the far field [102], where non-linear dynamics are the dominant mechanism. This sensitivity of the jet flow motivated numerous control efforts over the years.

Typical jet flow control objectives are mixing enhancement, jet noise reduction and vectoring the jet thrust. Mixing enhancement is the main focus of this dissertation but we will also investigate turbulence suppression mechanisms, which may be favourable for noise reduction. Jet vectoring is not in the scope of this study.

As mixing enhancement is the center of discussion in the further sections, the mixing phenomena is shortly discussed here. Mixing process can be synthesized into three distinct stages [35]: *entrainment*, *stirring* and *molecular mixing*. In the initial entrainment stage, large scales engulf irrotational ambient fluid into the turbulent core. Subsequently, in the stirring phase, the interfacial surface between the unmixed species is increased by intermediate scales of turbulence. In the final stage, the molecular mixing process occurs at the fine scales of motion. At this stage the mixing rate is determined by the contact surface area of the mixing fluids. It can be enhanced implicitly by promoting the fine scale structures of the turbulent flow. As a result, mixing augmentation is a highly challenging multi–scale control problem.

This section is devoted to a review of control efforts aiming to modulate jet dynamics. First, a short review of flow control efforts is given in Section 1.3.1. Then, zero–net–mass–flux actuators, also called synthetic jets, are introduced in Section 1.3.2.

1.3.1 Brief look into the literature

Control designs aim at the manipulation of coherent vortical features, and their interactions and eventual breakdown to finer scales of turbulence. As discussed in Section 1.2.2, these structures are induced by instability mechanisms of the mean inlet jet profile. The growth of initial disturbances results in shedding of toroidal KH rings if the axisymmetric instability mode is dominant. Consecutive KH rings lose their axisymmetry and give rise to secondary structures oriented in streamwise direction. These are also known as braid vortices as they occur in the braid regions located between consecutive KH rings. In an uncontrolled jet these events occur randomly. Therefore, the main strategy in jet flow control is controlling the evolution of primary and secondary instabilities by imposing axial and azimuthal perturbations in an organized fashion.

Passive steady controls are based on introducing azimuthal perturbations by modifying inlet nozzle designs. Elliptic, triangular and rectangular nozzles [49], mounted vortex generators and tabs [120] and lobed nozzles [92] are common examples enhancing the mass entrainment rate. Here broken axisymmetry of the inlet geometry causes variations in the azimuthal curvature of primary rings which lead to self-induced Biot-Savart deformations [9] and eventually the development of streamwise vortex structures. These are known for their ability to promote entrainment and bulk mixing in the near field of the jet [82]. The complex interactions of streamwise and azimuthal vortices gives also rise to fine-scale developments further downstream, and increases mixing in the local molecular sense.

In contrast to nozzle designs that focus on augmentation of turbulence and mixing, chevron nozzles suppress the turbulence and spreading of the jet and are therefore favourable to reduce acoustic emissions, e.g. [20, 19]. In chevron jets counter-rotating streamwise vortex pairs dominate the near field dynamics, and the growth of azimuthal structures is delayed [115]. Inhibition of large-scale primary vortices in the near field leads to a reduction in the far field noise. Similar effects can also be achieved by the use of microjets [4, 23], which is an example of steady active control.

Active unsteady control methods impose periodic excitations to influence the large-scale dynamics. They can be classified in two groups: small-amplitude control and large-amplitude control [68]. The approaches in the former group focus at imposing small perturbations at the nozzle lip to trigger the shear layer instability modes of jets [40]. In this way, subsequent merging and growth of primary structures can be manipulated. The methodology closely resembles mixing layer control studies, except that in jets also azimuthal instability modes can be exploited. In mixing layers, excitation of shear layer modes can manipulate the merging of the primary structures that evolve through the entire length of the experimental set–up. This is not the case for jets, where the shear layer reaches its physical limit at the end of the potential core, and primary structures disintegrate. This is the biggest limitation for small–amplitude control.

Large-amplitude control approaches cover a wide range of studies imposing perturbations with a magnitude comparable to main jet velocity. Here, main jets can be subjected to localized cross–stream perturbations at the nozzle lip, such as flapping actuators or plasma actuators [104], or they can be subjected to some global pulsating mechanism implemented on the entire nozzle. Thanks

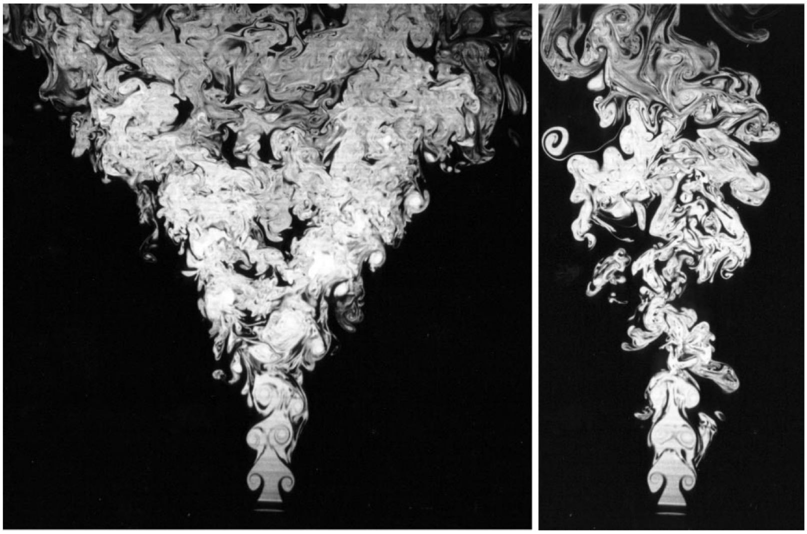

Figure 1.6: Bifurcating water jet at $\mathrm{Re}_D = 4300$: (left) bifurcation plane; (right) bisecting plane. Reproduced from Lee & Reynolds [102].

to high level perturbations, these methodologies have an increased control authority over the jet column, and therefore excitation of the jet preferred mode can lead to dramatic changes in the jet development.

A first example showing dramatic changes in jet evolution corresponds to the so called bifurcating and blooming jets [102]. An image of a bifurcating jet is shown in Figure 1.6. It is obtained by dual mode excitations using axial forcing with a magnitude of about $0.2U_J$ in combination with a helical perturbation with a magnitude of about $0.05U_J$. If the forcing frequency of the helical mode is one half of the frequency of the axial mode, i.e. $f_h/f_a = 2$ where $\mathrm{St}_a = f_a D/U_J = 0.5$, the vortex rings evolve with a slight radial displacement. Then, successive vortex rings tilt each other with mutual induction, and the jet eventually bifurcates into two distinct regions downstream. This is a very nice example that demonstrates the power of coherent–structures–based jet control. Although the focus here is only on the dynamics of primary structures, i.e. azimuthal vortex rings, the results are remarkable, and very good improvements in large–scale mixing can be observed.

Another remarking example for modification in flow structures occurs when the the jet is forced with axial pulsation in its preferred mode frequency. Forcing with natural jet frequency can lead to surprising secondary instabilities also known as “*side jets*”. On transverse views they appear as secondary mini-jets ejected radially away from the jet core giving, the jet star-like patterns. They were first observed in experiments with low-density jets [89] where self-sustained global oscillations regularize and synchronize primary ring structures to the natural frequency mode. The same phenomenon can also be observed for regular homogenous jets using strong axial forcing in which vortex rings are synchronized and shed with the forcing frequency [78, 90]. The key element here is the synchronization of vortex rings so that their strength and size is promoted. Then, the appearance of lobes on these rings due to azimuthal instabilities induces a positive strain in the braid region, giving rise to streamwise vortex filaments. Side jets are formed by these counter-rotating vortex pairs initially oriented in axial direction but soon propelling away from the jet centreline by their own induction, and causing anomalous spreading on streamwise planes. These long-lived structures are also responsible for enhancing large–scale mixing by entraining large masses of ambient fluid [34].

Side jets can also be produced by localized cross-stream forcing, i.e. by imposing periodic azimuthal perturbations. Brancher et al. [16] made a comprehensive analysis of side jets by conducting DNS simulations of a convective jet and clearly described the mechanisms leading to the formation of side–jets. Azimuthal excitation has the favourable effect of creating the lobes on the vortex rings in a desired arrangement instead of having them at random locations, leading to side jets that are randomly located.

1.3.2 Synthetic jets

One of the most popular time-periodic fluidic actuators is the so-called synthetic jet or ZNMF actuator [44]. The ZNMF actuators are quite attractive in the sense that they don't require an external fluid source, and work simply with the ambient fluid. Due to their oscillatory nature, there is no net mass addition to the main flow. Nevertheless, ZNMF actuators are capable of transferring a net momentum. Moreover, being a high bandwith device, they are also capable of producing complex waveforms using various types of drivers, including piezoelectric [64], capacitive [91] and electrodynamic [2].

Despite their strong potential, ZNMF actuators in jet flow control remain relatively unexplored. Parallel allocation of a ZNMF actuator with respect to the main jet can cause vectoring of the main jet if the control frequency is orders of magnitude higher than main jet instability frequencies [99]. If a ZNMF actuator is pointed to the main jet centreline, the effect is more complex due to direct impact of the synthetic jet. In this case, it can penetrate into the primary jet and break down its azimuthal symmetry. Depending on the momentum of the synthetic jet, and therefore the degree of penetration, this may initiate vortex induction mechanisms for increased entrainment such as in non-circular jets or turbulence supression mechanisms as in chevron jets. These effects also depend on the actuation frequency which allows manipulating global scale modes of the jet. Having a great flexibility to configure actuation frequency and momentum, ZNMF actuators have the capacity to become a versatile and powerful jet control device.

Tamburello and Amitay [106] investigated the interaction of a single synthetic jet with an axisymmetric jet at $\mathrm{Re}_D = 6600$ using various momentum coefficients, a ratio of synthetic jets momentum to main jets momentum, of $0.005 < C_\mu < 0.16$ and frequencies between $(0.16 < \mathrm{St}_D < 0.48)$. Mounting the ZNMF actuator $1.25D$ away from the jet centreline they observed the largest effect for $\mathrm{St}_D = 0.32$ in low C_μ excitation, and no sensitivity to the actuation frequency for high C_μ. They also identified counter-rotating streamwise vortices resulting from jet penetration and showed that their size and strength increased with momentum coefficient.

To our knowledge, there haven't been any numerical studies for ZNMF actuated round jets that carefully visualize the characteristics of three-dimensional vortex topology, and elucidate mechanisms for their evolution. In the present study, one of the motivations is to numerically investigate these typical flow patterns and their effect on key jet mixing parameters and to make connections to the bulk literature of jet flow control. To this end, we will model synthetic jets as oscillatory boundary conditions, and analyze the flow response with DNS experiments. Oscillatory velocity boundary conditions are able to produce synthetic jets featuring a well-organized train of vortex rings as previously shown in Ref. [76]. The considered control configuration can be seen in Figure 4.1 in Chapter 4.

1.4 The quest for optimization

In Section 1.3, we summarized numerous efforts to control an axisymmetric jet. All these efforts can be classified as brute-force approaches, in which the jet response is evaluated with respect to a certain control parameter by scanning its full range. Therefore, these studies were able to only explore a limited set of control parameters. Being a very complex multi-scale nonlinear system, this limited set of controls remains far from fully exploiting the rich dynamics of turbulent jets.

With the increasing availability of computing resources, flow optimization methods enabled the exploration of larger parameter spaces in active control of turbulent flows. A typical flow optimization, or optimal flow control study, aims to minimize a cost functional quantifying the flow control objective by using an optimization algorithm. To this date, flow optimization studies in large-parameter spaces were carried out almost exclusively with gradient-based methods, as these methods have better convergence properties compared to other classes of optimization algorithms, e.g. evolutionary and stochastic methods. Moreover, the gradient-based methods allow a reasonable reduction in first couple of iterations [52, 25] so that the algorithm can be stopped prematurely if the computational resources are limited. These methods are based on finding descent directions in the optimization landscape and updating the controls using these descent directions. These directions are constructed from the gradient of the cost functional. Therefore, this gradient has to be calculated at every optimization iteration. To that end, the adjoint method is commonly used, as it provides the whole gradient vector by solving the adjoint Navier-Stokes equations, and is insensitive to the dimension of the control parameter space.

When it is applied to unsteady flows, the adjoint method requires the storage of velocity fields at each time step. Early efforts using the adjoint method in combination with DNS, or LES, suffered due to this excessive storage requirement, and focused on idealized flows such as periodic channel flow [11], and spatially developing [116], or convective mixing layers [33]. More recently, optimal control was applied also to turbulent jets by Kim et al. [70] who employed adjoint–based gradient methods to reduce turbulent jet noise.

Optimal control with an adjoint method can be very interesting for jet mixing enhancement using ZNMF actuators considering the multi–scale nonlinear nature of the mixing problem, and the high bandwidth capabilities of the control device. To the authors knowledge, the only effort to date in optimal control of jet mixing has been made by Hilgers and Boersma [54]. They applied stochastic optimization methods to a relatively low–dimensional control parameter space covering amplitudes for helical and axial mode excitation of the jet. Their control methodology and frequency range allow an optimization by increasing organized motion in the jet, such as increasing the spreading of the jet. Although, this can be quite beneficial for the first two stages of mixing, i.e., entrainment and stirring, it can be detrimental to the molecular mixing stage as increased coherent behaviour can delay the transition to finer scales [93]. Therefore, in jet mixing optimization problems, the full range of turbulent motion should be properly addressed by controls.

In this study, an attempt to improve jet mixing is made by using adjoint–based gradient methods. The continuous adjoint method is the method of choice where the optimization problem is first formulated in continuous setting, and discretized and solved subsequently. ZNMF actuators are modelled as localized forcing regions and supplied with a wide range of frequencies. The configuration can be seen in Figure 6.1 in Chapter 6. The jet mixing is not directly tackled as it is a very difficult phenomenon to quantify with a simple cost functional measured over a limited time horizon. We instead optimize for kinematical mechanisms that implicitly lead to improved mixing. To this end, we pick up an enstrophy integral measured over a selected observation domain and time window. Delport et al. [33] demonstrated that maximizing the enstrophy accelerated the small-scale transition in convective mixing layers. As discussed before, an efficient small-scale transition is essential for molecular mixing.

1.5 Aims and objectives

This dissertation aims at contributing to the field of active control of turbulent jets. The main goal is exploring the capabilities of ZNMF actuation in round jet flow control. The control objective is to improve mixing properties. To this date, the application of these promising devices to turbulent axisymmetric jets were limited to simple configurations, such as a single actuator driven with a single frequency, cf. in Section 1.3.2. The complex flow mechanisms resulting from the actuation were not well understood, and the lack of insight prevented the design of more complicated control configurations. Therefore, the capabilities of ZNMF actuators in jet-flow control is not fully exploited yet.

Another goal of the dissertation is to develop a generic numerical flow control and optimization framework that is applicable to sophisticated engineering geometries where jet flows can appear. Although we limit our studies to basic jet geometries, the framework will be extensible to complex geometries in future studies.

In order to address these issues and explore more effective control designs using multiple ZNMF actuators and multiple actuation frequencies, four objectives are formulated for the current study:

1. Improvement of OpenFOAM® in order to allow cost-effective DNS studies on generic flow geometries.
2. DNS analysis of kinematical flow mechanisms leading to global changes in the jet flow that is controlled with multiple ZNMF actuators driven with a single frequency in phase.
3. Development of an optimization framework in OpenFOAM® for unsteady turbulent flow simulations using the continuous adjoint method.
4. Exploring the potential of the optimal control of axisymmetric jet flows to achieve better mixing properties using multiple ZNMF actuators equipped with complex waveforms.

1.6 Outline

This dissertation is organized as follows. In Chapter 2, the basic numerical methods in OpenFOAM® are discussed and a projection algorithm to improve the cost of time stepping is introduced. Subsequently, a parallelization of statistical averaging in DNS to improve parallel scaling is proposed in Chapter 3. In Chapter 4, a DNS study is conducted to study the active control of turbulent jets with three ZNMF actuators. Chapter 5 is devoted to the formulation of the jet flow optimization with the continuous adjoint method. Subsequently, an optimal control study is carried out in Chapter 6 for transitional round jets using twelve ZNMF actuators. Finally, conclusions of the study and an outlook for future research are given in Chapter 7. The content of these sections is fully synthesized in more detail below.

First of all, Chapter 2 focuses on the discretization of the incompressible Navier–Stokes equations with OpenFOAM®. Being a generic CFD solver, OpenFOAM® employs a Finite-Volume-Method designed for unstructured grids. This method is briefly discussed in Section 2.2 following the introduction of the governing equations in Section 2.1. Subsequently, the one-step-theta scheme for the discretization of the temporal term, and the linearisation of the convective term with extrapolation in time, are discussed in Section 2.3. Finally, the incremental projection algorithm is introduced in Section 2.4 as an alternative to the existing PISO scheme in OpenFOAM®. It is shown that this scheme has 45% less time step cost for the DNS of round jet case.

Chapter 3 starts with introducing the computational speed-up and efficiency metrics for the parallelization of statistical averaging in turbulent flows. Subsequently, the corresponding timescales in these metrics are estimated for the turbulent round jet case in Section 3.2. Finally, the applicability of the approach is demonstrated in Section 3.3 using DNS of a round jet.

In Chapter 4, the near field of a ZNMF actuated round jet is studied using DNS. The motivation is to investigate typical flow patterns and their influence on key jet parameters. The Reynolds number of the jet $\mathrm{Re}_D = 2000$, and three ZNMF actuators are used, evenly distributed over a circle and directed towards the main jet. The actuators are driven in phase, and have a relatively low momentum coefficient of $C_\mu = 0.0049$ each. Four different control frequencies are studied, with Strouhal numbers ranging from $\mathrm{St}_D = 0.165$ to $\mathrm{St}_D = 1.32$. Furthermore, two uncontrolled jet simulations are also included in the study. The chapter starts with introducing the flow configuration and computational details in Section 4.1. Subsequently, the features of the instantaneous flow field are discussed in Section 4.2. The mean flow properties are discussed in Section 4.3, and passive scalar evolution and scalar transport tubes are presented.

Finally, conclusions summarizing the changes in the controlled flows, and the mechanisms allowing this strong control authority, are given in Section 4.4.

Chapter 5 is devoted to the description of the jet-flow optimization problem using a continuous adjoint method. The chapter starts with the formulation of an enstrophy maximization problem in Sections 5.1.1-5.1.3. Subsequently, a steepest-descent method is presented in Section 5.1.4 to solve the optimization problem. This algorithm requires the solution of the adjoint incompressible Navier-Stokes equations. This is addressed in Section 5.2, where the adjoint version of the projection scheme is presented to solve these equations in OpenFOAM®. Finally, limitations of the adjoint method for turbulent jet optimization are discussed in Section 5.3.

Chapter 6 is devoted to an application of the optimization framework introduced in Chapter 5. To this end, an optimal distributed control study for an axisymmetric jet at $\mathrm{Re}_D = 2000$ is performed. The aim of the study is enhancing enstrophy of a transient jet in the near field region extending up to $x = 6D$. The enstrophy is assumed to be linked to the mixing characteristics of the flow, cf. Section 5.1.1 for a discussion. Twelve controls are modelled as small localized regions around the jet circumference with a uniform forcing distribution. The numerical configuration about this optimal control problem is introduced in Section 6.1. A verification study for the adjoint-based gradients follows in Section 6.2. Finally, the optimization is conducted, and results are presented and analysed in Section 6.3.

Finally, in Chapter 7, conclusions of the study are drawn and suggestions for further research are given.

Chapter 2

Numerical Methods

In this chapter, we review the numerical methods to solve jet flow problems. Direct numerical simulation is the method of choice, i.e., the conservation equations are discretized and solved directly without any explicit modelling. OpenFOAM® employs Finite-Volume Methods (FVM) for the spatial discretization of conservation equations. Following the spatial discretization with FVM, a differential algebraic equation system is obtained. Subsequently, classical time integration schemes can be applied to the temporal term in this differential algebraic equation system in the spirit of the method of lines. Finally, the overall system is solved in a segregated way as the official distribution of OpenFOAM® does not include any algorithm to solve the fully discretized coupled system matrix. To this end, OpenFOAM® features a variant of the PISO algorithm [63, 65], entitled *pisoFoam*, that solves the incompressible flow equations with successive iterations.

In the initial studies with pisoFoam, we have observed that a considerably high fraction of computation time is spent on solving the Poisson equation iteratively. In order to reduce the computational costs for DNS, the pisoFoam solver is replaced with an incremental projection scheme [113], which does not require iterative Poisson solutions. This classical scheme is non-iterative, and therefore costs less than the PISO scheme. For a round jet DNS case, a performance gain of about 45% is realized.

In the first step of a projection scheme, the momentum equation including an old time step pressure is solved and the resulting velocity field is not divergence–free. Then, the divergence of the velocity is projected out by solving a Poisson equation. The scheme is mass-conservative and has an additional second order segregation error in time for velocity. Therefore, the order of accuracy is consistent with the second order time integrators in OpenFOAM® such as Crank-Nicolson and backwards differencing methods.

This chapter is organized as follows. First, the governing equations are briefly introduced in Section 2.1. Subsequently, spatial discretization with FVM is reviewed in Section 2.2. Then, the temporal discretization is discussed in Section 2.3. Finally, the projection method is discussed in detail in Section 2.4.

2.1 Governing equations

This section introduces the continuum equations of transient, isothermal, viscous fluid motion. We exclusively consider incompressible flows where Mach number is Ma ≤ 0.3. For reasons of brevity, we only consider Dirichlet boundary conditions. The governing equations for the conservation of linear momentum are the full incompressible isothermal Navier–Stokes equations on a domain $\overline{\Omega} = \Omega \times (0, T]$,

$$\frac{\partial u_i}{\partial t} + \frac{\partial u_j u_i}{\partial x_j} = -\frac{\partial p}{\partial x_i} + \frac{1}{\mathrm{Re}_D} \frac{\partial^2 u_i}{\partial x_j \partial x_j} + f_i \qquad \text{in } \overline{\Omega}, \tag{2.1}$$

$$\frac{\partial u_i}{\partial x_i} = 0 \qquad \text{in } \overline{\Omega}, \tag{2.2}$$

$$u_i = g_i \qquad \text{on } \overline{\partial\Omega}, \tag{2.3}$$

where repeated indices are summed using Einstein's summation convention, x_i are spatial coordinates normalized by the jet diameter D, u_i are the fluid velocity components normalized by the jet exit velocity U_J, t is the time normalized by D/U_J, f_i is a body force, g_i is a specified velocity, Re_D denotes the Reynolds number based on D and U_J, and p is the non–dimensional gauge pressure.

In addition, the transport of a scalar quantity c is considered. This will be used in the mixing analysis in further chapters. Conservation of this quantity is governed by a passive scalar transport equation

$$\frac{\partial c}{\partial t} + \frac{\partial u_i c}{\partial x_i} = \frac{1}{\mathrm{Re}_D \mathrm{Sc}} \frac{\partial^2 c}{\partial x_i \partial x_i} \qquad \text{in } \overline{\Omega}, \tag{2.4}$$

$$c = c_d \qquad \text{on } \overline{\partial\Omega}, \tag{2.5}$$

where Sc denotes the Schmidt number and c_d is a specified scalar concentration. As the scalar transport equation has common operators with the momentum equation in Eq. (2.1), the discretization of this equation is not additionally discussed. In the further sections, the focus is on the discretization of the incompressible Navier–Stokes equations in Eq. (2.1) – Eq. (2.3).

2.2 Spatial discretization

This section is devoted to a brief review of the Finite Volume Method (FVM). Detailed information about FVM numerics in OpenFOAM® can be found in Jasak [65]. The Finite Volume Method is a method of weighted residuals [114]. In the method of weighted residuals, the residual of the strong form of the equations, which vanishes for the continuous case, is weighted by an appropriate set of test functions and integrated over the fluid domain Ω. For the incompressible Navier-Stokes equations this is described by

$$\int_{\Omega} v_i \left(\frac{\partial u_i}{\partial t} + \frac{\partial u_j u_i}{\partial x_j} + \frac{\partial p}{\partial x_i} - \frac{1}{\mathrm{Re}_D} \frac{\partial^2 u_i}{\partial x_j \partial x_j} - f_i \right) \mathrm{d}\boldsymbol{x} = 0, \tag{2.6}$$

$$\int_{\Omega} q \frac{\partial u_i}{\partial x_i} \mathrm{d}\boldsymbol{x} = 0, \tag{2.7}$$

where $\boldsymbol{v}$ and q are suitable velocity and pressure test functions respectively. If we discretize the domain Ω with non-overlapping arbitrary polyhedral grid elements Ω_k, i.e. $\Omega = \bigcup_{k=1}^{N} \Omega_k$, and define test functions with local support in these elements, i.e.

$$v_i^k(\boldsymbol{x}) = \begin{cases} 1 & \text{if } \boldsymbol{x} \in \Omega_k, \\ 0 & \text{if } \boldsymbol{x} \notin \Omega_k, \end{cases}$$

we end up with local conservation equations within each grid elements, also referred to as control volumes. The overall equation system reads then as follows

$$\int_{\Omega_k} \left(\frac{\partial u_i}{\partial t} + \frac{\partial u_j u_i}{\partial x_j} + \frac{\partial p}{\partial x_i} - \frac{1}{\mathrm{Re}_D} \frac{\partial^2 u_i}{\partial x_j \partial x_j} - f_i \right) \mathrm{d}\boldsymbol{x} = 0, \tag{2.8}$$

$$\int_{\Omega_k} \frac{\partial u_i}{\partial x_i} \mathrm{d}\boldsymbol{x} = 0, \tag{2.9}$$

for $k = 1, \ldots, N$. Hereafter, we will omit the continuity equation in the discussion as this equation is never directly discretized. It is treated implicitly by the segregated solution algorithm (cf. Section 2.4).

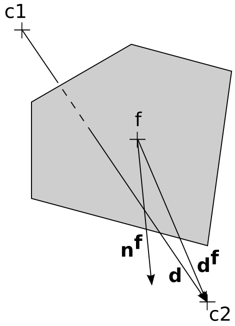

Figure 2.1: Metrics defining geometrical relations between two neighbouring cells and the face in between. $c1$ and $c2$ are the cell centroids and f is the face centroid.

In the next step, the element volume integrals containing spatial differential operators are converted to surface integrals $\partial\Omega_k$ by using Gauss' Divergence Theorem:

$$\int_{\Omega_k} \left(\frac{\partial u_i}{\partial t} - f_i \right) \mathrm{d}\boldsymbol{x} + \int_{\partial\Omega_k} \left(u_i u_j + p\delta_{ij} - \frac{1}{\mathrm{Re}_D} \frac{\partial u_i}{\partial x_j} \right) n_j \mathrm{d}\boldsymbol{x} = 0, \qquad (2.10)$$

where $\boldsymbol{n}$ is the unit surface normal of element boundaries, also denoted as faces.

Until now, there was no numerical approximation involved. A numerical integration scheme has to be applied to evaluate the integrals. Applying the second–order accurate midpoint rule, the approximated equations for each element read as follows

$$\left(\frac{\partial u_i^k}{\partial t} - f_i^k \right) |\Omega_k| + \sum_{f=1}^{N_{kf}} \left(u_i^f u_j^f + p^f \delta_{ij} - \frac{1}{\mathrm{Re}_D} \left(\frac{\partial u_i}{\partial x_j} \right)^f \right) n_j^f |\partial\Omega_k^f| = 0, \quad (2.11)$$

where the superscripts k and f denote evaluations in element and face centroids respectively, $|\Omega_k|$ is the volume of the polyhedral element, $|\Omega_k^f|$ is the area of the faces and $\boldsymbol{n}^f$ the corresponding unit normal, N_{kf} is the total number of faces around the element.

OpenFOAM® is designed for unstructured collocated grids where all the field variables are stored on cell centroids. The required data on face centroids in Eq. (2.11), i.e., u_i^f and p^f, have to be interpolated from the neighbouring cell centroid data. OpenFOAM® provides numerous options for data interpolation (cf. [96] for a detailed list of options). Linear interpolation is the method of choice in the current work. In Figure 2.1 a face f between two arbitrary

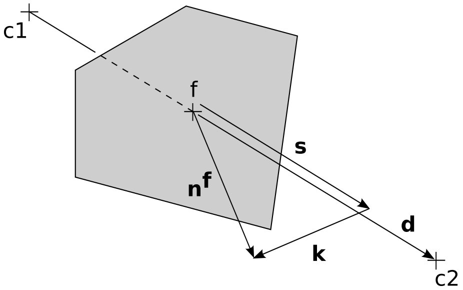

Figure 2.2: Illustration of the vectors used in the non–orthogonal correction approach in Eq. (2.14).

polyhedral elements and related geometrical metrics is illustrated. Using these metrics, a linear interpolation operator, denoted with $\overline{(\cdot)}$, is defined as follows

$$u_i^f \approx \overline{(u_i^k)} := w^f u_i^{c1} + (1 - w^f) u_i^{c2}, \text{ where } w^f = \frac{|n_i^f d_i^f|}{|n_i^f d_i|}. \tag{2.12}$$

It is a second order accurate approximation except for severely skewed elements where the accuracy reduces to first order [65]. Using Eq. (2.12), the velocity flux ϕ_f on the faces can be defined as

$$\phi_f = \overline{(u_i^k)} n_i |\partial\Omega_k^f| \approx u_i^f n_i |\partial\Omega_k^f|. \tag{2.13}$$

Eq. (2.11), requires an evaluation for the face normal gradient operator, namely $n_j(\partial u_i/\partial x_j)^f$. To approximate this operator, a central differencing scheme is selected. It contains a non–orthogonal correction based on a deferred–correction approach [39, 65]. The metrics for this correction are illustrated in Fig. 2.2. Using these metrics, the calculation of the surface normal gradient is given by:

$$n_j^f \left(\frac{\partial u_i}{\partial x_j}\right)^f = (s_j + k_j) \left(\frac{\partial u_i}{\partial x_j}\right)^f \approx \frac{u_i^{c2} - u_i^{c1}}{|n_j d_j|} + \left(k_j \frac{u_i^{c2} - u_i^{c1}}{d_j}\right)_o, \tag{2.14}$$

the subscript o denotes the explicit evaluation of the term with the available field data. Therefore, the term with subscript o is evaluated with old values of $\boldsymbol{u}^{c1}$ and $\boldsymbol{u}^{c2}$. It is treated as a source term, and is put on the right hand side of the matrix equations. This correction term with the vector $\boldsymbol{k}$ vanishes for orthogonal cells, as $\boldsymbol{s}$ and $\boldsymbol{n^f}$ completely overlap in this case.

2.3 Temporal discretization

In this section, temporal discretization of the incompressible Navier–Stokes equations is discussed. OpenFOAM® features various one–step–theta methods for time integration, such as Crank–Nicolson, backwards Euler or forwards Euler. Moreover, OpenFOAM® also features a second order backwards differencing scheme which is never used in this work and therefore will not be included in the discussion. To ease the presentation we will write the equations in space continuum.

For application of a standard theta method, the time interval is uniformly partitioned into time steps of size δt. Field values at time level $t^n = n\delta t$ are accordingly defined as $\boldsymbol{u}^n$ and p^n. Then, using an implicitness parameter $\theta \in [0, 1]$, the following notation holds

$$\boldsymbol{u}^{n+\theta} = \theta \boldsymbol{u}^{n+1} + (1-\theta)\,\boldsymbol{u}^n. \tag{2.15}$$

Using the notation in Eq. (2.15), the application of the one–step theta scheme to incompressible Navier-Stokes in Eq. (2.1) – Eq. (2.3) results in the following temporally discretized set of nonlinear equations

$$\frac{u_i^{n+1}-u_i^n}{\delta t} + \frac{\partial u_j^{n+\theta} u_i^{n+\theta}}{\partial x_j} = -\frac{\partial p^{n+\theta}}{\partial x_i} + \frac{1}{\mathrm{Re}_D}\frac{\partial^2 u_i^{n+\theta}}{\partial x_j \partial x_j} + f_i^{n+1} \qquad \text{in } \Omega, \tag{2.16}$$

$$\frac{\partial u_i^{n+1}}{\partial x_i} = 0 \qquad \text{in } \Omega, \tag{2.17}$$

$$u_i^{n+1} = g_i^{n+1} \qquad \text{on } \partial\Omega, \tag{2.18}$$

The most simple case is $\theta = 0$ which yields the first–order accurate, i.e. $\mathrm{O}(\delta t)$, fully explicit forward Euler method. In general, fully explicit methods are attractive as they don't require any matrix inversion. But this is not applicable to incompressible flows as the pressure in these flows does not have an evolution equation and is elliptically linked to the velocity through a Poisson equation [48]. Therefore, the discretized version of this Poisson equation has to be solved at each time step. Another drawback of the explicit Euler method is the strong time step restrictions due to CFL the (Courant–Friedrichs–Lewy) condition [56]. Consequently, the low–order explicit Euler method is clearly unattractive for DNS or LES. The common choice of the fully explicit time integrator in DNS/LES community is the multi–stage Runge–Kutta scheme as it allows high–order accuracy and is less restrictive on the time step. However, for incompressible flows, this method requires to solve the costly Poisson equation multiple times per time step as it requires at each substage an intermediate pressure. This bottleneck makes this popular method also unfavourable for the current DNS studies.

For $\theta > 0$, the family of implicit time integrators is obtained. The most frequently applied members in this family are

- *Crank–Nicolson Scheme*: $\theta = 0.5$, unconditionally stable but prone to oscillations for large time steps, second order accurate, i.e., $\mathrm{O}(\delta t^2)$.
- *Backwards Euler Scheme*: $\theta = 1$, unconditionally stable, first order accurate, i.e., $\mathrm{O}(\delta t)$, characterized by dissipative behaviour.

The Crank–Nicolson scheme is an obvious choice for current DNS studies because of the relatively higher accuracy and the desirable stability behaviour. Being an implicit method this scheme requires the linearization of the convective term. To linearize this term, we can introduce an approximation $u^{n+\gamma}$ using extrapolation in time

$$\boldsymbol{u}^{n+\gamma} = \gamma \boldsymbol{u}^{n-1} + (1-\gamma)\,\boldsymbol{u}^{n} \quad \text{for} \qquad \gamma \leq 0. \tag{2.19}$$

According to this definition the following approximation orders hold for two different values of γ

$$\gamma = 0 \quad : \quad \boldsymbol{u}^{n+\gamma} = \boldsymbol{u}^{n} = \boldsymbol{u}^{n+1} + O(\delta t), \tag{2.20}$$

$$\gamma = -0.5 \quad : \quad \boldsymbol{u}^{n+\gamma} = 1.5\boldsymbol{u}^{n} - 0.5\boldsymbol{u}^{n-1} = \boldsymbol{u}^{n+1} + O(\delta t^2). \tag{2.21}$$

For $\gamma = 0$, only the previous time-step velocity is used for extrapolation. This is the method of choice in the OpenFOAM® PISO solver. As this extrapolation is only first order, we replace it with second order form using Eq. (2.21). This new extrapolation does not require any additional cost except the storage of an old time step velocity vector, i.e., the discrete version of $\boldsymbol{u}^{n-1}$.

2.4 Projection method: a non-iterative segregated solver

This section is devoted to the presentation of the projection method which is a method to seggregate momentum, Eq. (2.1), and continuity, Eq. (2.2) equations, and derive a set of related equations that can be solved in a sequential fashion.

The original projection methods by Chorin [26, 27] and Temam [107, 108] were developed as time marching techniques for evolutionary incompressible fluid problems. Although the usual philosophy of fractional methods are not directly applicable to incompressible Navier–Stokes equations due to the incompressibility constraint, projection methods are also classified as fractional step methods in this context because of the decomposition of a time step into fractional substeps [48].

This section is organized as follows. First, the theory for the projection scheme is discussed in Section 2.4.1. Subsequently, an incremental projection scheme is introduced in Section 2.4.2, followed by a discussion on the discretization on collocated grids in Section 2.4.3. Then, the second order accuracy of the algorithm is verified in Section 2.4.4. Finally, the performance of the scheme for a round jet DNS case is demonstrated in Section 2.4.5.

2.4.1 Theory

The name of the projection methods comes from the idea of projecting a general vector field onto a subspace of solenoidal vector fields. This is realized by one instance of the general Helmholtz–Hodge decomposition by Ladyzhenskaya [77]. Ladyzhenskaya states that any vector field $\boldsymbol{u^*}$ can be interpreted uniquely as the sum of a soleinoidal vector, e.g. the incompressible flow velocity $\boldsymbol{u}$, and an irrotational vector, e.g. the pressure gradient ∇p, i.e.

$$u_i^* = u_i + \frac{\partial p}{\partial x_i}, \tag{2.22}$$

which are orthogonal by definition, i.e.,

$$\int_\Omega u_i \frac{\partial p}{\partial x_i} \mathrm{d}\boldsymbol{x} = -\int_\Omega \frac{\partial u_i}{\partial x_i} p \mathrm{d}\boldsymbol{x} + \int_{\partial\Omega} p u_i n_i \mathrm{d}\boldsymbol{x} = 0, \tag{2.23}$$

for enclosed flows with $u_i n_i|_{\partial\Omega} = 0$. Using the definition in Eq. (2.24), a projection operator (cf. Fig. 2.3) can be defined as follows

$$u_i = P(u_i^*). \tag{2.24}$$

Similarly, the Helmholtz–Hodge decomposition can be applied to momentum equation. A vector field $F(u_i)$, can be uniquely decomposed into the sum of the solenoidal Eulerian acceleration vector and the irrotational pressure gradient, i.e.

$$F(u_i) = \frac{\partial u_i}{\partial t} + \frac{\partial p}{\partial x_i}, \tag{2.25}$$

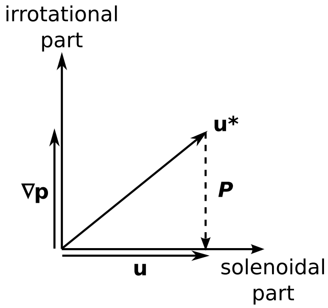

Figure 2.3: Helmholtz–Hodge decomposition of a vector $\boldsymbol{u}^*$.

where

$$F(u_i) = \frac{1}{\mathrm{Re}_D}\frac{\partial^2 u_i}{\partial x_j \partial x_j} - \frac{\partial u_j u_i}{\partial x_j} + f_i. \tag{2.26}$$

Note that the diffusive term is also solenoidal but not necessary tangential to the boundaries and therefore does not satisfy the orthogonality condition, see Eq. (2.23). Now a projection operator P_{ns} can be defined as

$$\frac{\partial u_i}{\partial t} = P_{\mathrm{ns}}(F(u_i)), \tag{2.27}$$

and can be written explicitly in the tensorial form as follows [47]

$$P_{\mathrm{ns}} = \boldsymbol{I} - \nabla\Delta^{-1}\nabla\cdot . \tag{2.28}$$

Equation (2.27) eliminates pressure from the momentum equation and, describes acceleration in terms of $F(u_i)$, a nonlinear functional of velocity. Therefore, this equation decouples the momentum equation from the continuity equation. However, the extreme complexity of the projection operator P_{ns} prevents a direct feasible numerical solution to the Eq. (2.27).

Initial projection schemes are designed as non–iterative pressure–correction methods that are composed of two main steps. In the first step, the momentum equation is decoupled from the continuity equation by doing an approximation to the projection operator P_{ns}. As the exact P_{ns} projection is never realized, a non–solenoidal preliminary velocity $\boldsymbol{u}^*$ is obtained at the end of this first step. Subsequently, in the second step, a further projection is required to impose the incompressibility condition and satisfy the mass-conservation. To this end, a Helmholtz–Hodge decomposition can be applied on $\boldsymbol{u}^*$ as described in Eq. (2.24).

The classical projection algorithms may be classified according to the pressure extrapolation they employ in the momentum step. According to this classification the two main classes are: the non-incremental projection method, and the incremental projection method [51]. The former uses simply no pressure gradient (zero-order approximation) in the momentum equation step. Chorin designed this first projection algorithm with the simplest choice of $P_{\mathrm{ns}} \approx I$ [26, 27]. In contrast, the incremental method employs a first order pressure extrapolation by constructing the pressure gradient using the pressure from the previous time step. Then, a Helmholtz–Hodge decomposition is applied on the intermediate field and the pressure increment is found. This class has been found more attractive due to increase in the accuracy without any extra computational demand compared to the non-incremental approach. The incremental method was first used by Goda [45]. Then, Van Kan [113] proposed a second-order accurate scheme in velocity which combines the incremental algorithm with semi-implicit Crank-Nicolson time discretization. For comprehensive reviews of higher–order projection methods please refer to [21, 51, 6].

As discussed above, projection methods are theoretically based on the Helmholtz–Hodge decomposition which is defined for enclosed flows (cf. Eq. (2.23)). However, Guermond et al. [51] demonstrated that similar accuracy and stability behaviour is expected for the flows with open boundaries, where $u_i n_i|_{\partial\Omega_o} \neq 0$ at least on some portion Ω_o of the boundary Ω.

2.4.2 An incremental projection scheme

In this section, an incremental projection scheme is presented. In order to ease the description, the algorithm is first given in spatially continuous framework. The reader is referred to Section 2.4.3 for the spatial discretization on collocated grids. Moreover, for reasons of brevity, only Dirichlet boundary conditions are considered. Using a one–step theta scheme with a semi-implicit convective term, cf. Section 2.3, the basic steps of the incremental projection scheme read as follows:

1. Momentum step: Given u_i^n and p^n from the previous time step, solve for the preliminary velocity $\tilde{u}_i^{n+1}$;

$$\frac{\tilde{u_i}^{n+1} - u_i^n}{\delta t} + u_j^{n-1/2}\frac{\partial \tilde{u_i}^{n+\theta}}{\partial x_j} = \frac{1}{\mathrm{Re}_D}\frac{\partial^2 \tilde{u_i}^{n+\theta}}{\partial x_j \partial x_j} - \frac{\partial p^n}{\partial x_i} + f_i^{n+1} \qquad \text{in } \Omega, \tag{2.29}$$

$$\tilde{u}_i^{n+1} = g_i^{n+1} \qquad \text{on } \partial\Omega, \tag{2.30}$$

where

$$\tilde{u_i}^{n+\theta} = \theta \tilde{u}^{n+1} + (1-\theta)\, u^n, \tag{2.31}$$

$$u_i^{n-1/2} = 1.5 u_i^n - 0.5 u_i^{n-1}. \tag{2.32}$$

2. Projection step: Perform the projection $u_i{}^{n+1} = P(\tilde{u_i}^{n+1})$;

$$\frac{(u_i{}^{n+1} - \tilde{u_i}^{n+1})}{\delta t} + \frac{\partial (p^{n+1} - p^n)}{\partial x_i} = 0 \qquad \text{in } \Omega,$$

by solving first

$$\frac{\partial^2 \left(p^{n+1} - p^n\right)}{\partial x_i \partial x_i} = \frac{1}{\delta t}\frac{\partial \tilde{u_i}^{n+1}}{\partial x_i} \qquad \text{in } \Omega, \tag{2.33}$$

$$\frac{\partial \left(p^{n+1} - p^n\right)}{\partial x_i} n_i = 0 \qquad \text{on } \partial\Omega, \tag{2.34}$$

then, updating the velocity

$$u_i^{n+1} = \tilde{u_i}^{n+1} - \delta t \frac{\partial \left(p^{n+1} - p^n\right)}{\partial x_i}, \qquad \text{in } \Omega, \tag{2.35}$$

$$u_i^{n+1} = g_i^{n+1} \qquad \text{on } \partial\Omega. \tag{2.36}$$

In this incremental projection scheme, we apply the same boundary conditions on the preliminary $\tilde{u_i}^{n+1}$ and the final $u_i{}^{n+1}$ velocity fields, cf. Eq. (2.30) and Eq. (2.36). However, in various realizations of the algorithm these boundary conditions may differ, please refer to [48] for a discussion. The presented scheme yields a second order splitting error, i.e., $\mathrm{O}(\delta t^2)$, in velocity and a first order error, i.e., $\mathrm{O}(\delta t)$, in pressure [51]. The reduced accuracy in pressure is caused by the unphysical boundary condition in Eq. (2.34). This unphysical Neumann boundary condition creates spurious boundary layers around the boundaries and therefore yields an overall reduction in the pressure accuracy [47].

If the Crank–Nicolson scheme is employed for time–marching, i.e., $\theta = 0.5$, the order of the additional segregation error is consistent with time–marching error for velocity fields. Therefore, the PISO algorithm can be replaced with the proposed scheme without suffering a reduction in accuracy. This is verified in Section 2.4.4.

2.4.3 Discretization on collocated grids

This section is devoted to the spatial discretization of the projection scheme described in Equations (2.29)–(2.36). Therefore, all the variables are discrete. In Section 2.2, we used a superscript k to denote the variables at cell centroids. In this section, this notation is dropped to avoid an overuse of superscripts. If the evaluation is done on the face centroid, it is explicitly shown with f, otherwise it is at cell centroids.

Discretization of the momentum step in Equations (2.29)–(2.32), closely resembles the discretization in Section 2.2, and therefore is not repeated here. Only a final remark about the linearization of the convective term is made at the end of the section.

In order to discretize the pressure Poisson equation in Eq. (2.33), the equation is first reformulated in the weak form, and then suitable weighting functions with local support in the element are introduced. Subsequently, the Gauss–Divergence Theorem in combination with the midpoint rule is applied and the following element equation is obtained

$$\sum_{f=1}^{N_{kf}} \left(\frac{\partial p^{n+1}}{\partial x_i} \right)^f n_i^f |\partial \Omega_k^f| = \sum_{f=1}^{N_{kf}} (\tilde{u}_i^{n+1})^f n_i^f |\partial \Omega_k^f| + \sum_{f=1}^{N_{kf}} \left(\frac{\partial p^{n}}{\partial x_i} \right)^f n_i^f |\partial \Omega_k^f|, \quad (2.37)$$

where the superscript f denotes that the evaluation is done on the face centroids, $|\Omega_k^f|$ is the area of the face and $\boldsymbol{n}^f$ is its corresponding unit normal. Further, N_{kf} is the total number of faces around the element. The approximation to the pressure gradient on the face centroid in Eq. (2.37) is done using central differencing with a non–orthogonal correction as described in Eq. (2.14).

The velocity flux $(\tilde{u}_i^{n+1})^f n_i^f$ is not directly approximated by using ϕ_f, cf. Eq. (2.13), as this approach leads to the well known odd–even decoupling problem on collocated grids [117]. An additional term using a pressure–weighted interpolation, also known as the Rhie–Chow interpolation [103], is added to the velocity flux to avoid this problem. Consequently, this step reads as follows

$$\begin{aligned}\tilde{\phi}_{fp}^{n+1} &= \tilde{\phi}_f^{n+1} + \left(\overline{\left(\frac{\delta p^n}{\delta x_i}\right)} n_i^f - \frac{(p^n)^{c2} - (p^n)^{c1}}{\left| n_i^f d_i \right|} \right) |\partial\Omega_k^f| \delta t, \qquad (2.38)\\ &\approx (\tilde{u}_i^{n+1})^f n_i^f |\partial\Omega_k^f|,\end{aligned}$$

where

$$\frac{\delta p}{\delta x_i} = \sum_{f=1}^{N_{kf}} p^f n_i^f, \qquad (2.39)$$

is the pressure gradient approximation at the centroid of the cell, and $\overline{(\cdot)}$ represents linear interpolation to the face centroid as defined in Eq. (2.12). Further, $c1$ and $c2$ are the face neighbouring cell centroids, and $\boldsymbol{d}$ is the vector connecting $c1$ and $c2$, cf. Fig. 2.2.

Applying Eq. (2.14) and Eq. (2.38) to Eq. (2.37), a linear system of equations is obtained which can be solved for p^{n+1}. After the new pressure p^{n+1} is obtained, the velocity u_i^{n+1} at the cell centroids and velocity flux vectors ϕ_{fp}^{n+1} at the face centroids are updated separately as follows

$$\phi_{fp}^{n+1} = \tilde{\phi}_{fp}^{n+1} - \delta t \left(\frac{(p^{n+1} - p^n)^{c2} - (p^{n+1} - p^n)^{c1}}{\left| n_i^f d_i \right|} \right) |\partial\Omega_k^f|, \qquad (2.40)$$

$$u_i^{n+1} = \tilde{u}_i^{n+1} - \delta t \frac{\delta(p^{n+1} - p^n)}{\delta x_i}. \qquad (2.41)$$

The reason for the distinctive update of the flux field ϕ_{fp}^{n+1} is that this flux field satisfies the mass balance where $\overline{(u_i^{n+1})} n_i |\partial\Omega_k^f|$ does not. Thus, ϕ_{fp} is also employed in the linearised convective term in the next time step, i.e.,

$$\sum_{f=1}^{N_{kf}} (u_i^{n+1})^f (u_j^{n+1})^f n_j^f |\partial\Omega_k^f| \approx \sum_{f=1}^{N_{kf}} \overline{(u^{n+1})} (\frac{3}{2}\phi_{fp}^n - \frac{1}{2}\phi_{fp}^{n-1}). \qquad (2.42)$$

2.4.4 Verification

In this section, the accuracy of the projection scheme introduced in Sections 2.4.2 and 2.4.3 is tested. A classical benchmark case to verify the time accuracy of incompressible flow problems is the so–called Taylor–Green vortex first used by Kim and Moin [72]. Taylor–Green vortex flow is an unsteady incompressible flow of a periodic array of vortices that exhibit exponential decay in time due to viscous dissipation. This flow has an exact closed form solution which reads for the two–dimensional case as follows

$$u_1^r(x_1, x_2, t) = -\cos(2\pi x_1)\sin(2\pi x_2)e^{-8\pi^2 \nu t}, \tag{2.43}$$

$$u_2^r(x_1, x_2, t) = \sin(2\pi x_1)\cos(2\pi x_2)e^{-8\pi^2 \nu t}, \tag{2.44}$$

$$p^r(x_1, x_2, t) = -\frac{1}{4}\left(\cos(4\pi x_1) + \cos(4\pi x_2)\right)e^{-16\pi^2 \nu t}. \tag{2.45}$$

The case is solved over a domain $\Omega = [0, 1] \times [0, 1]$ for a time interval of $t \in (0, 1]$. Periodic boundary conditions are applied for all the field variables. Initial fields are obtained from Eq. (2.43)–(2.45), i.e., $u_i(x_i, 0) = u_i^r(x_i, 0)$ and $p(x_i, 0) = p^r(x_i, 0)$. A kinematic viscosity of $\nu = 0.01$ is selected.

The domain Ω is discretized with a fine uniform grid of 256 × 256 quadrilateral elements in so that errors induced by the temporal discretization dominate. The spatial discretization is carried out with collocated FVM as described in section 2.2. For the temporal discretization a semi–implicit Crank–Nicolson method with second order extrapolation for convective term is employed (cf. Section 2.3). Tolerances for all the linear solvers are set to machine accuracy. An error measure E_u is defined for the velocity using L_2 norm $\| \cdot \|_0$, i.e.,

$$E_u(t) = \frac{\|\boldsymbol{u}(x_i, t) - \boldsymbol{u}^r(x_i, t)\|_0}{\|\boldsymbol{u}(x_i, t)\|_0}, \text{ with } \quad \|\boldsymbol{u}\|_0 = \left(\int_\Omega u_i u_i \mathrm{d}\boldsymbol{x}\right)^{1/2}. \tag{2.46}$$

The time step size δt is varied between 3.125×10^{-3} and 1.0×10^{-1} and $E_u(1)$ is evaluated with existing OpenFOAM® PISO solver *pisoFoam* and the newly implemented incremental projection scheme, entitled *projectionFoam*. In the pisoFoam test, the Poisson equation for the pressure is solved twice.

The results are shown in Figure 2.4 where second order accuracy is observed for both solvers. Thus, the implemented incremental projection scheme satisfies the theoretical second order accuracy in velocity. For this case, the additional error due to segregation is not noticeable.

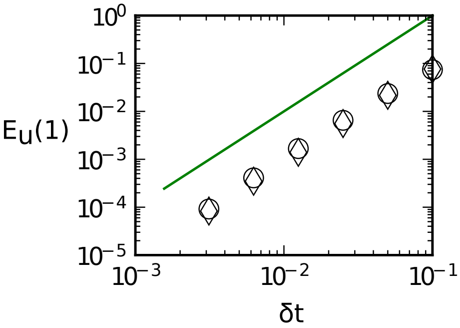

Figure 2.4: Error analysis for the Taylor–Green vortex case using Crank–Nicolson time integration. (○): *pisoFoam*; (◇): *projectionFoam*; (—): Slope 2;

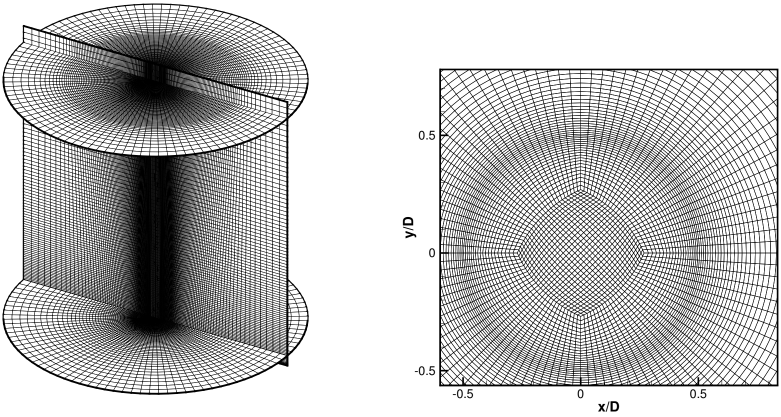

(a)

(b)

Figure 2.5: Computational grid. Every fifth line is shown. (a): slices of streamwise and spanwise cross-sections, $x = 0.5D$ and $x = 15.5D$ (b): zoom on a streamwise cross-section at $x = 0.5D$ close to the jet axis

2.4.5 Performance for DNS of a round jet

In Section 2.4.4 similar accuracy behaviour was shown for PISO and projection schemes. In this section, the focus is on the performance gain with the projection scheme. The main difference between the two algorithms on orthogonal grids is that PISO algorithm solves the Poisson equation multiple times. On non–

Table 2.1: Performance of PISO and Projection schemes for a DNS round jet case

Scheme	# outer iter.	# inner iter.	elapsed runtime	relative cost
PISO	2	3	119.39s	1
Projection	1	3	66.12s	0.5538

orthogonal grids, both algorithms do additional loops on the Poisson equation due to the deferred correction approach presented in Section 2.2. Overall, the projection scheme does less iterations on the Poisson equation and the effect of this is quantified here for a DNS case of a round jet at $\mathrm{Re}_D = 2000$. This DNS case is the original configuration that is used in the active control studies in chapter 4.

A cylindrical computational domain is selected which extends $L = 16D$ in axial direction and $R = 8D$ in radial direction. A multiblock-structured grid using hexahedral elements with a square-shaped central block and an O-grid formed of surrounding blocks is constructed (cf. Fig. 2.5). The grid resolution is fixed to $130(x) \times 130(y) \times 475(z)$ elements for the core region and $470(r) \times 520(\theta) \times 475(z)$ elements for the O-grid region, totalling to around $125 \cdot 10^6$ elements. Close to the jet inlet, the grid elements are clustered in the jet core region, especially in the shear layer. This cluster region expands radially moving downstream following the expected jet spreading.

Both projection and PISO schemes require in each time step the solution of the linear system of convection-diffusion like equations for the velocity fields. This is done by using the biconjugate gradient iterative solver with a diagonal incomplete LU preconditioner up to a solution tolerance of 10^{-9}. The second step requires solving a discretized Poisson equation for the pressure which is achieved by using a conjugate gradient solver with a geometric-algebraic multigrid preconditioner. The tolerance for initial iterations is 10^{-7} and the final Poisson solution is obtained with a tolerance of 10^{-10}. As the grid contains regions of cells with a degree of non-orthogonality (max. approx. $30°$), two additionals Poisson solutions for non-orthogonal corrections are employed to ensure second order spatial accuracy. This makes three Poisson solutions overall, which are denoted as inner iterations. Moreover, for PISO scheme two outer iterations are specified. The PISO scheme supplied with single outer iteration delivers unstable results.

The simulations are run on 156 processors of the *Thinking* infrastructure of the Flemish Supercomputer Center (VSC) which is equipped with an QDR Infiniband communication network. Each simulation is run for 3600 s only, as we noticed that the cost per time step changes less than $< 2\%$ and fluctuates around the same values.

The obtained data are reported in Table 2.1. For this particular case, solving the Poisson equations dominates the overall simulation cost. Therefore, the projection scheme allows a performance gain of about 45%. This result is by no means generic and it is highly dependent on the case, the iterative linear system solver and the hardware infrastructure. However, it marks the importance of employing the projection scheme in DNS studies in further sections in order to allow a noticable performance gain without losing the accuracy in the prediction of velocity fields. Considering the size of a DNS problem, 45% cost reduction is an essential advantage.

Chapter 3

Parallelization of statistical averaging

Similar to most of the general-purpose CFD codes, OpenFOAM® employs a basic non–overlapping grid partitioning for parallel computations. In this approach, each partition solves the same set of domain equations with the corresponding local partition boundary conditions. At the end of the each time step, these boundary conditions are updated by exchanging the data on the inter-partition boundaries. This updating operation can cause a significant communication overhead with increasing number of partitions, and can yield a poor parallel scaling of the code. This poor parallel scaling is an essential bottleneck in conducting high-fidelity turbulent flow simulations with generic flow solvers. In this chapter, a statistical averaging method is discussed that partly overcomes this bottleneck and improves the scalability of OpenFOAM® for round jet DNS. The methodology is designed for statistically stationary flows, and therefore also applicable to LES.

In DNS of turbulent flows, the chaotic and strongly fluctuating velocity fields associated to turbulence, are directly represented in the simulations. For practical purposes, these three-dimensional time-varying velocity fields need to be averaged, yielding mean-velocity profiles, Reynolds stresses, and similar turbulent-flow quantities. Formally, averaging in turbulence is defined using the average over an ensemble of statistical independent realizations of the same flow. For turbulent flow systems that are statistically stationary, the ensemble average is in practice replaced by averaging the solution in time. To this end, simulations are first run for some period of time T_i in which the flow starts from an initial condition (usually constructed for some part using random velocities), and subsequently settles into a statistical equilibrium. Afterwards, averaging in time is performed over a period of time T_s which needs to be sufficiently long to acquire statistically converged mean-flow quantities.

In order to be able to parallelize the averaging of the turbulent solution in DNS or LES of statistically stationary flows, we propose to partially resort back to the definition of an ensemble average, i.e., we propose to build a set of R statistical independent realizations of the same flow, which can be simulated independently (in parallel), with an interval for time averaging which is now reduced to T_s/R.

Two different approaches to build an ensemble with statistically independent members are studied. The first approach is straightforward and resembles an approach proposed by Carati et al. for dynamic subgrid-scale models [22]. Here, all the simulations are started simultaneously with a white noise superimposed on their mean inflow profiles and therefore they are statistically independent by default. This simple approach suffers an overhead because of multi-initialization, and is therefore not very ideal for flows where initialization and statistical averaging have comparable runtimes.

In a second approach, we run the initialization only once, and construct different members of an ensemble by adding three-dimensional random perturbations to the solution when it reaches a statistical equilibrium. Following the addition of random noise, the simulation in each member of the ensemble settles back rapidly into statistical equilibrium. However, the fields of interest in individual simulations are still correlated for another additional time period which we denote as decorrelation timescale T_d. After this decorrelation time, all simulations become statistically independent and parallel statistical averaging can be started.

The chapter is organized as follows. In Section 3.1, we derived new speed-up and efficiency expressions, including the additional cost due to the decorrelation timescale T_d. An important part in the methodology is the correct characterization of the initialization timescale T_i, and the decorrelation timescale T_d for the turbulent flow application, which is discussed in Section 3.2. Finally, in Section 3.3, the applicability of this approach is demonstrated using DNS of a round jet case.

3.1 Statistical ensemble and parallelization

In the current section, we briefly review some definitions related to the averaging of turbulence, as required in DNS or LES. These concepts may be found in most standard textbooks on turbulent flows, such as, e.g. Pope [100] and Tennekes and Lumley [109].

Instantaneous fields in turbulent flows are the result of nonlinear interactions of different scales which evolve in chaotic manner. Although these fields show seemingly random and unpredictable behavior their statistical properties are repeatable. Thus many aspects of turbulent flows can be efficiently studied using mean flow states. To formally define mean-flow properties, such as the average velocity field $\langle \boldsymbol{u} \rangle$, ensemble averaging is used, i.e.,

$$\begin{aligned} \langle \boldsymbol{u}(\boldsymbol{x},t) \rangle &= \lim_{R\to\infty} \langle \boldsymbol{u}(\boldsymbol{x},t) \rangle_R\,, \\ &= \lim_{R\to\infty} \frac{1}{R} \sum_{r=1}^{R} \boldsymbol{u}^{\{r\}}(\boldsymbol{x},t), \end{aligned} \tag{3.1}$$

where $\boldsymbol{u}^{\{r\}}$ $(r = 1 \cdots R)$ are a set of independent realizations of the same turbulent flow (e.g. obtained from repeated experiments). For practical purposes, the ensemble $\langle \boldsymbol{u} \rangle$ may be estimated using $\langle \boldsymbol{u} \rangle_R$ $(R \gg 1)$, with an error which decreases proportionally to $R^{-1/2}$ (cf. e.g. [100]). Performing this average in the context of DNS or LES, requires R different simulations, with boundary conditions and initial conditions that are slightly perturbed (e.g. using low-amplitude random noise), such that the evolving turbulent flow fields are statistically independent.

In case the flow is statistically stationary and ergodic, the ensemble averaging may be defined in a more convenient way, i.e. by using a time average

$$\begin{aligned} \langle \boldsymbol{u}(\boldsymbol{x}) \rangle &= \lim_{T_s\to\infty} \langle \boldsymbol{u}(\boldsymbol{x}) \rangle_{T_s} \\ &= \lim_{T_s\to\infty} \frac{1}{T_s} \int_{t_0}^{t_0+T_s} \boldsymbol{u}(\boldsymbol{x},t)\ \mathrm{d}t. \end{aligned} \tag{3.2}$$

For practical purposes, the ensemble $\langle \boldsymbol{u} \rangle$ may be estimated using $\langle \boldsymbol{u} \rangle_{T_s}$. To this end, the averaging interval should contain a sufficient number of independent realizations of the turbulent flow. This is the case provided that sufficient integral time scales are elapsed during time averaging. Thus, for a good average, $T_s/\mathcal{T} \gg 1$ is required, with an error decreasing proportionally to $(T_s/\mathcal{T})^{-1/2}$. Obviously, Eq. (3.1), and (3.2) may be combined, leading to

$$\langle \boldsymbol{u}(\boldsymbol{x}) \rangle \approx \frac{1}{R} \sum_{r=1}^{R} \frac{R}{T_s} \int_{t_0}^{t_0+T_s/R} \boldsymbol{u}^{\{r\}}(\boldsymbol{x},t)\ \mathrm{d}t, \tag{3.3}$$

with $R \geq 1$, and $T_s/\mathcal{T} \gg 1$.

In DNS, or LES, of statistically stationary systems, Eq (3.2) is usually used for averaging. Generally, the time averaging time is so long that it covers many statistically independent sequential events. These events can be processed independently exploiting a fully parallelizable part of the problem. Hence in the current work, we propose to use the formulation of Eq. (3.3) instead, allowing us to run R statistically independent simulations concurrently (and without the need for parallel communications), while reducing the averaging time in each simulation to T_s/R.

We explore two different approaches to build up a statistical ensemble. In the first approach, all simulations start–up simultaneously and they are statistically independent by default because of random perturbations superimposed on their inflows. The idea itself is fairly straightforward, and was already suggested by Carati et al. [22] in the context of elaborating the ensemble averaging in a dynamic procedure using R different realizations (instead of averaging over homogeneous directions in space). The major drawback for this method is that all R simulations need to be initialized, and require a start–up run during which the initial velocity field evolves into statistical equilibrium. The required time T_i is typically of the order of a few through-flow times of the simulation domain; a more precise discussion is provided in Section 3.2.

Taking the non-parallelizable initialization time T_i into account in the proposed parallelization of ensemble averaging and allowing for grid partitioning in the R individual simulations, we end up with a parallel speed-up, and parallel efficiency respectively of

$$\begin{aligned} S_1(p,R) =& \frac{\mathbf{T}_1^w}{\mathbf{T}_P^w} = \frac{T_i+T_s}{T_i+T_s/R} S_g(p) = R\frac{k+1}{Rk+1} S_g(p), \\ =& S_{e1}(R) S_g(p), \end{aligned} \tag{3.4}$$

$$\begin{aligned} E_1(p,R) =& \frac{\mathbf{T}_1^c}{\mathbf{T}_P^c} = \frac{T_i+T_s}{RT_i+T_s} E_g(p) = \frac{k+1}{Rk+1} E_g(p), \\ =& E_{e1}(R) E_g(p), \end{aligned} \tag{3.5}$$

where $k = T_i/T_s$, the superscript w and c denote the *wall-time*, and the *cpu-time* respectively, $P = pR$ is the total number of processors with p being the number of processors in each simulation, and $S_g(p)$ is the speed-up due to grid partitioning and $E_g(p) = S_g(p)/p$ is the corredponding computational efficiency. Looking at these equations, it is appreciated that the efficiency of the proposed parallelization becomes very poor for $Rk \gtrsim 1$. Moreover, unless $k \ll 1$, the potential for speed-up is rather limited.

In the second approach, we explore a methodology to improve the efficiency of the ensemble parallelization for turbulent flows with $k \ll 1$. We propose to run only one simulation for the initial transient towards statistical equilibrium (with time T_i). Subsequently, we add R individual realizations of solenoidal random noise to the equilibrium solution. In this way, we obtain R distinct simulations, which are first run for a time T_d to establish statistical independency; then statistics are collected. The main premise in this approach is that the decorrelation timescale is considerably shorter than the initialization timecale (i.e. $T_d \ll T_i$). In Section 3.2, we show for the selected turbulent flow problem, turbulent round jet, that T_d is approximately 27% of T_i (which is in the order of the simulation through-flow time).

The speed-up and efficiency corresponding to the second method is now straightforward. We introduce the additional definitions $k_D = T_d/T_s$, and obtain

$$\begin{aligned} S_2(p,R) =& \frac{\mathbf{T}_1^w}{\mathbf{T}_P^w} = \frac{R(k+1)}{Rk + Rk_D + 1} S_g(p) \\ =& S_{e2}(R) S_g(p), \end{aligned} \tag{3.6}$$

$$\begin{aligned} E_2(p,R) =& \frac{\mathbf{T}_1^c}{\mathbf{T}_P^c} = \frac{k+1}{k + Rk_D + 1} E_g(p) \\ =& E_{e2}(R) E_g(p). \end{aligned} \tag{3.7}$$

3.2 Prediction of T_i and T_d

This section is devoted to the estimation of the initial transition timescale T_i, and the decorrelation timescale T_d. The performance of the methods described in Section 3.1 highly depends on these temporal dynamical characteristics and their relative behaviour. Thus, before applying the method to a turbulent case, a correct characterization of these quantities is essential. In the current section, an attempt is made to identify these timescales for an incompressible round jet case at $\mathrm{Re}_D = 2150$.

The selected test case has a cylindrical computational domain that extends $L = 17.5D$ in axial direction and $R = 8D$ in radial direction. No explicit turbulence model is used. Numerical discretization for the case is described in detail in Chapter 2. A block-structured grid with approximately 21×10^6

hexahedral elements is built. The time step size is fixed to $\delta t = 0.1D/U_J$, where D is the jet diameter and U_J is the jet exit velocity.

In order to estimate T_i, the statistically stationary turbulent flow is modelled as a linear system in steady-state. Using this simple model, we can characterize the transients in the simulation as basic system response and quantify these transients using well-known timescales in linear systems theory. To this end, first, certain global properties of the flow are monitored. For the turbulent round jet flow, we select the total kinetic energy E and enstrophy ε in a domain of interest Ω. These quantities are given by

$$E(t) = \frac{1}{2\,|\Omega|} \int_{\Omega} \boldsymbol{u}(\boldsymbol{x},t) \cdot \boldsymbol{u}(\boldsymbol{x},t) \mathrm{d}\boldsymbol{x}, \tag{3.8}$$

$$\varepsilon(t) = \frac{1}{2\,|\Omega|} \int_{\Omega} \boldsymbol{\omega}(\boldsymbol{x},t) \cdot \boldsymbol{\omega}(\boldsymbol{x},t) \mathrm{d}\boldsymbol{x}, \tag{3.9}$$

where $\boldsymbol{\omega} := \nabla \times \boldsymbol{u}$ is the instantenous vorticity. Subsequently, the evolution of these integral flow properties are modelled as the step response of a second order dynamical system [57], i.e.,

$$f(t) = \frac{A_1}{w_n^2} \left(1 - \frac{e^{-\zeta w_n t}}{\sqrt{1-\zeta^2}} \cos(w_d t - \psi) \right) + A_0, \tag{3.10}$$

with

$$w_d = \sqrt{1-\zeta^2} w_n, \qquad \psi = \tan^{-1}(\zeta / \sqrt{1-\zeta^2}).$$

Starting from an initial value A_0, the system evolves (or resorts back) eventually to a steady state value of $f_s = A_1/w_n^2 + A_0$. The required time to be in the %2 band of f_s is $4.6/(w_n \zeta)$ and is denoted as the settling time of the response. After this specific time instance, it is assumed that the system settles completely to steady state and the effect of the transient is over.

Using the response function $f(t)$, we perform least-squares curve fittings to time series of $E(t)$ and $\varepsilon(t)$ and measure the settling times T_1 and T_2 for the initialization transient, and the transient after the addition of random noise respectively. The resulting curves are plotted in Figures 3.1 and 3.2 and the corresponding time constants are listed in Table 3.1 and 3.2. We observed that the integral measure of kinetic energy does not show the effect of adding random noise to a statistically stationary field, and therefore it is not used to measure T_2. We notice that T_2 of ε is substantially shorter than T_1 of both quantities meaning that fluctuations due to random disturbances are quickly absorbed by the large-scale structures and background turbulence.

As the integral measure of kinetic energy exhibits slower dynamics and reaches the equilibrium later than enstrophy, T_1 for this quantity is more suitable

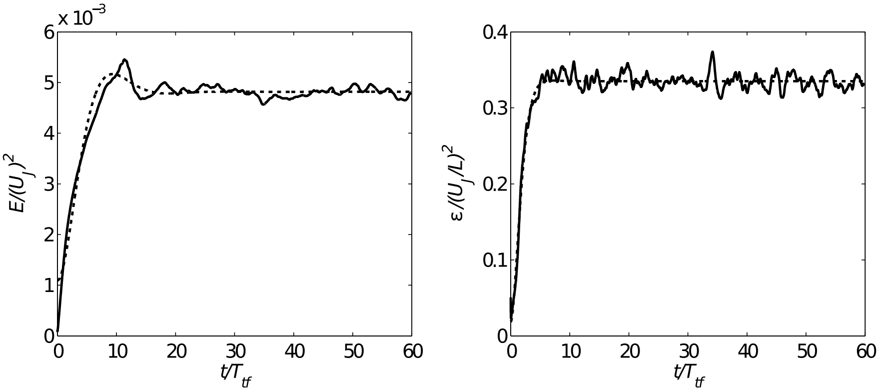

(a) kinetic energy (b) enstrophy

Figure 3.1: Evolution of integral measures at the simulation start-up. The domain length L and the jet exit velocity U_J are used for normalization. (—): time series for functions $E(t)$ and $\varepsilon(t)$ defined in Eq. 3.8 and Eq. 3.9 respectively; (- - -): fitted $f(t)$ curves using Eq. (3.10).

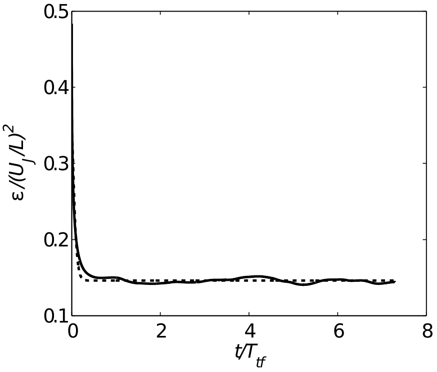

Figure 3.2: Evolution of integral measure for enstrophy after adding random perturbation to a statistically stationary field. See Fig. 3.1 for captions.

to model the duration of transient phase. If we assume that the round jet becomes statistically stationary following the settling time T_1 of $E(t)$, then the initialization timescale T_i is found by $T_i = T_1 = 18.2046T_{tf}$. T_{tf} is the through–flow time in a round jet and is defined as $T_{tf} = 1/2L/U_J$.

Table 3.1: The settling time T_1 for the initialization transient (normalized using the through flow time $T_{tf} = 1/2L/U_J$).

Quantity	w_n	η	T_1/T_{tf}
E	0.6012	0.4203	18.2046
ϵ	0.6920	0.9987	6.6566

Table 3.2: The settling time T_2 for the secondary transient following the addition random noise.

Quantity	w_n	η	T_2/T_{tf}	T_2/T_1
ϵ	26.1791	0.9984	0.1759	0.0097

T_i is estimated with a straightforward model, but estimation of T_d is more intricate. To this end, a statistical study is carried out which requires running hundreds of turbulent jet simulations. In order to keep the study in the feasibility margin, a grid coarsening, based on doubling the cell length in every coordinate direction, is applied to the computational grid described above.

The methodology is based on a generic averaging operation defined for arbitrary vector fields as follows

$$\langle \boldsymbol{u}(\boldsymbol{x},t)\rangle_C = \lim_{R\to\infty} \frac{1}{R}\sum_{r=1}^{R} \boldsymbol{u}^{\{r\}}(\boldsymbol{x},t). \tag{3.11}$$

If the vector fields are statistically independent, then $\langle \boldsymbol{u}(\boldsymbol{x},t)\rangle_C = \langle \boldsymbol{u}(\boldsymbol{x})\rangle$.

Following the addition of the low–amplitude three-dimensional random perturbations to the identical turbulent velocity fields, say at $t = 0$, the produced fields remain strongly correlated. As the time lapses as long as T_d, .i.e., $t = T_d$, these fields become statistically independent and the generic average $\langle \boldsymbol{u}(\boldsymbol{x},t)\rangle_C$ over these fields approaches the ensemble average $\langle \boldsymbol{u}(\boldsymbol{x})\rangle$, i.e.

$$\langle u_i(\boldsymbol{x},T_d)\rangle_C = \langle u_i(\boldsymbol{x},T_d+t)\rangle_C = \langle u_i(\boldsymbol{x})\rangle\,, \tag{3.12}$$

and

$$\left\langle u_i^c(\boldsymbol{x},T_d+t)u_j^c(\boldsymbol{x},T_d+t)\right\rangle_C = \left\langle u_i'(\boldsymbol{x})u_j'(\boldsymbol{x})\right\rangle, \tag{3.13}$$

where

$$u_i^c(\boldsymbol{x},t) = u_i(\boldsymbol{x},t) - \langle u_i(\boldsymbol{x},t)\rangle_C\,, \tag{3.14}$$

$\langle u_i(\boldsymbol{x})\rangle$ is the mean velocity component, and $\left\langle u_i'(\boldsymbol{x})u_j'(\boldsymbol{x})\right\rangle$ is the Reynolds Stress component of the statistically stationary field.

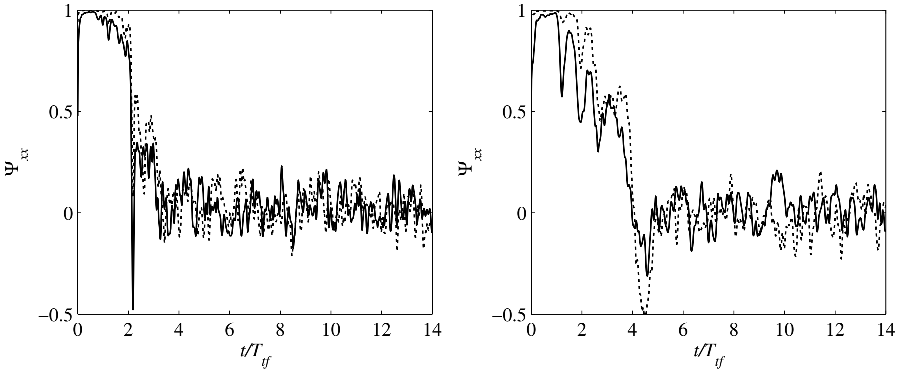

(a) $x = 15D$ downstream on axis (b) $x = 15D$ downstream, $r = D$ off-axis

Figure 3.3: Decay of correlation in time given by the measure Ψ in Equation (3.15) using random noise with an amplitude of $(\cdots)$: $0.05U_0$, (—): $0.15U_0$.

For $t < T_d$, there is a deviation between $\langle \boldsymbol{u}(\boldsymbol{x}, t)\rangle_C$ and $\langle \boldsymbol{u}(\boldsymbol{x}, t)\rangle$. In order to monitor the decay of this deviation in time, we propose a measure using second order moments

$$\Psi_{ij}(\boldsymbol{x}, t) = 1 - \frac{\left\langle u_i^c(\boldsymbol{x}, t) u_j^c(\boldsymbol{x}, t)\right\rangle_C}{\left\langle u_i'(\boldsymbol{x}) u_j'(\boldsymbol{x})\right\rangle}. \tag{3.15}$$

In contrast to the previous approach above using global measures in equations 3.8 and 3.9, Ψ is a local measure attached to a specific location in the domain. Thus, relevant sampling points from the domain have to be selected. Obviously, they should be located in the areas with slowest dynamics. For a round jet, these areas are the most downstream regions in the domain of interest and therefore two points slightly upstream from the outflow boundary at $x = 15D$, located on the axis ($r = 0$) and off the axis ($r = D$), are selected.

Two sets of numerical simulations, each set with $R = 250$ members, are conducted using random perturbations with maximum magnitudes of $0.05U_J$ and $0.15U_J$. The results for the axial component Ψ_{xx} are presented in Figures 3.3a and 3.3b. The other components delivered similar results. These figures demonstrate that the decorrelation timescale is not very sensitive to the magnitude of the perturbation. For the point on the axis, Ψ_{xx} reaches zero approximately in $t = 4T_{tf}$ and for the off-axis point it is $t = 5T_{tf}$. According to these results, we can roughly estimate the decorrelation timescale as $T_d \approx 5T_{tf}$ or $T_d \approx 0.27T_1 \approx 27.8T_2$.

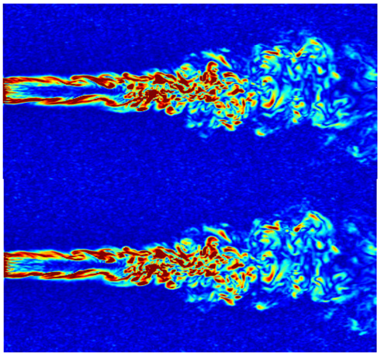

(a) $t = T_2$

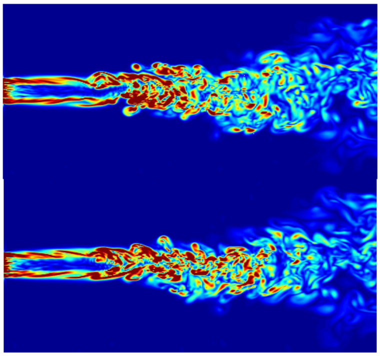

(b) $t = 0.5T_d = 13.9T_2$

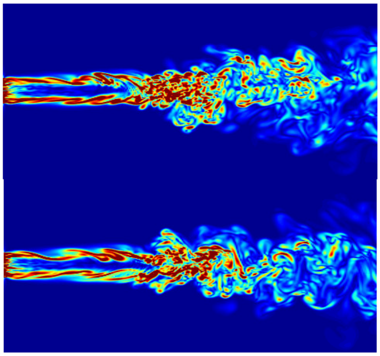

(c) $t = T_d = 27.8T_2$

Figure 3.4: Evolution of two jets following the addition of random noise using snapshots of $|\boldsymbol{\omega}|$.

Table 3.3: Parallel performance of OpenFOAM for Case *C1* in Chapter 4. Linear speed-up is assumed for $p = 64$ case.

p	64	128	156	256	512	624	1024	2048
t_{sim}	98.7	49.1	40.9	27.7	16.3	14.7	11.9	12.1
$S_g(p)$	64	128.65	154.44	228.04	387.63	423.94	530.82	522.04
$E_g(p)$	1	1.005	0.99	0.89	0.76	0.68	0.52	0.25

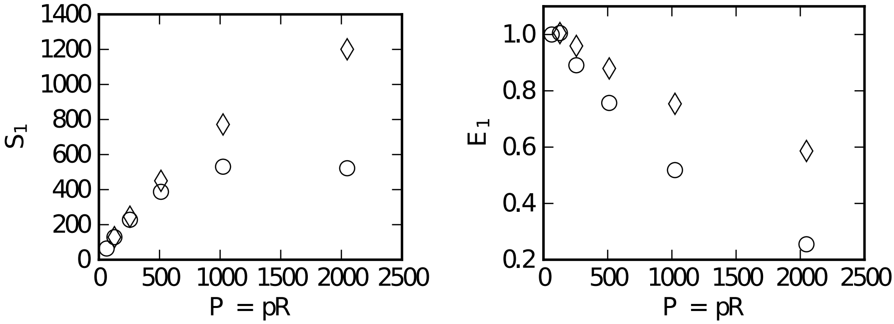

(a) speed-up (b) parallel efficiency

Figure 3.5: Parallel performance for two cases. ($\circ$) : $S_1(p, 1) = S_g(p)$ (only grid partitioning); ($\diamond$) : $S_1(p = 128, R = 1 \dots 16)$.

Figure 3.4 illustrates the evolution of two cases following the addition of the random perturbation with a maximum magnitude of $0.15U_J$ on the original grid with approximately 21×10^6 elements. At the time instance $t = 0.5T_d$ shown in Figure 3.4b, there are noticeable differences between the two flows, but similar vortical behaviour can be observed on the large scales. These similar flow trends on the large scales disappear when the decorrelation time scale $t = T_d$ is reached, cf. Figure 3.4c.

3.3 Application to a controlled round jet

In this section, the speed-up and efficiency of parallel statistical averaging for a controlled turbulent jet is evaluated. The computational details for this case is already given in Section 2.4.5 and the details about the flow configuration can be found in Section 4.1.1 in Case *C1*. The considered case has an initialization parameter of $k = 0.05$. The test environment is the *Tier1* supercomputer of the Flemish Supercomputer Center (VSC). *Tier1* has a total number of 8448 computer cores equipped with Intel Sandy Bridge microprocessor technology and FDR Infiniband Mellanox communication network.

The estimations in Section 3.2 demonstrated that in a turbulent round jet, the decorrelation timescale T_d is in the same order of magnitude as the transient timescale T_i. Thus, the second approach in Section 3.1 is not attractive for the current case and the first approach by Carati et al. [22] is employed to utilize parallel statistical averaging.

First, a scaling study is conducted. The Scotch library, included in the official OpenFOAM® distribution v2.1.x, is employed for grid partitioning. This package features a parallel graph partitioning algorithm which minimizes the boundaries between different partitions [1]. The results are reported in Table 3.3. Using the grid partitioning results in Table 3.3, the potential of parallel statistical averaging is explored by evaluating S_1 and E_1 in Equations (3.4) and (3.5) with $k = 0.05$, $p = 128$ and $R = 1 \ldots 16$. The results are illustrated in Fig. 3.5. It can be seen that the addition of ensemble averaging on top of grid partitioning parallelism improves the parallel performance. Therefore, the parallel statistical averaging concept developed in this chapter will be used in the DNS studies in Chapter 4.

Chapter 4

Active control with zero-net-mass-flux actuators

In this chapter, the near field of a zero-net-mass-flux (ZNMF) actuated round jet is studied using direct numerical simulations. The motivation is to investigate the typical flow patterns and their effect on key jet parameters and to make connections to the bulk literature of jet flow. The Reynolds number of the jet $\mathrm{Re}_D = 2000$, and three ZNMF actuators are used, evenly distributed over a circle and directed towards the main jet. The actuators are triggered in phase, and have a relatively low momentum coefficient of $C_\mu = 0.0049$ each. We study four different control frequencies, with Strouhal numbers ranging from $\mathrm{St}_D = 0.165$ to $\mathrm{St}_D = 1.32$; next to that, also two uncontrolled baseline cases are included in the study.

The work discussed in this chapter is published in A. Önder & J. Meyers, Phys. Fluids (2014) [95]. The structure of this chapter is as follows. First, the computational details and flow configuration are described in Section 4.1. Then we will analyse the features of the instantaneous flow field in Section 4.2. Subsequently, first and second order statistics are discussed in Section 4.3, and the passive scalar evolution and scalar transport tubes are presented. Finally, conclusions are presented in Section 4.4.

4.1 Methodology and computational set-up

In the current section, we define the flow configuration in Section 4.1.1. Subsequently, computational details are presented in Section 4.1.2, followed by a grid-assessment study in Section 4.1.3.

4.1.1 Flow configuration

All the cases considered in this work have a Reynolds number of $\mathrm{Re}_D = 2000$ and a Schmidt number $Sc = 1.0$. At this Reynolds number the flow is initially laminar and becomes turbulent downstream. Direct numerical simulations are carried out without any further turbulence-modelling assumptions.

The inflow profile is essential in the description of the flow as it plays a crucial role in the near field flow development. In the present study, we specify a uniform velocity U_J in the core region of the jet, and laminar Blasius profile in the vicinity of the wall similar to previous numerical work [71]. The associated inlet momentum thickness, defined as

$$\theta_0 = \frac{2}{D} \int_0^{D/2} \frac{U_x(r)}{U_J} \left(1 - \frac{U_x(r)}{U_J}\right) r \, \mathrm{d}r, \tag{4.1}$$

corresponds to $D/2\theta_0 \approx 88$ in our study.

For the control of the main jet we employ three ZNMF actuators distributed evenly in circumferential direction and placed $0.625D$ away from the jet centreline, and inclined at an angle of $\alpha = 30°$ with the jet centreline (cf. Figure 4.1). The ZNMF actuators and cavities are not represented in full detail, but instead, the actuators are modelled as an oscillating inlet-velocity boundary condition on the wall, with

$$u_a = U_a \sin(2.0\pi f_a t). \tag{4.2}$$

This simple control model is inspired by experimental phase locked velocity measurements on the centreline of a synthetic jet with a step [44]. Such an oscillatory velocity boundary condition is able to produce synthetic jets featuring a well-organized train of vortex rings as previously shown in Ref. [76]. The boundary condition is imposed on an elliptic actuation surface, i.e. resulting from the $\alpha = 30°$ inclination of the ZNMF jets (cf. Figure 4.1). The individual actuators have a momentum coefficient of $C_\mu = 0.0049$ and a ratio between actuation velocity to main jet velocity of $U_a/U_J = 1$. All the controls are in phase, manipulating the axisymmetric modes of the main jet.

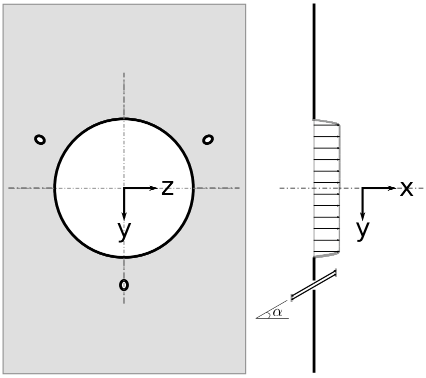

Figure 4.1: Configuration of the actuators.

The different simulation cases studied in this work are listed in Table 4.1. First of all, two baseline cases without any control are included. In fact, in absence of any other perturbations, we observed for uncontrolled simulations a rather late transition to turbulence. Since all controlled cases in the current work display an early transition, the two baseline cases contain additional random perturbations on the jet inlet profile. In the first baseline case (*B1*) these have an amplitude of $u'_J = 0.015U_J$ (with u'_J the rms value), while in the other baseline case (*B2*) a higher amplitude of $u'_J = 0.075U_J$ is used.

We further assume that the Strouhal number ($\mathrm{St}_D = fD/U_J$) of the jet preferred mode $\mathrm{St}_{pm} = 0.33$ — for Case *B2* we observed a peak in the velocity spectra at this Strouhal number. This value is consistent with the experimental results in Ref. [37] considering our initial boundary layer thickness with $D/2\theta_0 \approx 88$. Four control cases are then considered (cf. Table 4.1), i.e. with control frequencies of $\mathrm{St}_D = 0.165$, $\mathrm{St}_D = 0.33$, $\mathrm{St}_D = 0.66$ and $\mathrm{St}_D = 1.32$, or ranging from one half (*C0.5*) up to four times (*C4*) the Strouhal number of the preferred mode. In the controlled cases the perturbation level on the baseline jet is reduced to $u'_J = 0.0015U_J$, in order to prevent that the uncontrolled excitation by white noise becomes more dominant for the flow development than the ZNMF actuation with only a momentum coefficient of $C_\mu = 0.0049$.

4.1.2 Computational details

The open-source C++ library OpenFOAM® is employed in this study (using the v2.1.x distribution). The details of the discretization are discussed in Chapter 2.

Table 4.1: Nomenclature and control parameters of investigated cases. (St_D): actuation frequency, (u'_J/U_J): background turbulence level, (C_μ): momentum coefficient for individual actuators

Cases	*B1*	*B2*	*C0.5*	*C1*	*C2*	*C4*
St_D	0	0	0.165	0.33	0.66	1.32
u'_J/U_J	0.015	0.075	0.0015	0.0015	0.0015	0.0015
C_μ	0	0	0.0049	0.0049	0.0049	0.0049

A cylindrical computational domain is selected which extends $L = 16D$ in axial direction and $R = 8D$ in radial direction. The computation grid described in Section 2.4.5 (cf. Figure 2.5) is also used for the current DNS experiments.

In the simulations, the time step size is fixed to $\delta t = 0.004DU_J^{-1}$, enabling us to resolve one period of actuation for the highest frequency case (*C4*) with 200 time steps. The initialization of simulations take $T_i = 16DU_J^{-1}$. Afterwards we collect the statistics for a time interval of $T_s = 320DU_J^{-1}$. For instance, for case *C1*, this relates to 20 cycles of actuation during the initial transient T_i, and 400 cycles during the statistical sampling time T_s.

The boundary conditions at lateral and outflow boundaries correspond respectively to $\partial u_i/\partial r = 0$, and $\partial u_i/\partial x = 0$. No inflow is allowed on the outflow boundary. The ZNMF inlet boundary (cf. Eq. 4.2) is treated in a special way. Instead of body-fitting the mesh to the elliptic ZNMF openings, we instead project the effect of actuation on the DNS grid using a two–dimensional axisymmetric convolution filter. The actuators are located in regions discretized with an O-grid, where grid lines are aligned with a cylindrical coordinate system having the jet centreline as reference axis. Applying filtering in this coordinate system the filtered actuation velocity at the center of a face element corresponds to

$$\tilde{\boldsymbol{u}}_a(r_h, \theta_h) = \iint \boldsymbol{u}_a(r, \theta)\, G(r - r_h)\, G(\theta - \theta_h)\, r_h \,\mathrm{d}\,\theta \mathrm{d}r \tag{4.3}$$

where r_h , θ_h are the radial distance and angular position of the cell center respectively, and $G(r)$ is the filter kernel $G(r) = (6/\pi\Delta^2)^{1/2}\exp(-6r^2/\Delta^2)$ with filter width $\Delta = 1.5h_r$ (where h_r is the cell size in radial direction).

The simulations are conducted on *Tier1* supercomputer of the Flemish Supercomputer Center (VSC). In order to improve parallel scaling, parallel statistical averaging method is applied, cf. Chapter 3 for details. According to the data in Table 3.3 in Chapter 3, the code exhibits linear speed-up up to $p = 156$ processors. Thus, for the current study we selected a configuration of $p = 156$ and $R = 4$. This configuration delivers an overall speed-up of

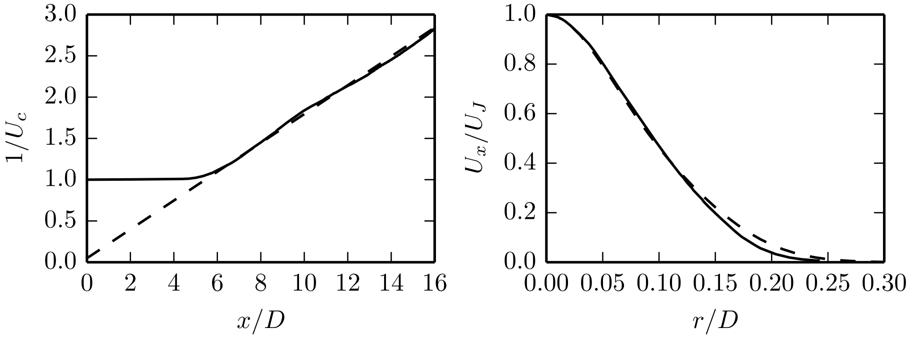

(a) axial velocity (b) turbulent kinetic energy

Figure 4.2: Literature benchmark of baseline data. (a) decay rate for centerline velocity: $U_c = \langle u_x \rangle_{r=0}$; (b) self-similar profile for axial velocity U_x. (—): case B2; (−−): experimental data in Ref. [62]

.

$S_e = 540.56$ and $E_e = 0.87$ on $P = 624$ processors, where $S_g(624) = 423.94$ and $E_g(624) = 0.68$ only.

4.1.3 Grid Assessment

Before analyzing the different control cases in detail in next sections, we first perform a grid-assessment study. To this end, we first benchmark the baseline case B2 with a well known experimental work from literature [62]. The comparison is limited to the first order statistics as these are less sensitive to initial conditions and Reynolds number, and converge relatively fast to self-similar profiles downstream. In Figure 4.2 the decay rate for the centerline axial velocity $U_c = \langle u_x \rangle_{r=0}$ and self-similar profile for axial velocity are shown. Numerical results for these quantities are in very good agreement with experimental data except some minor discrepency for $r/D > 0.15$ in the self-similar profile.

Additionally, we perform a grid sensitivity study. We construct a number of grids for the control case *C1*, and compare statistically averaged results. Two coarser meshes and one finer mesh are constructed, so that we can compare four grid levels, i.e. Level I (coarsest), Level II (intermediate), Level III (original resolution) and Level IV (finest). Details are provided in Table 4.2 along with the original case (Level III). On the coarser-grid simulations, we further increased the time step to $\delta t = 0.0064 D U_J^{-1}$ and on Level IV reduced it to $\delta t = 0.0032 D U_J^{-1}$.

In a first step, the evolution of the mass flux $\dot{m}(x)$ and energy flux $\phi_E(x)$ as function of downstream distance x are investigated. These are also used in further sections, and are respectively defined as

$$\dot{m}(x) = \int_0^{2\pi} \int_0^{\infty} \langle u_x \rangle \, r \, \mathrm{d}r \, \mathrm{d}\theta, \tag{4.4}$$

and

$$\phi_E(x) = \int_0^{2\pi} \int_0^{\infty} \frac{1}{2} \langle u_i \rangle \langle u_i \rangle \langle u_x \rangle \, r \, \mathrm{d}r \, \mathrm{d}\theta, \tag{4.5}$$

and where we numerically evaluate the inner integral up to $8D$ in practice (instead of ∞).

In Figure 4.3a the normalized mass entrainment by the jet, $\dot{m}(x)/\dot{m}(0)$, is shown for the different grid resolutions. It is appreciated that the entrainment is well predicted on all grid levels. In particular results of the intermediate, original and finest grid level collapse, except for some small differences at the end of the simulation domain for $x > 10D$. In Figure 4.3b the normalized energy flux $\phi_E(x)/\phi_E(0)$ is shown, with also a very good collapse of results for all grid levels.

We now turn to some flow properties that do not benefit from any form of plane averaging (unlike Eqs. 4.4 or 4.5). First of all, in Figure 4.4a the evolution of the centreline axial velocity $U_c = \langle u_x \rangle_{r=0}$ is shown for the different grid levels. We observe that grid convergence for this property is more challenging. In particular results on the coarsest grid differ considerably. The intermediate and original grid yield collapsing centerline velocities up to $x = 10D$; beyond that, some differences also occur. The two finest levels have the best agreement as their centerline velocities nicely collapse except for some minor differences in the region $7D < x < 9D$.

Finally, we look at second-order statistics along the centerline of the jet in Figure 4.4b, i.e. the evolution of the centerline turbulent kinetic energy $k_c = 0.5\langle u_i' u_i' \rangle_{r=0}$ (with $u_i' = u_i - \langle u_i \rangle$). It is seen that results for the original grid have a very good collapse with the ones of the finest case up to $x = 6D$. Beyond that, significant differences occur. Thus for this last property, grid convergence could not be ascertained for $x > 6D$. Therefore we will limit the discussions on second order statistics to a smaller domain with a length of $6D$. We further investigated the grid convergence of the second-order statistics in this smaller domain by looking at the turbulent kinetic energy contours on transverse planes (not shown here), and found that up to $6D$ the results on the original and reference grid are practically indistinguishable.

Table 4.2: Employed grids for sensitivity studies. Level III is the original grid used in next sections.

Level	Core region	O-Grid	Total number of elements
I	$78 \times 78 \times 285$	$282 \times 312 \times 285$	26 809 380
II	$104 \times 104 \times 380$	$376 \times 416 \times 380$	63 548 160
III	$130 \times 130 \times 475$	$470 \times 520 \times 475$	124 117 500
IV	$156 \times 156 \times 570$	$564 \times 614 \times 570$	214 475 040

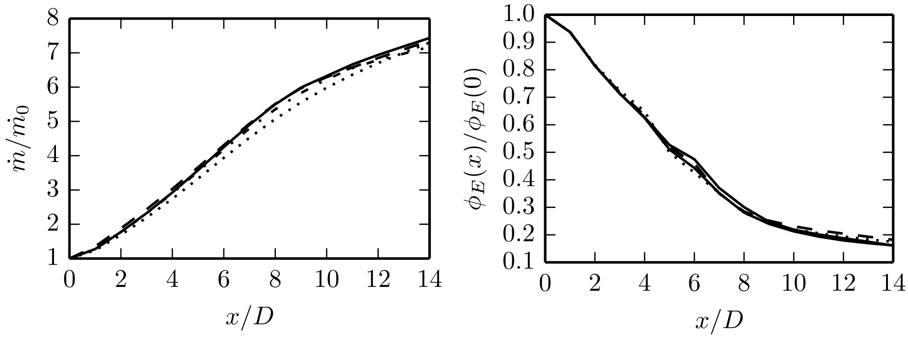

(a) entrainment

(b) kinetic energy flux

Figure 4.3: Grid sensitivity of planar data. (a) entrainment rate using vol. flux in Eq.4.4 (b) mean kinetic energy flux in Eq.4.5. (···) : Level I; (·—) : Level II; (—) : Level III (original resolution); (——): Level IV.

4.2 Flow dynamics

In the current section, we investigate the transitional flow dynamics of the different cases by looking at instantaneous vortex patterns in Section 4.2.1, and the mechanisms driving their evolution in Section 4.2.2.

4.2.1 Unsteady flow behavior

We present the dominant unsteady flow features playing a crucial role in the momentum and scalar transport. To this end, we vizualize isocontours of vorticity modulus $|\boldsymbol{\omega}|$ and isosurfaces of the Q criterion [60], where Q is the second invariant of the velocity gradient tensor, defined as

$$Q = \frac{1}{2}\left[\Omega_{ij}\Omega_{ij} - S_{ij}S_{ij}\right], \tag{4.6}$$

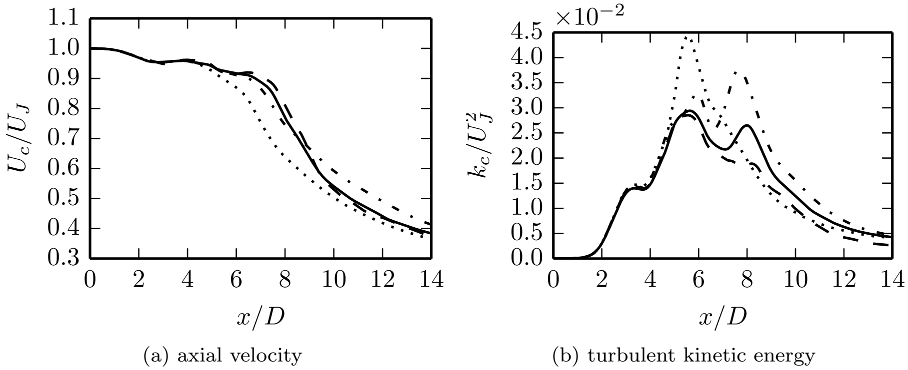

(a) axial velocity (b) turbulent kinetic energy

Figure 4.4: Grid sensitivity of examples of flow data along the centreline. (a) mean axial velocity: $U_c = \langle u_x \rangle_{r=0}$; (b) mean turbulent kinetic energy: $k_c = 0.5 \langle u_i' u_i' \rangle_{r=0}$. See Fig. 4.3 for captions.

with $\Omega_{ij} = [\partial u_i/\partial x_j - \partial u_j/\partial x_i]/2$ the skew-symmetric rate-of-rotation tensor and $S_{ij} = [\partial u_i/\partial x_j + \partial u_j/\partial x_i]/2$ the symmetric rate-of-strain tensor.

In Figure 4.5 isosurfaces of Q are illustrated. For the baseline case *B2* the single-helix mode is observed in the transition region. In contrast, actuation syncronizes the axisymmetric mode, and a train of strong vortex rings are shed with the actuation frequency. In addition to primary vortices, secondary counter-rotating vortex pairs are also present, located in the braid regions between successive vortex rings. Due to their prominent size and strength these primary and secondary structures are most noticable in Case *C1*.

Figure 4.6 presents streamwise snapshots of $|\boldsymbol{\omega}|$ in an actuation plane, i.e. a cutplane passing through the centreline of an actuator (plane given by $z = 0$ in this case, cf. Fig. 4.1). Jet actuation causes significant changes in these planes as seen in Figure 4.6c–f. We see again that in-phase actuation leads to strong formation of vortex rings with round cores that are synchronized to the actuation frequency. A fully grown ring is marked in Case *C1* (cf. red dashed line in Fig. 4.6d). The vortex ring is clearly asymmetric with lower (trough) part on the actuation side ($y > 0$) and higher (peak) part on the other off-actuation side. A three-dimensional view of this asymmetric ring is given in Figure 4.7. The ring has been distorted azimuthally and longitudinally and has a corrugated pattern. Similar vortex patterns are also seen in experiments with corrugated nozzles [78] or simulations with combined axial and azimuthal forcing [16].

Looking further at the actuation planes in Figure 4.6, we note the presence of

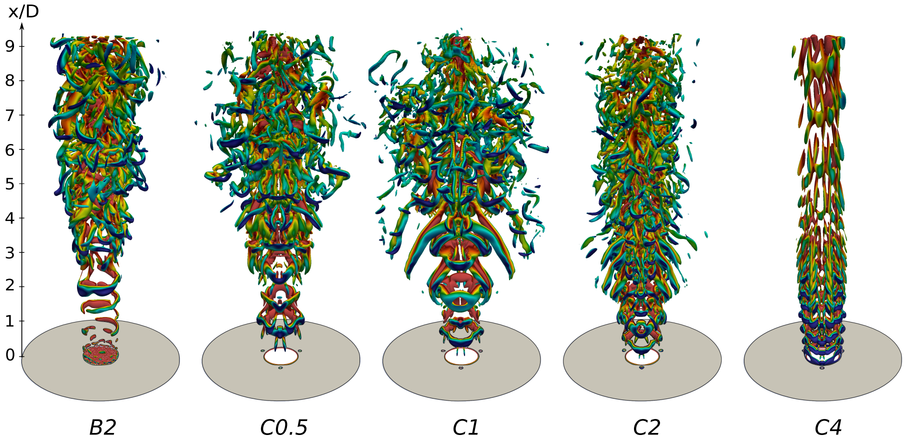

Figure 4.5: Visualization of vortical structures by isosurfaces of $Q/(U_J^2/D^2) = 3.267$ (0.3267 for *C4*). Color coded by velocity modulus (maximum value is $0.8U_J$ and coded in red).

streamwise vortex filaments in the braid regions. These secondary structures are first formed between the peak sides of primary rings, similar to earlier observations [82, 16]. An example is marked for Case *C1* between two fully formed vortex rings using the red solid line in Fig. 4.6d. Once these streamwise filaments appear, they free themselves from their trailing vortex rings and spread away from the jet core with large angles to jet axis (cf. blue arrow). We also observe the formation of streamwise filaments and their lateral ejections on the trough sides of the rings, starting from the downstream vortex ring (cf. green arrow).

We first further focus on Case *C1* in Figure 4.8b, presenting snapshots of $|\boldsymbol{\omega}|$ on various transverse planes at the same time instance as Fig. 4.6d. In general, the actuation causes a profound distortion on the jet cross-section and induces strong anisotropy. The $x/D = 2.3$ plane cuts the first developed vortex ring through the peaks (cf. I in zoom A on Figure 4.8b. The ring has intensive vorticity on peak sides (indicated with P, in zoom A). In addition, we see the formation of counter-rotating streamwise vortex pairs attached to peak sides (cf. II in zoom A). In the braid region, here at $x/D = 3$, these secondary structures grow stronger (cf. III in zoom B). Three initial side jets (cf. IV in zoom B for instance) are formed which are produced by the motions of counter-rotating streamwise filaments (cf. further discussion in Section 4.2.2). Further downstream ($x/D = 5$), the main corrugated vortex ring deforms and increases its three-dimensionality. New streamwise structures are induced at the

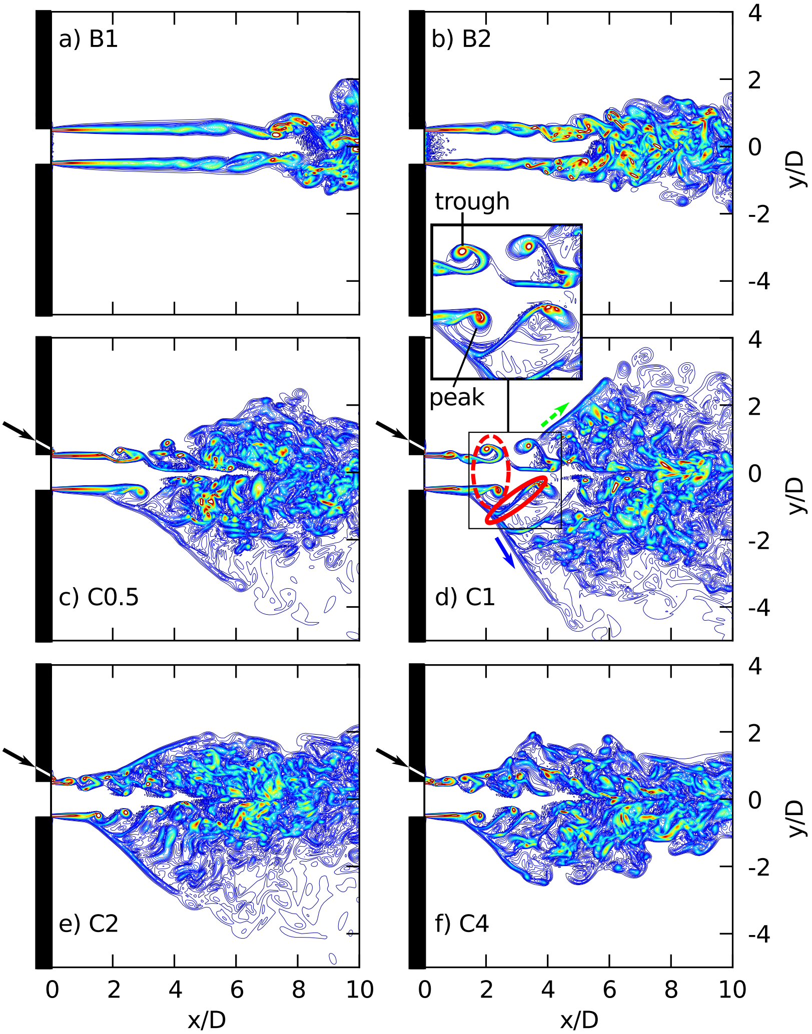

Figure 4.6: Snapshots of $|\boldsymbol{\omega}|$ on an actuation plane ($z = 0$).

trough sides. These new secondary structures produce additional side jets (cf. green arrows) and together with the initial ones (cf. blue arrows) they deform the system into a hexagram, which eventually ($x/D = 7, 10$) disintegrates into finer scales.

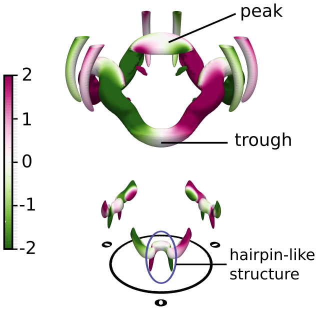

Figure 4.7: Initial jet development for *C1* by isosurfaces of $Q/(U_J^2/D^2) = 10.89$. Color coded by helicity density $H' = (\boldsymbol{\omega} \cdot \boldsymbol{u})/(U_J^2/D)$. Secondary vortex features have been removed for clarity of presentation.

We now return to the other actuation cases. For the cases with low frequency actuation, i.e. *C0.5* and *C1*, the vortex rings are well separated from each other and their interaction is limited (cf. Fig. 4.5). For Case *C2* we noted (not shown here) strong interaction and merging of vortical structures in the potential core. For the high frequency Case *C4*, vortices have substantially smaller size and strength and jet spreading appears to be suppressed.

To further elaborate these observations we present in Figure 4.9 power spectra of the streamwise component of fluctuating velocity signals at five downstream locations on the jet centerline ($r/D = 0$). For cases *C0.5* and *C1*, significant energy is contained at the actuation frequency until the most downstream measurement point ($x = 5D$). This is not the case for higher control frequencies. Already at $x = 1D$ the presence of subharmonics with increased energy content is clear. Further downstream these subharmonics gain more energy related to the vortex merging mechanisms observed in these cases. At $x = 5D$, spectral peaks are hardly noticable for cases *C2* and *C4* hinting at earlier breaking-up to small scales.

4.2.2 Vortex dynamics

In Section 4.2.1 it was observed that ZNMF controlled jets show distinct departure from axisymmetry. In this section, we investigate the mechanisms leading to the observed topological features.

ZNMF actuation produces isolated mini-vortex rings that are periodically travelling towards the main jet. These mini-vortex rings subsequently impact

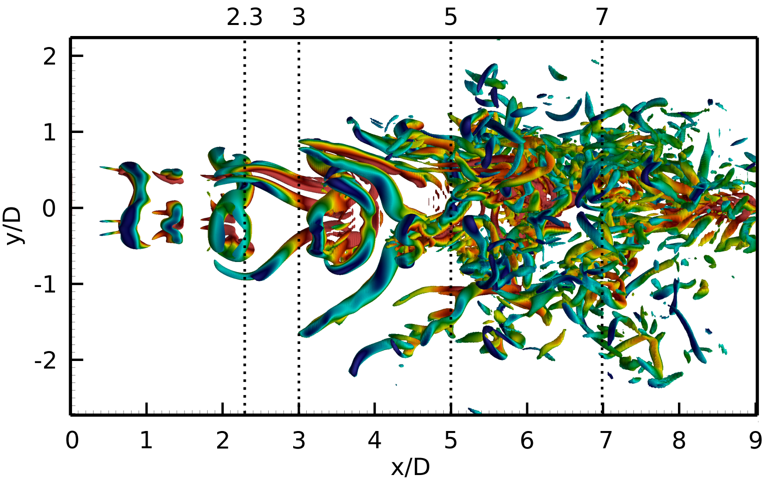

(a) Side view of Case *C1* from Fig. 6.

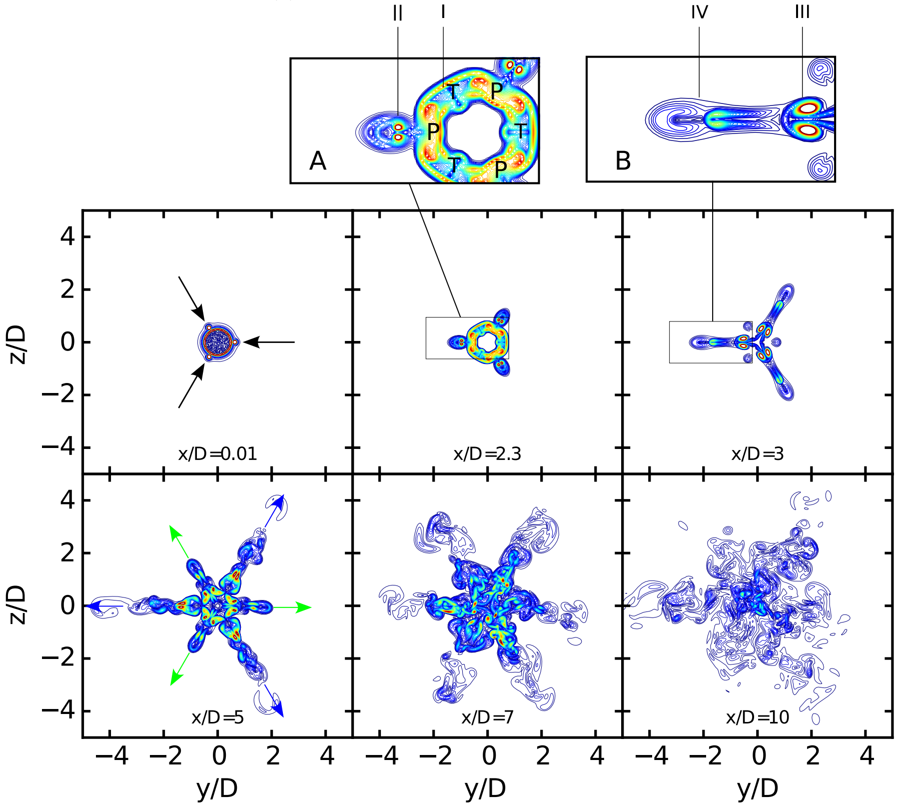

(b) Snapshots of $|\boldsymbol{\omega}|$ on transverse planes. Black arrows: actuation directions; blue arrows: side jets emaneted from peak sides of the vortex rings; green arrows: side jets ejected at trough sides.

Figure 4.8: Detailed vizualizations for Case *C1*.

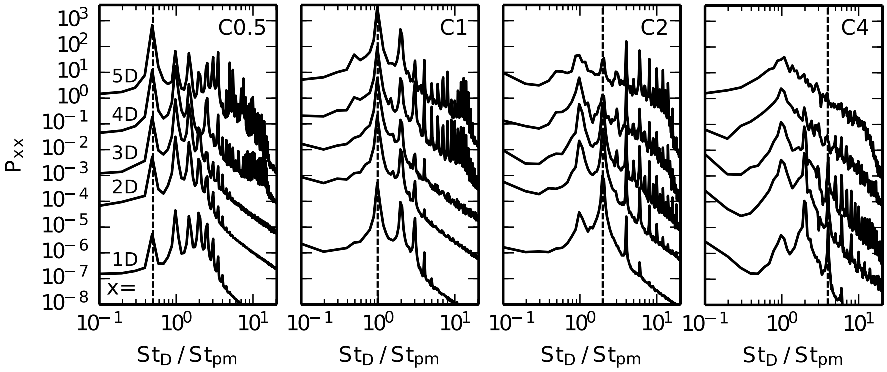

Figure 4.9: Power spectra of centreline velocity signals. Each spectrum is shifted one decade starting from the signals on $x/D = 5$. Dashed lines show actuation frequencies.

and distort the jet shear layer. Following this nonlinear interaction, the mini-vortex rings are stretched in streamwise direction by the main jet, and evolve into hairpin-like structures attached to small azimuthal vortex filaments that are the result of the local bending of the jet shear layer in these regions (cf. Fig. 4.7).

The actuation frequency plays a key role in the evolution of these initial vortex fragments. If the jet is excited with the natural mode, i.e. Case *C1*, then the time and spacing between two consecutive penetration events are long and hairpin-like structures disappear while azimuthal vortex filaments grow. They connect to the KH roll-ups on the unperturbed azimuthal sides, and build corrugated vortex rings. The further downstream development of the jet in this case is very similar to axisymmetric jets subject to periodic azimuthal perturbations [86, 16] where strong corrugated vortex rings also emerge and give rise to powerful secondary structures which produce side jets. These side jets remarkably alter the global characteristics of the jet.

In contrast, if the jet is actuated with a high frequency, as in Case *C4*, hairpin vortices interact with each other and inhibit azimuthal structure growth. This mechanism leads to suppression of large scale vortex development and reduces jet spreading. The vortex dynamics for these two distinct cases, i.e. Case *C1* and Case *C4* are now discussed in more detailed.

Case *C1*: Strong primary structures and side jets

The jet development for Case $C1$ is mainly dominated by downstream evolution of ZNMF induced azimuthal perturbations of the jet shear layer which gradually develop strong primary and secondary large scale vortices. Our discussion is based on vortex induction arguments, inspired by previous numerical studies on inviscid [86] and viscous [16] azimuthally perturbed jet flows in a temporal framework. We show that the downstream evolution of primary vortex structures is characterized by a sequence of self induction, mutual induction with secondary structures, followed by self induction again. The evolution of secondary counter-rotating streamwise structures is initially determined by mutual induction with the primary structures, followed by self induction. The latter leads to strong side jets that enhance jet spreading and lead to the above-discussed hexagrammoid structure.

To explain these features, we base our discussion on Figures 4.10, and 4.11. The first figure shows the primary and secondary vortices in side view, and shows streamwise vorticity in transverse jet sections at different downstream locations. For sake of discussion, three successive primary vortex rings, i.e. *VR1*, *VR2*, and *VR3*, are marked in the figure. Secondary structures, i.e., counter-rotating streamwise vortex pairs that are formed between the peak sides of the primary rings, are marked with *PP1*, *PP2*, *PP3* in the figure. The second figure, i.e. Figure 4.11, shows a detailed zoom on the initial dynamics of a primary vortex ring over the first actuation period $t \in [0, T]$ following its emergence. In order to better represent three-dimensional deformations of the vortex structures in both figures, the helicity density $H = \boldsymbol{\omega} \cdot \boldsymbol{u}$ is used to color Q isosurfaces (e.g. $H = 0$ for an azimuthally unperturbed vortex ring).

We now first turn to the discussion of primary vortex evolution. To that end, we look at Figure 4.11, and at the vortex regions in Figure 4.10c (i.e. see part ii, and iv). Note that the third sequence in Figure 4.11, i.e. at $t = 3T/4$ approximately corresponds to the location of the transverse section in part ii of Figure 4.10c. At time $t = 0$ in Figure 4.11 we show an initial wavy vortex ring with an azimuthal wavenumber $m = 3$, that just emerged from three azimuthal vortex segments indicated in Figure 4.7. The waviness of the ring grows due to self-induced velocities and further deforms the vortex ring at later stages, i.e. $t = T/4$ and $t = T/2$. After that, the effect of self-induction is inhibited, because of the interaction with secondary streamwise structures [50]. This is best seen in part ii of Figure 4.10c (cf. also the zoom A), showing that the strong streamwise vorticity created in the peak regions of the vortex ring is now coupled to an opposite pair of counter-rotating secondary vortex structures. Because of this mutual interaction between primary and secondary structures, the peaks and troughs in the primary vortex ring flattens, as seen by the

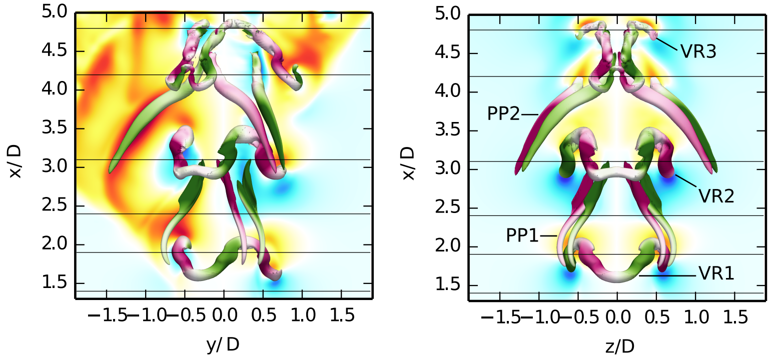

(a) z-view

(b) y-view

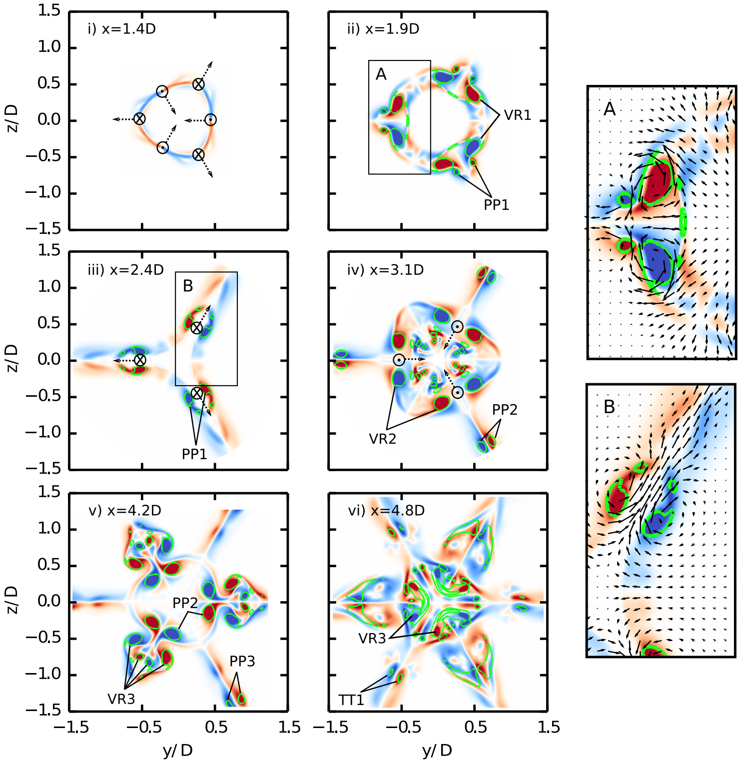

(c) x-views

Figure 4.10: Primary and secondary structures in potential core of *C1*. (a)-(b): Side views of 3D isosurfaces of $Q/(U_J^2/D^2) = 10.89$ color coded by normalized helicity density. Only three primary rings and corresponding secondary vortex filaments have been extracted. In (a,b) a streamwise section colored with radial velocity u_r is shown as background; i.e. in (a) the $z = 0$ plane, and in (b): $y = 0$ plane. (c): Transverse sections corresponding to horizontal lines in (a) and (b) visualizing snaphots of streamwise vorticity ω_r and (green) isolines of $Q/(U_J^2/D^2) = 10.89$.

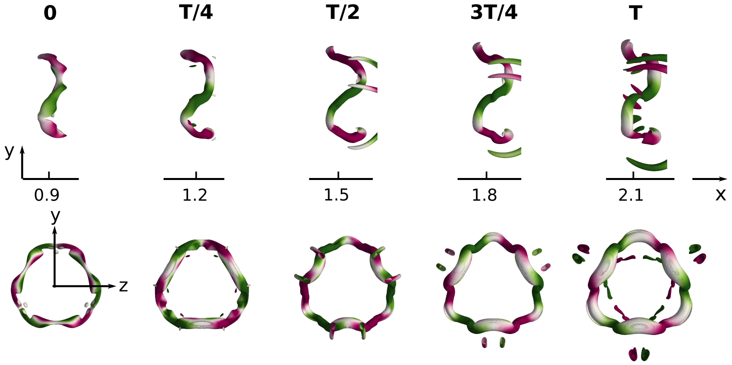

Figure 4.11: Temporal evolution of a vortex ring in *C1* by isosurfaces of $Q/(U_J^2/D^2) = 10.89$. Color coded by helicity density. T is one actuation cycle.

helicity coloring in Figure 4.11 for $t = 3T/4$ and $t = T$ and *VR1* in Fig. 4.10b. When continuing downstream to the next vortex ring *VR2*, we see that the secondary structures are detached from the primary vortex ring (reasons are further discussed below). As a result, self-induced velocities (indicated with arrows in part iv of Figure 4.10c) that result from the alternate arrangement of streamwise vorticity in the peak regions, push these peak regions towards the jet centerline. Consequently, the vortex ring rapidly deforms into a tripod-like three-dimensional structure with legs on the trough sides (cf. *VR3* in Fig. 4.10a-b and part v and vi of Fig. 4.10c).

The evolution of the secondary structures is now discussed. They originate from sheets of streamwise vorticity in the braid region, that are arranged with alternated signs (cf. part i of Figure 4.10c). This particular vorticity pattern is generated by the effect of global induction [86]: the radial shear layer of the main jet is azimuthally perturbed by the ZNMF actuation, and is convected faster in regions closer to the jet centerline, i.e. at the ZNMF penetration side. This results in streamwise vorticity with alternating signs as seen in Figure 4.10c (part i). This arrangement of streamwise vorticity leads to self-induction as also shown in Figure 4.10c (part i) with arrows. Moreover, similar to the creation of secondary vortex structures in mixing layers [83, 94], it is well documented [86] that the combination of this self-induction with the stretched strain-field in the braid region between the primary vortex peak sides, leads to the generation of secondary structures that are attached to the peak sides of the vortex rings (cf. *PP1* in Fig. 4.10c-part iii and 4.10a-b). Initially, mutual induction with the primary vortex ring is dominant in the evolution of secondary vortices, as they have an opposite arrangement of streamwise vorticity (cf. Fig. 4.10c-part

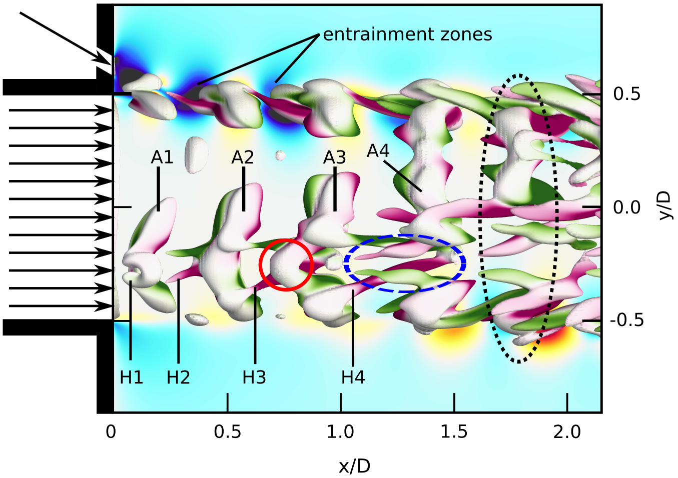

Figure 4.12: Initial jet development for *C4* by isosurfaces of $Q/(U_J^2/D^2) = 3.267$. Color coding is the same as in Figure 4.10(a,b).

ii). This difference is directly related to the different way in which streamwise vorticity is generated in the braid region (global induction), and the ring region (by ZNMF impact and self-induced velocities – cf. discussion above).

The secondary streamwise vortex pairs have very strong self-induction in their braid regions (indicated with arrows in Fig. 4.10c-part iii), which eventually overcomes the effect of mutual induction at their tips. Thus, they free themselves from the primary structures and spread in lateral direction (cf. *PP2* in Fig. 4.10a). As a result, the vortex pairs eject high velocity fluid from the jet core to the ambient and produce side jets (cf. zoom B in Fig. 4.10). At the same time, in the region between vortex pairs, quiescent ambient fluid is entrained into the potential core (cf. also zoom B in Fig. 4.10) [34].

Finally, when the primary structure evolves into a tripod-like geometry, self-induced velocities stretch the strain field around the sharp tips in the trough sections, and additional secondary vortex filaments develop (cf. *TT1* in Fig. 4.10c-part vi). The evolution of these newly emerged filaments is similar to the ones on the peak sides. Together with the secondary structures on the peak sides they shape the jet's transverse cross-section into a hexagram.

Case *C4*: Suppression of jet spreading

Now we turn to Case *C4* where hairpin-like structures induced by the synthetic jets play a more dominant role. When the actuation frequency is high, the streamwise spacing between ZNMF induced vortex filaments is low. This has a major impact on the downstream development of the flow as we will discuss in this section. The discussion will be limited to the region close to the orifice $(x < 2)$.

To facilitate the discussion, the initial development of Case *C4* is illustrated in Figure 4.12. The evolution of ZNMF induced mini-vortex rings into streamwise hairpin-like structures is indicated with the sequence *H1*–*H4* in the figure. It is observed that *H1* is a slightly distorted mini-vortex ring impacting the main jet that generates a small azimuthal vortex filament *A1*. The mini-vortex ring quickly evolves into a streamwise hairpin-like structure that has its head connected to the azimuthal filament, and convects downstream (cf. *A2*–*H2*). A similar structure is observed in Case *C1* (cf. Fig. 4.7). The difference in Case *C4* is that now the tails of the hairpin connect to the trailing filament *A1*, and remain more stable.

When looking in more detail at the hairpin vortices *H2* and *H3*, it is observed that they create strong regions of entrainment between their legs (cf. strong negative radial velocity on the other actuation side in Figure 4.12, i.e. at $y = 0.5$). As a side effect, the nearby azimuthal vortex filaments are pulled into these entrainment zones, and are strongly deformed (see red circle marking the interaction between *A3* and *H3*). Further downstream, the hairpin-like vortex *H4* largely converts the leading vortex filament *A4* into streamwise vorticity (cf. blue dashed region). This counter-balances the streamwise vorticity of the hairpin itself, inhibiting further entrainment. At this time, the shear layer rolls up at the unperturbed sides into new azimuthal filaments. We believe that this is the result of conventional KH instability. Finally, at the end of the investigated region (cf. region marked with black dotted line), we have small portions of azimuthal KH roll-ups at the unperturbed sides, and a street of streamwise vortices at the perturbed sides of the jets. Remind that in large contrast to this, a strong primary vortex ring has developed in Case *C1* at the same location $(x = 1.8D)$ (cf. $t = 3T/4$ in Fig. 4.11).

The lack of formation of strong coherent vortex rings suggests that large scale primary vortex formation is effectively inhibited by the ZNMF induced hairpin-like streamwise structures in the initial jet region $(x < 2D)$ in *C4*. This mechanism substantially delays the growth of conventional primary and secondary structures, suppressing the spreading of the jet (cf. Fig. 4.5 in Section 4.2.1). Similar results have been observed in jet control studies with

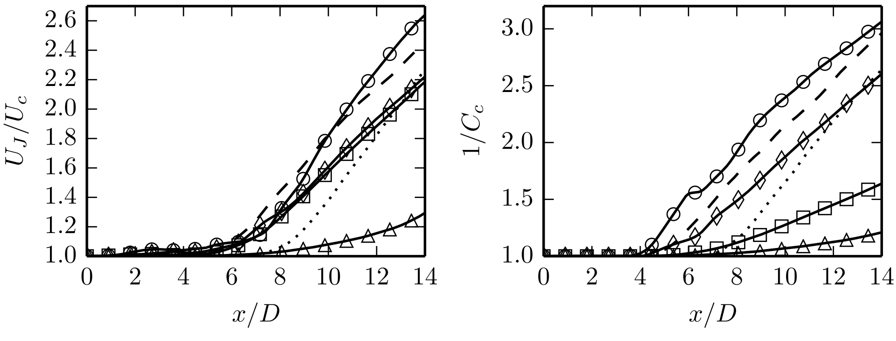

(a) velocity (b) passive scalar

Figure 4.13: Evolution of the streamwise velocity $U_c = \langle u_x \rangle_{r=0}$ and the passive scalar $C_c = \langle c \rangle_{r=0}$ along the jet centreline. $(\cdots)$: *B1*; (−−): *B2*; (—◇): *C0.5*; (—○): *C1*; (—□): *C2*; (—△): *C4*.

chevron nozzles [42] and steady mini-jets [4].

4.3 Mean flow characteristics

In the previous section, we saw that different actuation frequencies produce distinctive jet dynamics. Here, we further investigate global jet characteristics using statistical results. Focus is on the common parameters that are often used to describe mixing efficiency, and are either measured on the centerline of the jet (cf. Section 4.3.1), or over planes normal to the centerline (cf. Section 4.3.2). Next to that, we also present results of scalar transport tubes and flux lines in Section 4.3.3. For the discussion of results in the current section, it is important to recall that the baseline cases (*B1* and *B2*) have inlet perturbations that are an order of magnitude higher than that of the control cases (cf. Section 4.1.1), to trigger comparable transition lengths as for the controlled cases (at same levels of perturbations, the baseline cases would remain largely laminar).

4.3.1 Centreline statistics

First, averaged results along the jet centerline are presented. Figure 4.13a shows the evolution of the reciprocal of the streamwise velocities $U_c(x) = \langle u_1 \rangle_{r=0}(x)$ along the jet centerline. As may be expected, both baseline cases have a centerline velocity that is approximately constant in the potential core, then

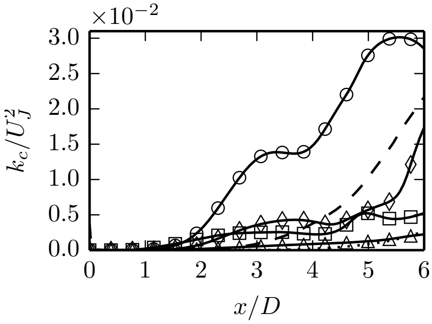

Figure 4.14: Evolution of the turbulent kinetic energy $k_c = 0.5 \langle u_i' u_i' \rangle_{r=0}$ along the jet centreline. See Fig.4.13 for captions.

followed by a linear increase of $1/U_c$. Case *B2* has a potential core of $x/D \approx 5$, whereas *B1* has a quite long potential core of $x/D \approx 8$.

Among the controlled cases, Case *C4* clearly illustrates the effect of inhibited jet spreading on the centerline velocity (cf. Figure 4.13a). The potential core is very long, and the subsequent decay rate of the centerline velocity is slow (small slope for $1/U_c$). The transition is a lot slower than that of the baseline cases, resulting from a combination of low jet spreading rate, and random perturbations on the inlet that are an order of magnitude lower (cf. Section 4.1.1). Further, the control cases *C0.5* and *C2* both have a potential core of approximately $x/D = 5$, followed by nearly identical decay rates, with slopes that are slightly smaller than those for the baseline cases. Finally, Case *C1* has the highest decay rate for centreline velocity, and a potential core with the same length as Case *C0.5* and *C2*.

In Figure 4.13b the development of the reciprocal of centreline scalar concentration $C_c = \langle c \rangle_{r=0}$ is shown for all cases. The evolution of C_c is very similar to U_c for Case *C0.5*, *C1* and the baseline cases. The only difference lays in the slightly higher C_c decay rates compared to U_c. The most noticeable distinction between C_c and U_c evolution is observed in Case *C2*. Here the decay of C_c is very slow in contrast to U_c. Also for Case *C4*, the decay of C_c is a bit slower than that of U_c.

Now we address how the fluctuating part of the velocity is influenced by the actuation in the potential core ($x < 6D$). As a quantitative appraisal for this we check the evolution of turbulent kinetic energy on the jet centreline $k_c = 0.5 \langle u_i' u_i' \rangle_{r=0}$. Figure 4.14 shows k_c normalized using the jet inlet velocity. Among the controlled cases the highest amplification for potential

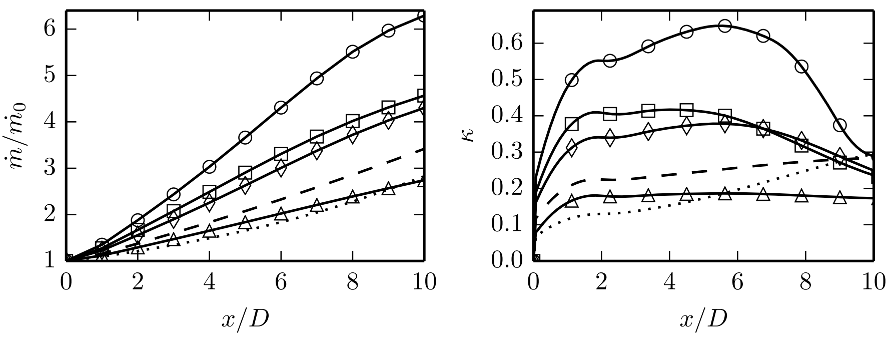

(a) entrainment (b) entrainment rate

Figure 4.15: The variation of entrainment and local entrainment rate with axial distance. See Fig. 4.13 for captions.

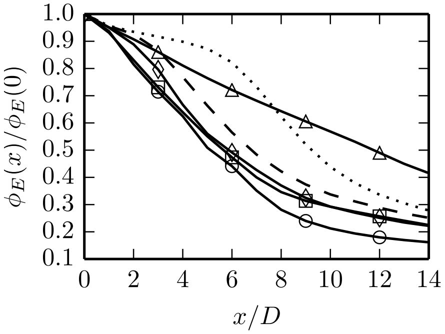

Figure 4.16: Flux of mean kinetic energy through transverse planes.

core fluctuations is obtained for Case *C1*. After around $x/D = 2$, Case *C1* shows a rapid increase in k_c, reaching a first peak value of $k_c/U_J^2 \approx 0.03$ at $x/D \approx 5.2$. Case *C4* exhibits a very slow streamwise development of the turbulent kinetic energy, suggesting the efficiency of high frequency actuation to suppress turbulence transition. Among the baseline cases, the *B2* case has a higher turbulent kinetic energy between $4D < x < 6D$ compared to all controlled cases except *C1*. For Case *B1* the rate of kinetic energy production is comparable to the Case *C4*.

4.3.2 Planar statistics

We further address statistics of fluxes through transverse planes, to investigate the global behaviour of the jet evolution. First of all, in Figure 4.15a the results for jet entrainment of the ambient fluid defined by Eq. (4.4) are shown. We observe that the entrainment is enhanced significantly by actuated cases *C0.5*, *C1* and *C2*. This is mainly due to formation of strong primary vortices and secondary structures which produce side jets. These are known to significantly improve entrainment rates of the jets (cf. discussion in Section 4.2.2). We observe that actuation of the preferred mode (Case *C1*) delivers the most entrainment to the jet core. This is mainly due to strongest side jet formation for this case. Moreover, we note that high frequency actuation, i.e. Case *C4*, induces a major reduction in entrainment as the growth of large scale structures responsible for entrainment is minimal in this case.

The striking entrainment abilities of controlled jets *C0.5*, *C1* and *C2* can also be seen in their local entrainment rates, defined in Ref. [93] as $\kappa = (D/\dot{m}_0)\mathrm{d}\dot{m}/\mathrm{d}x$ presented in Figure 4.15b. Close to the jet origin, the controlled cases (except Case *C4*) exhibit an entrainment rate that grows remarkably faster than the baseline cases. Subsequently ($2 < x/D \approx< 6$) entrainment rates first stagnate for Cases *C0.5*, *C1* and *C2* and then decrease, dropping back to the levels of the baseline cases.

In Figure 4.16 the flux of mean kinetic energy (Eq. 4.5) along the jet is shown. We see that the initial energy flux decays for all cases. This decrease can be attributed to an increase in the production of turbulent kinetic energy while moving downstream. The highest decay is observed in Case *C1*, showing that this control case is the most efficient in converting mean-flow energy into turbulence.

To further quantify mixing, contours of the mean passive scalar c are shown in a number of transverse planes in Figure 4.17. Here we see again that initially (around $x/D = 2.5$) the synthetic jets deform the jet column cross-section into triangular-shaped contours. A little bit further downstream $x/D = 5$ we observe the effect of side jets on the transported passive scalar and non-uniform hexagrammoid shapes in the contours are observed. Further downstream the sharp regions of hexagrams entrain fluid and spread, morphing back into triangular-like patterns on the most downstream plots. In order to further visualize the transport of the passive scalar for the different cases, we study the evolution of transport tubes and scalar flux lines next.

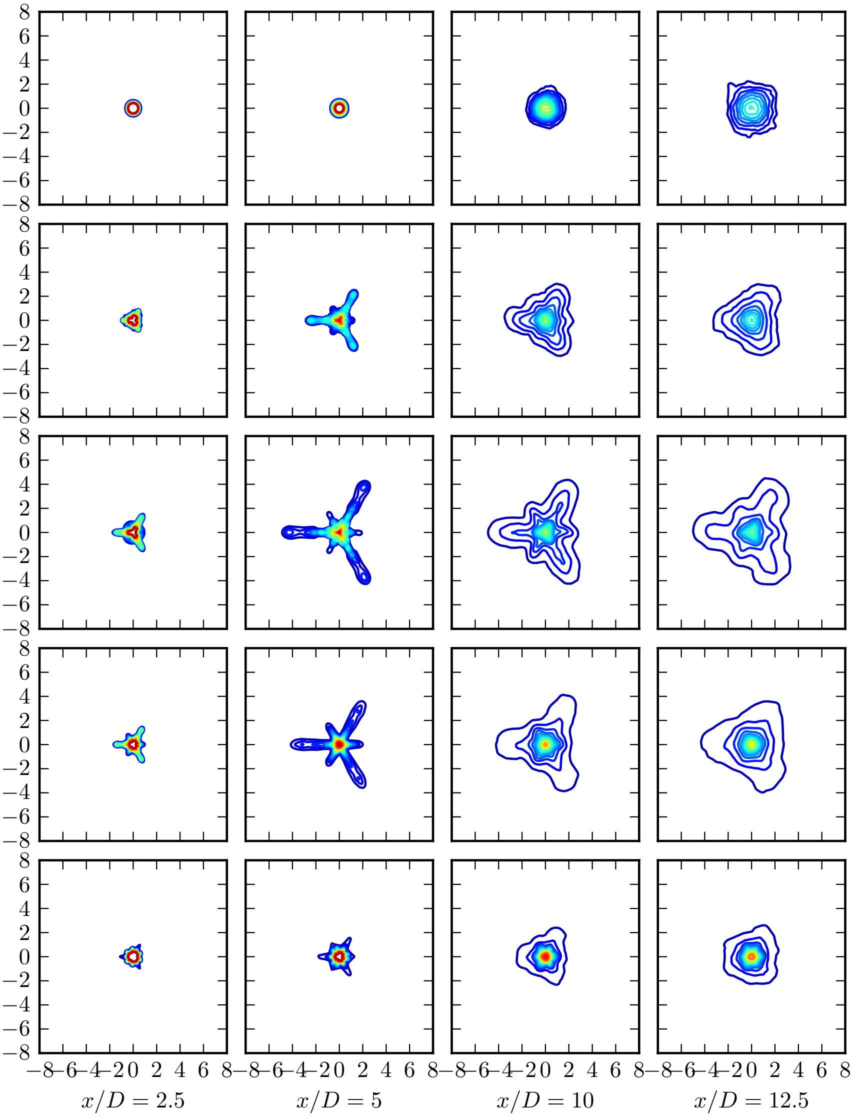

Figure 4.17: Contours of mean scalar concentration $\langle c \rangle$ on various transverse planes $x = 2.5D, 5D, 10D, 12.5D$. Contour levels of 0.05 varying between $\langle c \rangle = 0$ and $\langle c \rangle = 1$.

4.3.3 Scalar transport tubes

In the current section, the mixing of the passive scalar is further investigated using scalar transport tubes that are constructed based on flux lines of the scalar transport field. These flux lines are essentially equivalent to the heatlines proposed by Kimura and Bejan [74], and the related tubes are similar to the concept of momentum and energy transport tubes discussed by Meyers & Meneveau [87]. Here we briefly review these concepts in terms of scalar fluxes, and then apply them to the different jet cases.

First of all, recall that a classical streamline in a stationary mean incompressible flow field is a curve that is constructed tangentially to the mean velocity vector $\langle \boldsymbol{u} \rangle$ of the flow. A classical streamtube is constructed by taking the family of all streamlines passing through a closed curve in the three-dimensional fluid domain [9]. Obviously, by construction, there is no mass transport through the tube mantle M as $\langle u_i \rangle n_i = 0$ (with n_i the normal vector to the tube mantle). This concept can be extended to passive scalar transport (and other properties) [74, 87] by considering the vector field for the Reynolds-averaged total flux of the scalar quantity, i.e.

$$F_{c,i} = \langle u_i \rangle \langle c \rangle + \langle u_i' c' \rangle - \frac{1}{\mathrm{Re}_D Sc} \frac{\partial \langle c \rangle}{\partial x_i}. \tag{4.7}$$

Using this flux vector, the Reynolds-averaged scalar-transport equation in a stationary system simplifies to

$$\frac{\partial}{\partial x_i} F_{c,i} = S, \tag{4.8}$$

where S are potential volume sources of the scalar quantity (here $S = 0$). Thus, if we construct a scalar transport tube based on flux lines along the flux vector field $F_{c,i}$ (and with mantle M, two cross-section A_1 and A_2, and volume Ω), then integration of Eq. (4.8) over the tube volume and using the Gauss theorem yields

$$\iint_{A_1} F_{c,i} n_i \mathrm{d}\boldsymbol{x} + \iint_{\mathrm{A_2}} \mathrm{F_{c,i} n_i d}\boldsymbol{x} = \iiint_{\Omega} \mathrm{S d}\boldsymbol{x}, \tag{4.9}$$

since by construction there are no fluxes over the tube mantle M. Consequently, the constructed tube is a scalar transport tube: i.e., the only changes to the scalar in Ω are due to internal sources S. In absence of sources (as is the case in the current work), the scalar flux is conserved along the tube.

In the current section, we use this concept to investigate how the scalar at the jet inlet is transported on average throughout the domain for the different control cases. To that end, a series of concentric circles is selected as starting

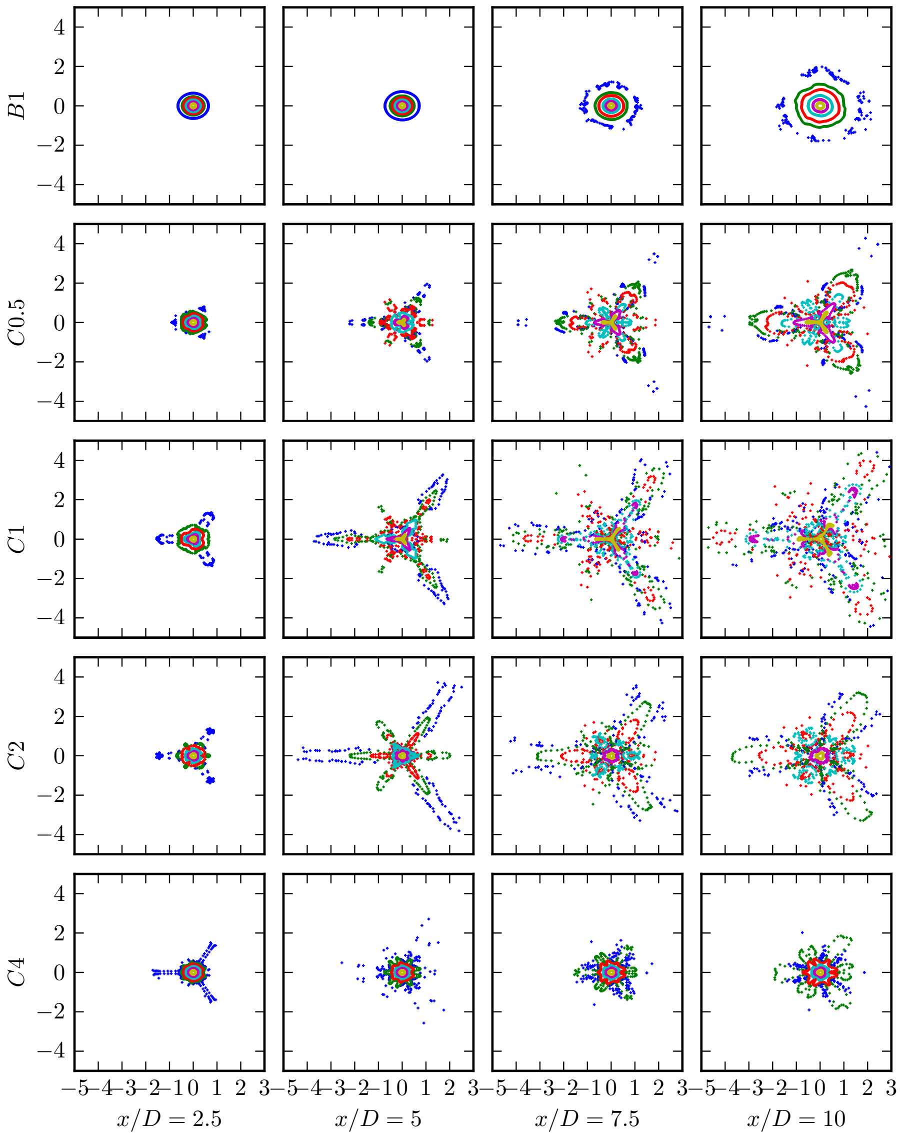

Figure 4.18: Transverse sectional views of flux lines starting from concentric circles on the inlet $x = 0$ with radial distances of $2r/D = 0.2$ (yellow),0.4 (magenta),0.6 (cyan),0.8 (red), 0.9 (green),0.99 (blue). Each circle is seeded with 180 points.

point for six different transport tubes. Each circle is seeded with 180 points through which flux lines are constructed. In Figure 4.18 results are presented for the different cases, and the intersection of the different flux lines with planes at $x/D = 2.5$, 5, 7.5, and 10 are shown as points, colored according to the radius of the seed circle from which they originate.

Looking first at the baseline case B1 in Figure 4.18, we observe that the circular shape of the flux tubes is well conserved downstream – this is quite normal since this case is fully axisymmetric. For the tube starting from the largest circle (colored in blue), we observe that the circular shape is not fully retained for $x/D = 7.5$, and 10, and points are a bit more scattered. This is related to statistical averaging times that are not long enough for this property at these downstream locations: recall that for a round jet, the turbulent time scale is proportional to x^2, so that statistical averages converge considerably slower at large downstream distances.

For the controlled cases in Figure 4.18, the triangular and hexagonal geometries discussed in previous sections, are recognized again. However there are some distinct differences between Case *C0.5*, Case *C4* (and to a lesser extent Case *C2*) on the one hand, and Case *C1* on the other hand. For the former cases, it is still possible to assemble to the flux tubes at downstream planes (i.e. their intersection with the plane) by connecting points belonging to the same-colored set of flux lines intersects (something we didn't do on the figure). For Case *C1* we find that this becomes very difficult, i.e. for the planes $x/D = 7.5$, and 10, the distribution of the flux points has become so irregular that it is impossible to reasonably connect the points and reconstruct the shape of the tube mantle. This may hint at some useful analogies with chaotic mixing for laminar-flow systems [5, 98], and further substantiates that Case *C1* is more efficient in large-scale mixing than the other cases.

4.4 Concluding remarks

In this chapter, we numerically studied a moderate Reynolds number ($\mathrm{Re}_D = 2000$) axisymmetric jet subject to multiple miniature ZNMF actuators. The parameters in the study were four different actuation frequencies varying between $\mathrm{St}_D = 0.165 - 1.32$. We employed three actuators distributed evenly in circumferential direction and directed towards the main jet with an inclination angle of $\alpha = 30$ to the jet axis. The momentum coefficient of individual actuators is selected to be $C_\mu = 0.0049$. The actuation was implemented as a sinusoidal signal and all the actuators were driven in phase.

All the controlled cases show highly distorted instantaneous shapes and structures, showing the capability of multiple ZNMF actuation in modifying the base jet flow. We clearly observe that the resulting vortices are significantly different from a regular axisymmetric jet. Although the driving momentum coefficient is rather small, the influence on the development of the large coherent structures is significant. The effects are maximal in the case where the actuation is closest to the jet preferred frequency, i.e. Case *C1* with $\mathrm{St}_D = 0.33$. In contrast, the evolution of large coherent structures is suppressed by the highest investigated actuation frequency, i.e. Case *C4* with $\mathrm{St}_D = 1.32$.

We find that actuation with the preferred mode frequency leads to strong “side jets” that significantly increase the spreading of the jet, and change the geometry of the transverse jet section into hexagrammoid patterns. The mechanisms creating this phenomenon were analyzed, and following scenario was found. First, ZNMF actuation induces azimuthal perturbations on the initial jet profile by penetrating into the jet. As a result, the jet shear layer evolves into strong corrugated vortex rings with peaks at the unperturbed azimuthal locations. These primary structures are shed with the actuation frequency, and are prone to self-deformation. The strain field in the braid regions between the peaks of successive vortex rings are heaviliy stretched, and as a result, counter-rotating streamwise vortex pairs are formed. As a result of strong self-induction, these secondary structures spread laterally with large angles to the jet axis. This self-induction leads to the production of side jets. These observations are similar to earlier numerical [16] and experimental [34] studies on azimuthally perturbed jets.

We further find that actuation with high frequency, i.e. *C4* with $\mathrm{St}_D = 1.32$, prevents the above scenario. In this case, ZNMF actuation induces streamwise hairpin-like vortices that play an important role. They break up the azimuthal vortex filaments, and prevent the formation of strong corrugated vortex rings. As a result, jet spreading and mixing are suppressed.

Key characteristics of the jet such as mean entrainment rate, decay rate and fluctuating energy are also strongly altered following the modifications in the instantaneous motion. First, we observed that the entrainment in the near field is significantly increased when the driving frequency of the controls are close to the natural jet frequencies thanks to the strong side jet production. Similar augmentations have also been observed in other metrics such as centreline decay rate and mean turbulent kinetic energy production. Moreover, we observed that passive scalar transport is enhanced as well by analysing the corresponding transport tubes. The effects on global jet characteristics were completely opposite in the high frequency actuation Case *C4*. In this case, all the characteristic metrics had much lower values and remained even below the reference baseline cases.

Chapter 5

Optimization with the continuous adjoint method

This section is devoted to the description of the optimal control of jet flows with the continuous adjoint method. In a typical optimal flow control problem, an objective for the control study [52] is set first. Common control objectives of interest vary from drag minimization [11], transition delay [67], noise reduction [116], to enhanced power extraction [46]. Subsequently, the control objective is mathematically formulated using a cost functional quantifying the desired flow behaviour. Afterwards, a set of controls are designed to manipulate the flow and meet the control objective. If these controls are located on the solid boundaries of the domain, then we obtain a *boundary control* problem. Examples are synthetic jets, steady blow or suction, plasma controls, etc. If the controls are placed in the fluid domain itself, e.g. using magnetic fields or heat sources, then we obtain a *distributed control* problem. Having postulated the cost functional and controls, an optimization problem is formulated subsequently with a set of Navier–Stokes PDE constraints as state equations.

There are two approaches to solve a PDE-constrained optimization problem and minimize the cost functional [105]. In the first approach, optimality conditions are first formally derived in the continuous setting, and a set of differential equations are obtained. Subsequently, these nonlinear infinite-dimensional equations are discretized and solved in an iterative way, usually with a gradient-based minimizer. This first method is referred to as the *optimize-then-discretize* approach. In the second approach, referred to as *discretize-then-optimize*, one first casts the optimization problem into the finite-dimensional form by discretizing the cost functional and corresponding PDE constraints.

Subsequently, the optimality conditions are derived and solved for the finite-dimensional problem. In general, both approaches deliver different results, see e.g. [43] for a discussion, though in the limit of very fine grids, they converge to the same solution.

Gradient–based methods are commonly employed in optimal flow control studies because of their reasonable convergence and low storage requirements [11]. There are two ways to calculate the gradient of the cost functional with respect to controls: the direct or finite-difference method, and the adjoint method. In the direct method, one straightforwardly perturbs the state equations for every control direction and evaluates the cost functional. A finite–difference formula is applied afterwards to calculate the gradient. If central-differencing is used, the procedure requires $2N+1$ cost functional evaluations, where N is the dimension of the discretized controls. This is extremely expensive and therefore infeasible for turbulent flow cases where cost functionals are evaluated with DNS or LES, and where $1 \ll N$. In contrary, the adjoint method only requires the solution of the adjoint Navier–Stokes equations to provide the gradient information. The cost of the gradient calculation is not dependent on the dimension of the control parameter space. As the solution of the adjoint Navier–Stokes equations have comparable computational cost to the solution of the original DNS or LES, the adjoint method is clearly more attractive. However, the method requires the storage of three-dimensional velocity fields in every time step, and therefore becomes infeasible for long optimization horizons. Furthermore, there are some additional limitations when the method is applied to turbulent flows, cf. Section 5.3 for a discussion.

In this chapter, optimal jet flow control with the continuous adjoint method is described. To this end, the problem is mathematically formulated and its numerical discretization is discussed. The continuous adjoint method is selected mainly because of implementation reasons. This approach allows maximum code re-usability, and it is often the method of choice in optimal flow control studies with DNS and LES, e.g. [11, 116, 33, 70, 32]. The objective of the study is promoting kinematical mechanisms which can lead to enhanced jet mixing. The content of this chapter is limited to the problem description only. The application of the method using OpenFOAM® is performed in Chapter 6.

5.1 Jet flow optimization

In this section, the first step of optimize-then-discretize approach is described, i.e., a jet flow maximization problem is formulated in a continuous setting and then a gradient-based method is introduced to solve this problem.

5.1.1 Cost functional and controls

The first objective of this section is to select a flow characteristic that provides a good measure for the mixing behaviour in the flow. The mixing itself is not explicitly tackled, as it is a very difficult phenomena to quantify with a simple cost functional measured over a limited time horizon. In order to have a complete view about the mixing properties of the flow, detailed statistical information such as first, second order moments and probability density functions have to be provided [112]. These statistical data can be gathered by averaging over long time series. Such an operation is not possible with the adjoint method considering its excessive storage requirement bottleneck. Therefore, targeting a kinematical flow property instead of a statistical mixing measure is the only feasible choice at the moment.

The enstrophy, integrated in a region Ω_s over a time window $(0, T]$, is selected as the cost functional for the current optimization study. The mathematical formulation reads as follows

$$\mathcal{J}_\varepsilon(\boldsymbol{u}) = \frac{1}{2}\int\int_{\overline{\Omega}_s} \omega_i\omega_i \mathrm{d}\boldsymbol{x}\mathrm{dt}, \tag{5.1}$$

where $\overline{\Omega}_s := \Omega_s \times (0, T]$ is the observation or sensor domain, and $\boldsymbol{\omega} := \nabla \times \boldsymbol{u}$ is the vorticity field. $\mathcal{J}_\varepsilon(\boldsymbol{u})$ can be linked to the total dissipated kinetic energy $\mathcal{E}$ in Ω_s at time $t = T$, such that

$$\mathcal{E}(T) := -\frac{1}{2}\left[\int_{\Omega_s} u_i u_i \mathrm{d}\boldsymbol{x}\right]\Bigg|_0^T = 2\nu\mathcal{J}_\varepsilon(\boldsymbol{u}). \tag{5.2}$$

The dissipation is mainly associated with the strain [112], and the strain is esentially responsible for the streching and folding of material elements which drives the mixing [98]. Therefore, $\mathcal{J}_\varepsilon(\boldsymbol{u})$ can be related to mixing efficiency in the flow. Moreover, Delport et al. [33] demonstrated for a convective mixing layer that maximizing the dissipation $\mathcal{E}(T)$ accelerates the transition into smaller scales. It is well appreciated that earlier break-up into small scales is beneficial for molecular mixing.

Now controls have to be chosen. Obviously, using multiple ZNMF actuators, modelled as velocity boundary conditions as in Chapter 4, and optimizing for their signals is the most natural choice in the context of this dissertation. However, such a boundary control design can be numerically very challenging to optimize. As mentioned before, the gradient of the cost functional is calculated using the adjoint variables. For a boundary control problem, this gradient reads as follows

$$\nabla\tilde{\mathcal{J}}(\boldsymbol{\phi})_i = \frac{1}{\mathrm{Re}_D}\frac{\partial\xi_i}{\partial x_j}n_j - qn_i, \qquad \text{on } \partial\Omega_c, \tag{5.3}$$

$\partial\Omega_c$ is the control boundary, $\boldsymbol{\phi}$ is the control field, $\boldsymbol{\xi}$ is the adjoint velocity field and q is the adjoint pressure field. The reader is referred to [25] for a derivation. The first term requires the gradient of the adjoint velocity on the control wall. This gradient can be extremely steep if the controls are placed into the areas where the flow is most sensitive, e.g. close to shear layer in the case of round jets (cf. Fig. 5.3). Therefore, the calculation of this term is error-prone unless an extremely high grid resolution is applied in the vicinity of the wall. Moreover, such a refinement can impose infeasible restrictions on the time step. Furthermore, the second term requires the adjoint pressure on the wall. As discussed in Chapter 2, segregated solvers such as the projection method employs an unphysical Neumann boundary condition for the pressure, cf. Eq. (2.34). This unphysical boundary condition yields spurious boundary layers in the pressure. As the projection scheme is also used for computation of the adjoint Navier-Stokes equations, the calculated pressure on the control boundary is not reliable. To overcome this problem, one must use a coupled solver which is not available in OpenFOAM® and requires a very time-consuming reimplementation in the low level data structures of the code.

Due to the difficulties related to the computation of the adjoint velocity gradient and pressure on the control wall, optimal boundary control is not considered in this dissertation. In Chapter 4 we saw that strong large scale vortex development is triggered by azimuthal perturbations caused by synthetic jets. Therefore, we have made a further simplification in the modelling of the ZNMF actuators and modelled these actuators as localized forcing regions that are distributed around the jet circumference, and are capable of introducing azimuthal perturbations. Similar adjoint-based jet control using distributed control was previously employed in noise reduction of round jets [70] and plane jets [85]. However, these studies employed local heat source regions in the domain.

5.1.2 Problem formulation

In this section, the optimal distributed jet control problem using the enstrophy integral $\mathcal{J}_\varepsilon(\boldsymbol{u})$ in Eq. (5.1) as cost functional is mathematically formulated. A descriptive sketch for the problem is illustrated in Figure 5.1. No explicit constraints are applied to the controls. In order to bound the controls a penalization is applied. Gunzburger suggests that computational boundaries, e.g. outflow Γ_o and lateral Γ_r, boundaries, should not be included in the derivation of continuous optimality conditions [52]. These boundary conditions are non-physical, and therefore they are not considered as the part of the continuous problem. Thus, we consider that the jet is ejected into an infinite domain that is bounded by Dirichlet boundaries $\partial\Omega := \Gamma_i \cup \Gamma_w \cup \Gamma_\infty$. Consequently, the

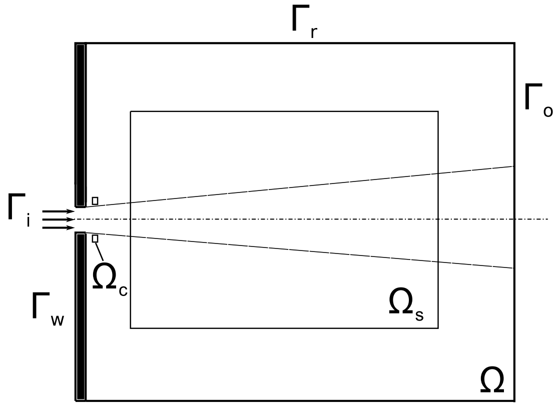

Figure 5.1: A schematic description for the jet optimization problem.

enstrophy maximization problem reads as follows

$$\min_{\boldsymbol{u},\boldsymbol{\phi}} \mathcal{J}(\boldsymbol{u},\boldsymbol{\phi}) := -\frac{1}{2}\int\int_{\overline{\Omega}_s} \omega_i\omega_i \mathrm{d}\boldsymbol{x}\mathrm{d}t + \frac{\gamma}{2}\int\int_{\overline{\Omega}_\mathrm{c}} \phi_\mathrm{i}\phi_\mathrm{i}\mathrm{d}\boldsymbol{x}\mathrm{d}t \tag{5.4}$$

s.t.

$$\frac{\partial u_i}{\partial t} + \frac{\partial u_j u_i}{\partial x_j} + \frac{\partial p}{\partial x_i} - \frac{1}{\mathrm{Re}_D}\frac{\partial^2 u_i}{\partial x_j \partial x_j} = f_i \quad \text{in } \overline{\Omega}, \tag{5.5}$$

$$\frac{\partial u_i}{\partial x_i} = 0 \quad \text{in } \overline{\Omega}, \tag{5.6}$$

$$f_i = \begin{cases} \phi_i & \text{in } \overline{\Omega}_c \\ 0 & \text{in } \overline{\Omega} \setminus \overline{\Omega}_c \end{cases}, \tag{5.7}$$

$$u_i = g_i \quad \text{on } \overline{\partial\Omega}, \tag{5.8}$$

$$u_i(0) = u_i^0 \quad \text{in } \Omega, \tag{5.9}$$

where $\overline{\Omega} := \Omega \times (0,T]$ is the flow domain, $\overline{\Omega}_c := \Omega_c \times (0,T]$ is the control domain, ϕ is the control field localized in Ω_c, $\boldsymbol{u}$ is the velocity field, p is the pressure field and γ is a penalization parameter.

The objective of the optimization problem in Eqs. (5.4)-(5.9) is to find $\overline{\boldsymbol{u}}$ and $\overline{\boldsymbol{\phi}}$ such that

$$\mathcal{J}(\overline{\boldsymbol{u}},\overline{\boldsymbol{\phi}}) < \mathcal{J}(\boldsymbol{u},\boldsymbol{\phi}) \;\; \forall \boldsymbol{u} \in \mathcal{H}_u, \boldsymbol{\phi} \in \mathcal{H}_c \tag{5.10}$$

where $\mathcal{H}_u$ and $\mathcal{H}_c$ are appropriate Hilbert spaces.

5.1.3 Optimality conditions

In order to derive the optimality conditions and find the set of equations that $\overline{\boldsymbol{u}}$ and $\overline{\boldsymbol{\phi}}$ should satisfy, the optimization problem in Eqs. (5.4)-(5.9) is first cast into an equivalent unconstrained reduced formulation

$$\min_{\boldsymbol{\phi}} \tilde{\mathcal{J}}(\boldsymbol{\phi}) := -\frac{1}{2}\int\int_{\Omega_s} \omega_i(\boldsymbol{\phi})\omega_i(\boldsymbol{\phi})\mathrm{d}\boldsymbol{x}\mathrm{dt} + \frac{\gamma}{2}\int\int_{\Omega_\mathrm{c}} \phi_\mathrm{i}\phi_\mathrm{i}\mathrm{d}\boldsymbol{x}\mathrm{dt} \tag{5.11}$$

with the reduced cost functional $\tilde{\mathcal{J}} : \mathcal{H}_c \to \mathbb{R}$. Subsequently, the reduced cost functional is assumed to be differentiable and its gradient $\nabla\tilde{\mathcal{J}}$ is defined. If $\mathcal{H}_c$ is endowed with the scalar product

$$(\boldsymbol{a}, \boldsymbol{b})_{\mathcal{H}_c} = \int\int_{\Omega_c} a_i b_i \mathrm{d}\boldsymbol{x}\mathrm{dt}, \tag{5.12}$$

then the gradient of the reduced cost functional is defined as the Riesz-representation of the derivative $\tilde{\mathcal{J}}'$ [15], i.e.,

$$\left(\nabla\tilde{\mathcal{J}}, \boldsymbol{\phi}'\right)_{\mathcal{H}_c} = \tilde{\mathcal{J}}'(\boldsymbol{\phi}') \quad \forall \boldsymbol{\phi}' \in \mathcal{H}_c,$$

where $\tilde{\mathcal{J}}'(\boldsymbol{\phi}')$ is the Gateaux derivative in the direction $\boldsymbol{\phi}'$ given by

$$\tilde{\mathcal{J}}'(\boldsymbol{\phi}') := \left.\frac{\mathrm{d}}{\mathrm{d}\alpha}\right|_{\alpha=0} \tilde{\mathcal{J}}(\boldsymbol{\phi} + \alpha\boldsymbol{\phi}') \quad \forall \boldsymbol{\phi}' \in \mathcal{H}_c. \tag{5.13}$$

Having defined the gradient of the reduced cost functional, the optimality condition can be described. The necessary condition of first order optimality states that an optimal solution $\overline{\boldsymbol{\phi}}$ renders a stationary point such that [15]

$$\nabla\tilde{\mathcal{J}}(\overline{\boldsymbol{\phi}}) = 0. \tag{5.14}$$

A computational expression can be derived by applying the chain rule to the derivative of the implicit variable $\boldsymbol{u}(\boldsymbol{\phi})$, and then deriving the corresponding adjoint operators. As the final expression contains adjoint states, the adjoint equations have to be derived subsequently [15].

A popular alternative to derive optimality conditions is the formal Lagrange method [111]. In this method, a Lagrangian functional is introduced to the PDE constrained optimization problem, and the optimality conditions are found from the vanishing directional derivatives of the Lagrangian. In the course of the derivation, all the integrals are formally defined and one would not care if they make sense in a functional analytic setting [111]. Thus, this approach is more attractive for complicated problems and it is commonly employed in the flow optimization studies, e.g. [25, 46, 97]. It is also the method of choice in this section to derive optimality system of equations.

For the derivation of the formal Lagrange method, we associate the following Lagrangian to the optimization problem in Eqs. (5.4)-(5.9)

$$\begin{aligned}\mathcal{L}(\boldsymbol{u}, p, \boldsymbol{\phi}, \boldsymbol{\xi}, q) &= \mathcal{J}(\boldsymbol{u}, \boldsymbol{\phi}) \\ &+ \int\int_{\Omega} \left(\frac{\partial u_i}{\partial t} + \frac{\partial u_j u_i}{\partial x_j} + \frac{\partial p}{\partial x_i} - \frac{1}{\mathrm{Re}_D} \frac{\partial^2 u_i}{\partial x_j \partial x_j} - f_i \right) \xi_i \mathrm{d}\boldsymbol{x}\mathrm{dt} \\ &+ \int\int_{\Omega} q \frac{\partial u_i}{\partial x_i} \mathrm{d}\boldsymbol{x}\mathrm{dt}, \end{aligned} \tag{5.15}$$

where $\boldsymbol{\xi}$ and q are Lagrange multipliers known as adjoint velocity and pressure states. Since the Lagrangian is an unconstrained functional, the first order optimality condition ensures that at the optimal point $(\overline{\boldsymbol{u}}, \overline{p}, \overline{\boldsymbol{\phi}}, \overline{\boldsymbol{\xi}}, \overline{q})$ the directional derivatives of the Lagrangian with respect to states, adjoint states and controls should vanish identically, such that

$$\mathcal{L}_{\boldsymbol{\xi}}(\boldsymbol{\xi}') = \mathcal{L}_q(q') = 0, \quad \Rightarrow \ \text{state equations} \tag{5.16}$$

$$\mathcal{L}_{\boldsymbol{u}}(\boldsymbol{u}') = \mathcal{L}_p(p') = 0, \quad \Rightarrow \ \text{adjoint equations} \tag{5.17}$$

$$\mathcal{L}_{\boldsymbol{\phi}}(\boldsymbol{\phi}') = 0, \quad \Rightarrow \ \text{design equations} \tag{5.18}$$

where the directional derivative, e.g. with respect to velocity $\boldsymbol{u}$ in the direction of $\boldsymbol{u}'$, reads as follows,

$$\mathcal{L}_{\cdot\boldsymbol{u}}(\boldsymbol{u}') \equiv \left.\frac{\mathrm{d}}{\mathrm{d}\alpha}\right|_{\alpha=0} \mathcal{L}(\boldsymbol{u} + \alpha\boldsymbol{u}', p, \boldsymbol{\phi}, \boldsymbol{\xi}, q). \tag{5.19}$$

The first optimality condition in Eq. (5.16) can be straightforwardly applied to the Lagrangian and the state equations, i.e. the incompressible Navier–Stokes equations in Eqs. (5.5)-(5.9), are obtained. The adjoint Navier–Stokes equations are derived from the second condition in Eq. (5.17). As the perturbations $\boldsymbol{u}'$ and p' are arbitrary, and independent from each other, $\mathcal{L}_{\boldsymbol{u}}(\boldsymbol{u}') = 0$ and $\mathcal{L}_p(p') = 0$

hold. From the first equality it follows

$$\begin{aligned}
0 &= \mathcal{L}_{\boldsymbol{u}}(\boldsymbol{u'}) \\
&= \int\int_{\overline{\Omega}_s} \frac{\partial^2 u_i}{\partial x_j \partial x_j} u_i' \mathrm{d}\boldsymbol{x}\mathrm{dt} \\
&+ \int\int_{\overline{\Omega}} \left(\frac{\partial u_i'}{\partial t} + \frac{\partial (u_j' u_i + u_j u_i')}{\partial x_j} + \frac{\partial p'}{\partial x_i} - \frac{1}{\mathrm{Re}_D} \frac{\partial^2 u_i'}{\partial x_j \partial x_j} \right) \xi_i \mathrm{d}\boldsymbol{x}\mathrm{dt} \\
&+ \int\int_{\overline{\Omega}} \frac{\partial u_i'}{\partial x_i} q \mathrm{d}\boldsymbol{x}\mathrm{dt},
\end{aligned}$$

where the vector identity ($\Delta \boldsymbol{u} = -\nabla \times (\nabla \times \boldsymbol{u})$, if $\nabla \cdot \boldsymbol{u} = 0$) is applied to the derivative of the enstrophy with respect to the velocity to get the first term on the right hand side. For the second and third terms on the right hand side, the differential operators have to be swapped over to the adjoint variables. To this end, we apply integration by parts, twice for the diffusive term, and obtain

$$\begin{aligned}
0 &= \mathcal{L}_{\boldsymbol{u}}(\boldsymbol{u'}) \\
&= \int\int_{\overline{\Omega}_s} \frac{\partial^2 u_i}{\partial x_j \partial x_j} u_i' \mathrm{d}\boldsymbol{x}\mathrm{dt} \\
&+ \int\int_{\overline{\Omega}} \left(-\frac{\partial \xi_i}{\partial t} - u_j \frac{\partial \xi_i}{\partial x_j} + \xi_j \frac{\partial u_j}{\partial x_i} - \frac{\partial q}{\partial x_i} - \frac{1}{\mathrm{Re}_D} \frac{\partial^2 \xi_i}{\partial x_j \partial x_j} \right) u_i' \mathrm{d}\boldsymbol{x}\mathrm{dt} \\
&+ \int\int_{\overline{\partial\Omega}} \xi_i \frac{\partial u_i'}{\partial x_j} n_j \mathrm{d}\boldsymbol{x}\mathrm{dt} + \int_{\Omega} \xi_i(T) u_i'(T) \mathrm{d}\boldsymbol{x},
\end{aligned} \tag{5.20}$$

where we have made use of the information from the boundary and initial conditions in Eq. (5.8)-(5.9) and explicitly forced the small variation $\boldsymbol{u'}$ to satisfy

$$u_i' = 0 \quad \text{on } \overline{\partial\Omega}, \text{ and} \qquad u_i'(0) = 0 \quad \text{in } \Omega. \tag{5.21}$$

Since $\boldsymbol{u'}$ and $\nabla \boldsymbol{u'} \cdot \boldsymbol{n}$ can vary freely in $\tilde{\Omega} := \Omega \times [0, T)$ and on $\widetilde{\partial\Omega} := \Omega \times [0, T)$ respectively we obtain the following adjoint momentum equation

$$-\frac{\partial \xi_i}{\partial t} - u_j \frac{\partial \xi_i}{\partial x_j} + \xi_j \frac{\partial u_j}{\partial x_i} - \frac{\partial q}{\partial x_i} - \frac{1}{\mathrm{Re}_D} \frac{\partial^2 \xi_i}{\partial x_j \partial x_j} = h_i \qquad \text{in } \tilde{\Omega} \tag{5.22}$$

$$h_i = \begin{cases} -\dfrac{\partial^2 u_i}{\partial x_j \partial x_j} & \text{in } \tilde{\Omega}_s := \Omega_s \times [0, T) \\ 0 & \text{in } \tilde{\Omega} \setminus \tilde{\Omega}_s \end{cases} ,$$

and boundary and initial conditions

$$\xi_i = 0 \quad \text{on } \partial\tilde{\Omega}, \text{ and} \qquad \xi_i(T) = 0 \quad \text{in } \Omega. \tag{5.23}$$

In addition to temporal, convective and diffusive terms, the adjoint momentum equation contains an additional term $\xi_j(\partial u_j/\partial x_i)$, will be referred to as *the transposed convection term.* An alternative version for this term can be derived by applying integration by parts on this term. Consequently an alternative form for the adjoint momentum equation is obtained

$$-\frac{\partial \xi_i}{\partial t} - u_j \frac{\partial \xi_i}{\partial x_j} - u_j \frac{\partial \xi_j}{\partial x_i} - \frac{\partial q}{\partial x_i} - \frac{1}{\mathrm{Re}_D} \frac{\partial^2 \xi_i}{\partial x_j \partial x_j} = h_i \qquad \text{in } \tilde{\Omega}, \tag{5.24}$$

with the alternative form of the transposed convection term $-u_j(\partial \xi_j/\partial x_i)$. The Dirichlet boundary conditions and the initial condition remain unchanged.

From the condition $\mathcal{L}_p(p') = 0$ we find the following expression

$$\begin{aligned} 0 &= \mathcal{L}_p(p') \\ &= \int \int_\Omega \frac{\partial p'}{\partial x_i} \xi_i \mathrm{d}\boldsymbol{x}\mathrm{dt} \\ &= -\int \int_\Omega \frac{\partial \xi_i}{\partial x_i} p' \mathrm{d}\boldsymbol{x}\mathrm{dt}, \end{aligned}$$

where we have made use of homogeneous adjoint velocity boundary conditions to remove boundary terms from the expression. As p' can be chosen freely in $\tilde{\Omega}$, we obtain the adjoint continuity equation

$$\frac{\partial \xi_i}{\partial x_i} = 0 \quad \text{in } \tilde{\Omega}.$$

Finally, we conclude the derivation by taking the directional derivative of the Lagrangian $\mathcal{L}$ with respect to control variable $\boldsymbol{\phi}$, such that

$$\begin{aligned} 0 &= \mathcal{L}_{\boldsymbol{\phi}}(\boldsymbol{\phi}') \\ &= \int \int_{\overline{\Omega}_c} (\gamma \phi_i - \xi_i) \phi_i' \mathrm{d}\boldsymbol{x}\mathrm{dt}, \end{aligned}$$

and obtain the design equations

$$\gamma \phi_i - \xi_i = 0, \qquad \text{on } \overline{\Omega}_c. \tag{5.25}$$

Consequently, the optimality system reads as follows

$$\frac{\partial u_i}{\partial t} + \frac{\partial u_j u_i}{\partial x_j} + \frac{\partial p}{\partial x_i} - \frac{1}{\mathrm{Re}_D}\frac{\partial^2 u_i}{\partial x_j \partial x_j} = f_i \quad \text{in } \overline{\Omega}, \tag{5.26}$$

$$\frac{\partial u_i}{\partial x_i} = 0 \quad \text{in } \overline{\Omega}, \tag{5.27}$$

$$f_i = \begin{cases} \phi_i & \text{in } \overline{\Omega}_c \\ 0 & \text{in } \overline{\Omega} \setminus \overline{\Omega}_c \end{cases}, \tag{5.28}$$

$$u_i = g_i \quad \text{on } \overline{\partial\Omega}, \tag{5.29}$$

$$u_i(0) = u_i^0 \quad \text{in } \Omega, \tag{5.30}$$

$$-\frac{\partial \xi_i}{\partial t} - u_j \frac{\partial \xi_i}{\partial x_j} + \xi_j \frac{\partial u_j}{\partial x_i} - \frac{\partial q}{\partial x_i} - \frac{1}{\mathrm{Re}_D}\frac{\partial^2 \xi_i}{\partial x_j \partial x_j} = h_i \qquad \text{in } \tilde{\Omega}, \tag{5.31}$$

$$\frac{\partial \xi_i}{\partial x_i} = 0 \quad \text{in } \tilde{\Omega}, \tag{5.32}$$

$$h_i = \begin{cases} -\dfrac{\partial^2 u_i}{\partial x_j \partial x_j} & \text{in } \tilde{\Omega}_s \\ 0 & \text{in } \tilde{\Omega} \setminus \tilde{\Omega}_s \end{cases}, \tag{5.33}$$

$$\xi_i = 0 \quad \text{on } \tilde{\partial\Omega}, \tag{5.34}$$

$$\xi_i(T) = 0 \quad \text{in } \Omega. \tag{5.35}$$

$$\gamma\phi_i - \xi_i = 0, \qquad \text{on } \overline{\Omega}_c. \tag{5.36}$$

Eqs. (5.26)-(5.30) are the state equations, Eqs. (5.31)-(5.35) are the adjoint equations, and Eq. (5.36) is the design equation.

5.1.4 Gradient–based minimization

The optimality system in Eqs. (5.26)-(5.36) is a set of strongly coupled partial differential equations containing nonlinearity. Therefore, it has to be solved iteratively. However, an iterative solution to this coupled system is computationally very demanding considering the size of DNS and LES simulations. Thus, for large-scale turbulence problems, generic optimization algorithms that are designed to minimize the reduced cost functional $\tilde{\mathcal{J}}$, are employed. To this end, first-order gradient-based methods such as the steepest-descent method and the nonlinear conjugate-gradient method are common choices because of their low storage requirements [11, 52].

The method of choice in this study is the steepest descent method with a backtracking line-search. This simple method delivers a reasonable reduction in the cost functional in the first few optimization iterations, cf. e.g. Ref. [25]. It employs the negative of the reduced gradient to update the control fields every outer iteration. The reduced gradient can be found from the Lagrangian $\mathcal{L}$ as follows

$$\left(\nabla\tilde{\mathcal{J}}, \boldsymbol{\phi}'\right)_{\mathcal{H}_c} = \left(\nabla_{\boldsymbol{\phi}}\mathcal{L}, \boldsymbol{\phi}'\right)_{\mathcal{H}_c} := \mathcal{L}_{\boldsymbol{\phi}}(\boldsymbol{\phi}') \quad \forall \boldsymbol{\phi}' \in \mathcal{H}_c. \tag{5.37}$$

The reader is referred to [111] for a derivation of this result. Using the Eq. 5.36, the reduced gradient is now given by

$$\nabla\tilde{\mathcal{J}}(\boldsymbol{\phi}) = \gamma\boldsymbol{\phi} - \boldsymbol{\xi}. \tag{5.38}$$

Basic steps of the selected steepest descent algorithm for the infinite-dimensional jet optimization is given in Algorithm 5.1. The norm $\|\cdot\|_{\mathcal{H}_c}$ in the algorithm is found from the scalar product in Eq. 5.12, i.e.,

$$\|\boldsymbol{\phi}\|_{\mathcal{H}_c} := \sqrt{(\boldsymbol{\phi}, \boldsymbol{\phi})_{\mathcal{H}_c}} \quad \forall \boldsymbol{\phi} \in \mathcal{H}_c. \tag{5.39}$$

In this study we have selected the following values for the free parameters in the algorithm: $\beta = 10^{-4}$, $\kappa = 0.1$, and $\eta = 0.25$.

5.2 Discretization of the adjoint equations

In the previous section, a jet flow optimization problem and a gradient-based optimization algorithm to solve this problem were introduced. The optimization algorithm was in infinite-dimensional setting. The gradient-based algorithm requires the solution of the state equations, usually multiple times due to the line search, and the adjoint equations at each outer iteration. Discretization of the state equations, i.e., the incompressible Navier-Stokes equations, is already discussed in Chapter 2. The discretization of the adjoint incompressible Navier–Stokes equations in (5.31)-(5.35) is discussed in this section.

OpenFOAM® v2.3.x includes an adjoint solver entitled *adjointShapeOptimizationFoam*, which is based on the work of Othmer [97]. This solver is developed to calculate gradients for shape optimization problems using RANS. Being a

Algorithm 5.1 (The steepest descent algorithm)

```
I initialization:
    i Choose an initial control field $\boldsymbol{\phi}_0$;
    ii Solve the state equations in (5.26)-(5.30) forward in time with $\boldsymbol{\phi}_0$, and obtain the corresponding state field $\boldsymbol{u}_0$ and functional value $\tilde{\mathcal{J}}(\boldsymbol{\phi}_0)$;
II main optimization loop, i.e. for $m = 1, 2, 3, \ldots$:
    i Solve the adjoint equations in (5.31)-(5.35) backward in time with $\boldsymbol{u}_{m-1}$ and obtain the adjoint field $\boldsymbol{\xi}_m$;
    ii Evaluate the gradient $\nabla\tilde{\mathcal{J}}(\boldsymbol{\phi}_{m-1}) = \gamma\boldsymbol{\phi}_{m-1} - \boldsymbol{\xi}_m$;
    iii Set a minimum limit $\tilde{\mathcal{J}}^g$ by Armijo rule [55, 69] to ensure a sufficient decrease, i.e.
            $$\tilde{\mathcal{J}}^g = \tilde{\mathcal{J}}(\boldsymbol{\phi}_{m-1}) - \beta\left(\|\nabla\tilde{\mathcal{J}}(\boldsymbol{\phi}_{m-1})\|_{\mathcal{H}_c}\right)^2;$$
    iv Set the initial step size $\lambda = \kappa\|\boldsymbol{\phi}_{m-1}\|_{\mathcal{H}_c}$;
    v Update the controls $\boldsymbol{\phi}_m = \boldsymbol{\phi}_{m-1} - \lambda\nabla\tilde{\mathcal{J}}(\boldsymbol{\phi}_{m-1})$;
    vi Solve the state equations in (5.26)-(5.30) forward in time with $\boldsymbol{\phi}_m$, and obtain $\boldsymbol{u}_m$ and $\tilde{\mathcal{J}}(\boldsymbol{\phi}_m)$;
    vii If $\tilde{\mathcal{J}}(\boldsymbol{\phi}_m) > \tilde{\mathcal{J}}^g$ set $\lambda = \eta\lambda$ and go to step (v); otherwise, set $m = m+1$, and go to step (i);
```

steady solver using the SIMPLE scheme, it is not suitable for unsteady problems. An unsteady adjoint solver requires a machinery for backward-in-time stepping with changing velocity fields at every time step. Therefore, a new adjoint solver using the adjoint version of the incremental projection scheme, cf. Chapter 2, is developed. The adjoint projection scheme will be introduced following some remarks about the spatial discretization.

The spatial discretization of the adjoint incompressible Navier–Stokes equations follows closely their primal counterparts. The main difference is in the discretization of the additional transposed convection term $\xi_j(\partial u_j/\partial x_i)$, or in its alternative form $-u_j(\partial \xi_j/\partial x_i)$. The spatial discretization of this term on an unstructured is carried out as follows

$$\left(\xi_j \frac{\partial u_j}{\partial x_i}\right)^k \approx \frac{\xi_j^k}{|\Omega_k|} \sum_{f=1}^{N_{kf}} u_j^f n_i^f |\partial\Omega_k^f|, \tag{5.40}$$

where the superscripts k and f denote evaluations in element and face centroids respectively, $|\Omega_k|$ is the volume of a polyhedral element, $|\Omega_k^f|$ is the area of the element face and n^f its corresponding unit normal, and N_{kf} is the total number of faces around the element. Similar spatial discretization can be applied to the alternative form.

The spatial discretization in Eq. (5.40) couples the adjoint velocity components. Since OpenFOAM® does not support the coupling of the velocity components at the time of this study, the temporal discretization of the transposed convection term cannot be handled implicitly. Therefore, a second-order Adams–Bashforth scheme is employed to discretize the cross-convection term in time. Consequently, the adjoint version of the incremental projection scheme in Section 2.4.2 using a semi-implicit backward in time stepping is formulated as follows:

1. Momentum step: Solve for the preliminary velocity $\tilde{\xi}_i^n$;

$$\frac{\tilde{\xi_i}^n - \xi_i^{n+1}}{\delta t} + u_j^{n+\theta} \frac{\partial \tilde{\xi_i}^{n+\theta}}{\partial x_j} + c_i = \frac{1}{\mathrm{Re}_D} \frac{\partial^2 \tilde{\xi_i}^{n+\theta}}{\partial x_j \partial x_j} - \frac{\partial q^{n+1}}{\partial x_i} + h_i^n \quad \text{in } \Omega, \tag{5.41}$$

$$\tilde{\xi}_i^n = g_i^n \quad \text{on } \partial\Omega, \tag{5.42}$$

where

$$\tilde{\xi_i}^{n+\theta} = \theta \tilde{\xi}^n + (1-\theta)\,\xi^{n+1}, \tag{5.43}$$

$$c_i = \frac{3}{2}\xi_j^{n+1} \frac{\partial {u_i}^{n+1}}{\partial x_j} - \frac{1}{2}\xi_j^{n+2} \frac{\partial {u_i}^{n+2}}{\partial x_j}, \text{ or} \tag{5.44}$$

$$c_i = -\frac{3}{2}u_j^{n+1} \frac{\partial {\xi_i}^{n+1}}{\partial x_j} + \frac{1}{2}u_j^{n+2} \frac{\partial {\xi_i}^{n+2}}{\partial x_j}. \tag{5.45}$$

2. Projection step: Perform the projection ${\xi_i}^n = P({\tilde{\xi_i}}^n)$;

$$\frac{({\xi_i}^n - {\tilde{\xi_i}}^n)}{\delta t} + \frac{\partial(q^n - q^{n+1})}{\partial x_i} = 0 \quad \text{in } \Omega,$$

by solving first

$$\frac{\partial^2 \left(q^n - q^{n+1}\right)}{\partial x_i \partial x_i} = \frac{1}{\delta t}\frac{\partial {\tilde{\xi_i}}^n}{\partial x_i} \quad \text{in } \Omega, \tag{5.46}$$

$$\frac{\partial \left(q^n - q^{n+1}\right)}{\partial x_i} n_i = 0 \quad \text{on } \partial\Omega, \tag{5.47}$$

then, updating the velocity

$$\xi_i^n = {\tilde{\xi_i}}^n - \delta t \frac{\partial \left(q^n - q^{n+1}\right)}{\partial x_i}, \quad \text{in } \Omega, \tag{5.48}$$

$$\xi_i^n = g_i^n \quad \text{on } \partial\Omega. \tag{5.49}$$

This algorithm delivers oscillatory results if the form in Eq. (5.45) is employed for the transposed convection term. An example using the turbulent jet case from Chapter 6 can be seen in Figure 5.2 where a wiggle-like behaviour around the jet inlet is observed for the case using Eq. (5.45). Thus, only the form in Eq. (5.44) is further considered in this study.

5.3 Issues concerning the adjoint-based gradient

There are two fundamental methodological issues concerning the adjoint-based calculation of the gradient when it is applied to turbulent jets. The first issue is related to the chaotic character of the turbulent flows, i.e., extreme sensitivity to initial conditions, causing a blow-up in the magnitude of the adjoint fields. Lea et al. [79] demonstrated this problem using a simplified chaotic case: a Lorentz system. They claimed that the adjoint method is a limited utility to calculate the sensitivity of time-averaged properties of the system. In their analysis, they used different integration time windows that are referred to as intermediate, long and very long. Intermediate integration completes a full orbit around the Lorenz attractor, long integration allows the completion of several of such orbits and very long integrations travel around the attractor many times, e.g. $O(100)$. The adjoint results for intermediate and long integrations were approaching direct sensitivity results over much of the parameter range but they were still

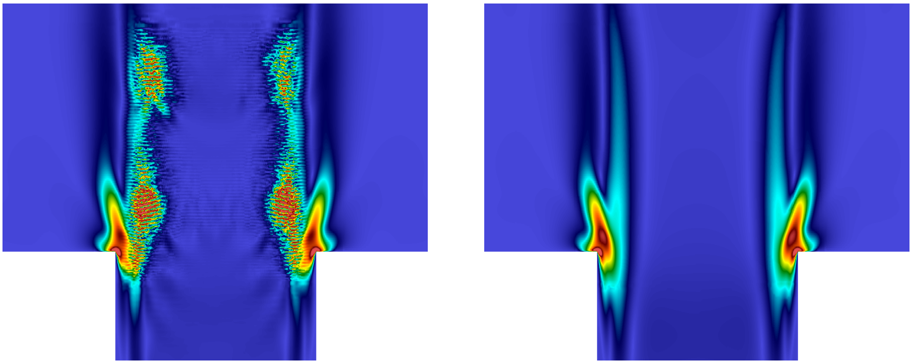

Figure 5.2: Demonstration of the instability concerning the cross-convection term using a snapshot of the magnitude of the adjoint velocity $\boldsymbol{\xi}$ in the inlet region of a turbulent jet. The case setup can be found in Chapter 6. (left): $|\boldsymbol{\xi}|$ using Eq. (5.45); (right): $|\boldsymbol{\xi}|$ using Eq. (5.44).

extremely inaccurate for certain values. In general, a reasonable estimation with an error of $O(10\%)$ is obtained. The adjoint method delivered completely useless gradient, with order of magnitude values around 10^{100} for very long time integrations. They concluded that there is a cumulative error growth due to one of the system's unstable modes with positive Lyapunov exponent, which causes this exponential divergence.

We observed similar issues in the turbulent round jet case. If the optimization time window is long enough to allow many through-flow times, e.g. $O(10)$ through-flow times in a domain with a length of $10D$, then the adjoint fields diverge and reach extremely high values. If we limit the time horizon, and just let the initial jet develop throughout the domain, then adjoint fields with reasonable magnitudes are obtained. This limitation of the adjoint method due to chaotic character is not exploited in the turbulent flow community yet. The main reason for this is the excessive storage cost of the adjoint method when applied to DNS and LES. This huge storage demand artificially limited the time horizons in the turbulent flow optimization studies with DNS and LES. Therefore, problems due to chaotic behaviour did not rise. However, the increasing availability of storage resources requires a solution to this issue of divergent adjoint fields for long time horizons. Very recently, Blonigan et al. proposed a Least-Squares Shadowing method to overcome this issue [12]. The method is based on approximating the shadow trajectory in phase space, and preventing the high sensitivity to the initial conditions. This approach is very new, and still requires a lot of research, and therefore falls outside of the scope of the current work.

The second issue concerning the adjoint methodology is related to the noise-amplifier character of the round jets, which causes an extremely non-uniform distribution in the adjoint velocity fields. In noise-amplifier flows, there are no intrinsic global instabilities in the flow, but the perturbations grow downstream as the result of convective instabilities [59]. The overall dynamics are therefore extrinsic and the flow acts like a fine-tuned amplifier to perturbations [58]. Thus, the flow is extremely sensitive to upstream perturbations, and even perturbations with very small amplitudes can alter global flow states. This extremely sensitive character results in the adjoint velocity fields that are exponentially growing while moving towards the jet inlet. Thus, the adjoint-jet problem has completely different nature than the forward jet problem. In the forward problem, the nonlinearity is dominant and the exponential growth of perturbations can be seen only in initial parts of the shear layer.

As the amplification mechanisms originate from the jet shear layer, very high adjoint velocity values concentrate in this small region. Moreover, the controls are usually placed also in this region, and the gradient of the cost functional has to be computed from the adjoint fields here. Therefore, accurate computation of the gradient becomes an extremely challenging numerical problem. In general, a computational grid merely designed to solve the forward DNS, or LES, problem will fail to resolve the adjoint velocity in the shear layer and eventually compute erroneous gradients for the optimization loop.

Both issues discussed in this section, originate from the extreme sensitivity of the jet to perturbations: in time due to the chaotic character of turbulence, and in space due to the noise-amplifier character of jet flows. Therefore, optimization in a long jet domain over a long time horizon is conceptually not possible. This is illustrated with a 2D Bickley jet example. In this example, a jet enters a large 2D domain through a 2D channel with a width of D. The Reynolds number $\mathrm{Re}_D = 800$. Two ZNMF boundary controls are located at each side of the jet inlet. Their signals are determined by a finite Fourier series. The optimization is carried out for the Fourier coefficients in these series. The reader is referred to Chapter 6 for the details of this control design in a distributed framework. A cost functional measuring the enstrophy in an observation domain $\Omega_s := [-20D, 20D] \times [5D, 100D]$ over a time horizon T of 10 through-flow times is selected.

A planar computational domain extending up to $120D$ downstream the jet inlet and up to $30D$ from the jet centreline is built. Additionally, a 2D channel with a length $30D$ is attached to the large domain. The computational domain is discretized with approximately 4.3×10^6 quadrilateral elements. In order to solve the primal Navier–Stokes equations, the incremental projection scheme in

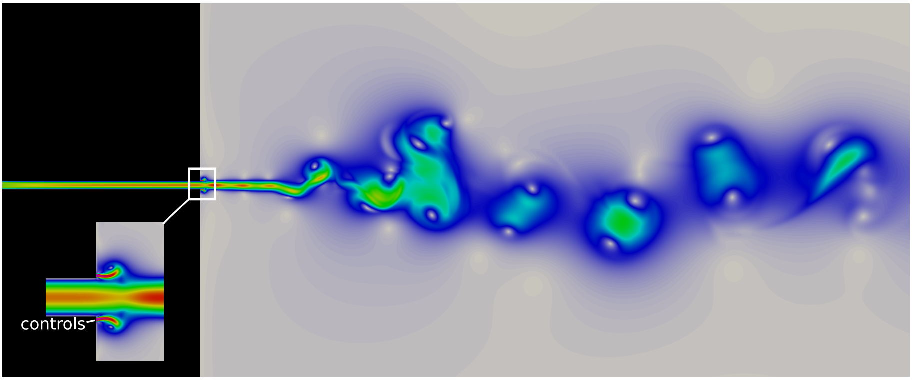

(a) Magnitude of velocity

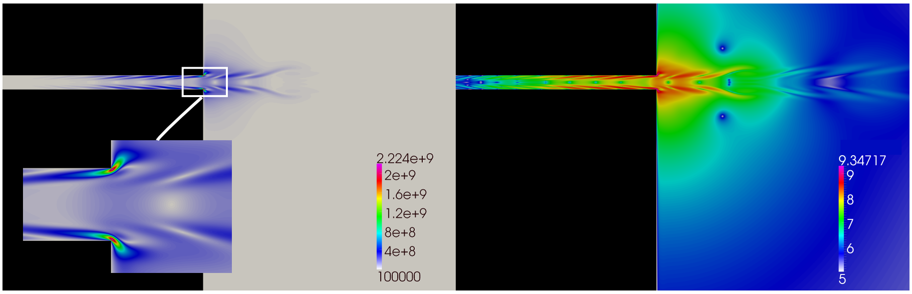

(b) Magnitude of adjoint velocity; colormap in (left): linear scale (right): logarithmic scale

Figure 5.3: Exponential growth of the adjoint fields in the 2D Bickley jet case.

Chapter 2 is employed. The adjoint version of this scheme is employed for the solution of the adjoint equations. The time step is selected to be $0.0001U_J/D$ where U_J is the uniform velocity at the pipe inlet.

The resulting adjoint velocity fields are illustrated in Figure 5.3 using a time instance $t = 0.2T$. We observe that the adjoint fields grow exponentially in space towards to the jet inlet. They also grow exponentially in time while stepping backwards in time (not shown here). As a result, in the regions, where the controls are placed, the adjoint velocity field reaches up to the values of $O(10^{10})$.

Chapter 6

Optimal control of a transitional axisymmetric jet

This section is devoted to the application of the continuous adjoint methodology, described in Chapter 5, to axisymmetic jet flow. In Chapter 4, we analyzed the fluid response to single frequency actuation with ZNMF actuators. We found that actuation with the preferred mode enables most large-structure growth, and yields dramatic changes in global jet characteristics such as entrainment rate, decay rate of centreline velocity and passive scalar. Although, these metrics are helpful to provide a general view of mixing in the flow, they are more sensitive to the large-scale events. Therefore, they do not capture the characteristics of the small scale motion which plays an essential role in molecular mixing [35]. In fact, it can be seen on Figure 4.5, that the Case *C1* with preferred mode actuation has a delayed smaller scale vortex development compared to the cases with higher frequency actuation, i.e., Case *C2* and Case *C4*. This is due to the fact that enhanced coherence in the flow increases the strength and stability of large scale structures and therefore delays their breakdown into smaller scales, as also previously suggested by Ref. [93].

As discussed in Chapter 1, mixing augmentation is a highly challenging multi–scale control problem where all the scales of turbulent motion should be properly addressed by controls. To this end, adjoint-based control is a promising tool, as the cost for the evaluation of the gradient is insensitive to the dimension of controls and therefore high-dimensional control designs covering a wide range of frequencies are possible. Moreover, such a control design can exploit high bandwidth capabilities of the ZNMF actuators.

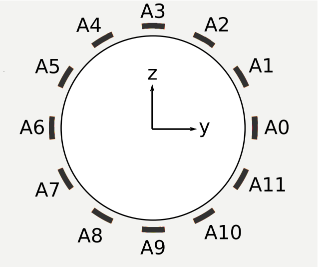

Figure 6.1: Configuration of forcing regions.

Table 6.1: Geometry of the actuation regions in cylindrical coordinates

	length	width	depth
direction	r	θ	z
value	$0.03D$	$0.14D$	$0.035D$

In this chapter, an optimal distributed control study for an axisymmetric jet at $\mathrm{Re}_D = 2000$ is performed. The controls are modelled as small localized regions around the jet circumference with a uniform forcing distribution. In Chapter 4, we saw that the development of primary and secondary vortices in the transition region is initiated by the distortions in the azimuthal curvature of the controlled jet. Therefore, forcing is applied only in the radial direction, which is sufficient to introduce cross-stream perturbations and break down the axisymmetry of the main jet.

The aim of the study is to enhance the integrated enstrophy of a transient jet in the near field region extending up to $x = 6D$. The enstrophy can be linked to the mixing characteristics of the flow (cf. Section 5.1.1 for a discussion). The observation domain is selected to be relatively short, as the noise amplifier character and chaotic behaviour of turbulent jets cause a divergence in the adjoint fields in larger observation domains, requiring longer optimization horizons (cf. Section 5.3 for a discussion).

6.1 Configuration of the optimization problem

6.1.1 Configuration of the controls

The primary purpose of the distributed controls is to model ZNMF actuation. To this end, twelve small hexahedral forcing regions are distributed around the jet circumference to resemble the synthetic jet model in Chapter 4. The configuration is illustrated in Figure 6.1. In order to adjust the forcing regions to the underlying O-grid, their shape is designed in cylindrical coordinates and the corresponding dimensions are summarized in Table 6.1. The center of the actuators is $0.1D$ downstream from the jet inlet plane and $0.55D$ away from the jet axis.

The forcing is one-dimensional and is aligned with radial direction and has a uniform spatial distribution in the actuation region. The control signals are designed as finite Fourier series. The control parameters to optimize are the Fourier coefficients in these Fourier series. This can be formulated as follows: the forcing signal of each actuator $k \in \{1, \dots, M\}$ occupying a domain Ω_c^k is designated with a periodic signal reading as follows

$$\boldsymbol{\phi}^h(x,t) = -\boldsymbol{e}_r^k \sum_{n=1}^{N} \left(\alpha_m \sin(2\pi(nf_o)t) + \alpha_{m+1}\cos(2\pi(nf_o)t)\right), \quad \forall \boldsymbol{x} \in \Omega_c^k. \tag{6.1}$$

where $m = (k-1) \times 2n + 2n - 1$, $\boldsymbol{e}_r^k$ is the unit vector in radial direction, M is the total number of actuators, N is the total number of frequencies, f_o is the fundamental control frequency, and $\boldsymbol{\alpha} \in \mathbb{R}^K$ is the finite-dimensional control vector with $K = 2NM$. In the current study, the fundamental frequency $f_0 = 0.5\mathrm{St}_D$, where $\mathrm{St}_D = 0.33$. Each actuator has $N = 10$ Fourier components, and therefore the highest frequency component considered is $10f_0 = 5\mathrm{St}_D$.

In Chapter 5 the gradient of the reduced cost funtional is derived using continous controls. Now this derivation is extended for the discrete controls. In order to find the gradient of the reduced cost functional with respect to Fourier coefficients $\boldsymbol{\alpha}$, we replace $\boldsymbol{\phi}$ with $\boldsymbol{\phi}^h$ in the Lagrangian $\mathcal{L}$ in Eq. (5.15) in Chapter 5 and take the directional derivative of the $\mathcal{L}$ with respect to an arbitrary perturbation $\boldsymbol{\alpha}' \in \mathbb{R}^K$, such that

$$\begin{aligned} 0 &= \mathcal{L}_\alpha(\alpha') \\ &= \sum_{m=1}^{K} \left(\int_0^T \gamma\alpha_m \mathrm{dt} + \int_0^{\mathrm{T}} \int_{\Omega_\mathrm{c}} \frac{\partial \phi_\mathrm{i}^\mathrm{h}}{\partial \alpha_\mathrm{m}} \xi_\mathrm{i} \mathrm{d}\boldsymbol{x}\mathrm{dt} \right) \alpha_m', \end{aligned}$$

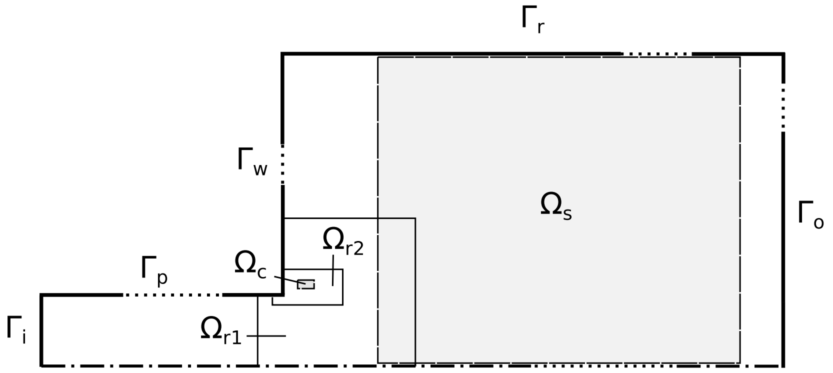

Figure 6.2: Schematic representation of the cylindrical computational domain using a cut at $\theta = 0$. Sizes are indicative.

where the derivative $\partial \boldsymbol{\phi}^h / \partial \alpha_m$ is calculated using Eq. (6.1) as follows

$$\frac{\partial \boldsymbol{\phi}^h}{\partial \alpha_m} = -\boldsymbol{e}_r^k \cos(2\pi(nf_o)t),$$

and

$$\frac{\partial \boldsymbol{\phi}^h}{\partial \alpha_{m+1}} = \boldsymbol{e}_r^k \sin(2\pi(nf_o)t).$$

If we use the finite-dimensional scalar product and define the discrete reduced gradient $\nabla \tilde{\mathcal{J}}^h$ as follows

$$\left(\nabla \tilde{\mathcal{J}}^h, \boldsymbol{\alpha}'\right) = \left(\nabla_{\boldsymbol{\alpha}} \mathcal{L}, \boldsymbol{\alpha}'\right) := \mathcal{L}_{\boldsymbol{\alpha}}(\boldsymbol{\alpha}') \quad \forall \boldsymbol{\alpha}' \in \mathbb{R}^K, \tag{6.2}$$

then we obtain

$$\nabla \tilde{\mathcal{J}}^h(\boldsymbol{\alpha}) = \gamma \boldsymbol{\alpha} T + \int_0^T \int_{\Omega_c} \frac{\partial \phi_i^h}{\partial \boldsymbol{\alpha}} \xi_i \mathrm{d}\boldsymbol{x}\mathrm{d}t, \tag{6.3}$$

, where we analytically integrated the penalization term. The integral containing the adjoint variable is evaluated with the midpoint rule. As only this discrete gradient will be used hereafter, we will drop the superscript h.

6.1.2 Numerical details

The open-source C++ library OpenFOAM® is employed in this study (using the v2.3.x distribution). A schematic representation for the computational domain is illustrated in Figure 6.2. The domain consists of two parts. A large cylindrical jet domain, which extends $L = 8D$ in the axial direction and $R = 5D$ in the radial direction, is attached to a small pipe domain with $R_p = 0.5D$ and $L_p = 8D$. The pipe is introduced to allow the adjoint fields to exit the jet domain while moving upstream with negative convection.

The domain is discretized with an O-grid type of computational grid, similar to the one described in Section 2.4.5. There are two main differences. Firstly, the overall grid density is approximately three times higher as the additional transposed convection term yields an adjoint flow with finer scales compared to the primal flow. Secondly, we applied two levels of local grid refinements in the control regions. The motivation for these refinements is to resolve the adjoint fields in the control regions and provide accurate gradient information. Each level of refinement doubles the grid density in every direction. The first level of refinement is applied in the domain $\Omega_{r1} = [0, 0.8D] \times [0, 2\pi] \times [-0.2D, D]$, which is defined in the radial, azimuthal and axial directions respectively. An additional level of refinement is applied in the domain $\Omega_{r2} = [0.48D, 0.6D] \times [0, 2\pi] \times [0.025D, 0.5D]$. Overall, the computational grid consists of approximately 184×10^6 computational elements.

The primal and adjoint Navier–Stokes equations are solved with DNS without any explicit turbulence modelling. The system of equations for primal and adjoint euations are segregated with corresponding incremental projection algorithms presented in Chapter 2 and Chapter 5 respectively. The details of the spatial discretization are discussed in Chapter 2 for the forward problem and in Chapter 5 for the adjoint problem. The very fine grid resolution in control regions requires a modification in the temporal discretization compared to the one employed in the DNS study in Chapter 4. In order to keep the study feasible, we increase the implicitness parameter θ introduced in Section 2.3, to $\theta = 0.66$ for the primal DNS problem, and to $\theta = 0.9$ for the adjoint problem. This increment allowed a time step of $\delta t = 0.0303DU_J^{-1}$, enabling us to resolve one period of actuation for the highest frequency component $(5\mathrm{St}_D)$ with 20 time steps.

The boundary conditions at lateral Γ_r and outflow Γ_o boundaries correspond respectively to $\partial u_i/\partial r = 0$, and $\partial u_i/\partial x = 0$ for the velocity, and in the same way, $\partial \xi_i/\partial r = 0$, and $\partial \xi_i/\partial x = 0$ for the adjoint velocity. No inflow is allowed on the outflow boundary for velocity fields. On the inlet Γ_i and pipe Γ_p boundaries, the velocity has a uniform profile in the axial direction, i.e., $u_x = U_J$, and the adjoint velocity vanishes, i.e., $\xi_i = 0$.

Initial fields for the velocity are produced by allowing an uncontrolled jet develop in the domain. As there is no random perturbation introduced, the jet remains laminar in the domain. The initial condition for the adjoint velocity is the zero

Table 6.2: Comparison of adjoint and finite-difference gradients for five different time horizons T using the measure e_g in Eq. (6.4).

T	T_{pm}	$2T_{pm}$	$3T_{pm}$	$4T_{pm}$	$5T_{pm}$
e_g	0.0003	0.0012	0.0079	0.0078	0.0043
$\|\nabla\tilde{\mathcal{J}}_a\|/\|\nabla\tilde{\mathcal{J}}_{fd}\|$	0.9814	0.8723	0.6948	0.8344	0.7178

field, as already derived in Chapter 5.

6.2 Verification of the adjoint-based gradient

In this section, the adjoint-based gradients are compared to finite-difference gradients for the transitional jet case at $\mathrm{Re}_D = 2000$. As the critical information for the steepest descent method is the direction of the gradient, the main motivation is to verify the accuracy of this direction. To this end, a subset $\boldsymbol{\alpha}_{A0} \in \mathbb{R}^{10}$ corresponding to Fourier coefficients of cosine components in the forcing region $A0$ is extracted from $\boldsymbol{\alpha} \in \mathbb{R}^K$ and the following error measure to quantify the accuracy of the gradient direction is introduced

$$e_g := 1 - \frac{\nabla\tilde{\mathcal{J}}_a \cdot \nabla\tilde{\mathcal{J}}_{fd}}{\|\nabla\tilde{\mathcal{J}}_a\|\|\nabla\tilde{\mathcal{J}}_{fd}\|}, \tag{6.4}$$

where $\nabla\tilde{\mathcal{J}}_a \in \mathbb{R}^{10}$ is the gradient of the reduced cost functional with respect to the control parameters in $\boldsymbol{\alpha}_{A0}$, which is calculated by the adjoint method with the Eq. (6.3), and $\nabla\tilde{\mathcal{J}}_{fd} \in \mathbb{R}^{10}$ is the finite-difference gradient calculated by

$$(\nabla\tilde{\mathcal{J}}_{fd}(\boldsymbol{\alpha}))_i := \frac{\tilde{\mathcal{J}}(\boldsymbol{\alpha} + \epsilon\boldsymbol{\delta\alpha}_i) - \tilde{\mathcal{J}}(\boldsymbol{\alpha})}{\epsilon}, \tag{6.5}$$

where $\boldsymbol{\delta\alpha}_i = [0, \ldots, 1, \ldots, 0]$ is the perturbation direction regarding the cosine component, and $\epsilon = 10^{-6}\alpha_i$ is selected as the magnitude of perturbation.

We evaluate the gradient for five different time horizons $T = T_{pm}, \ldots, 5T_{pm}$ at a control point $\boldsymbol{\alpha}_r$ with uniform coefficients, i.e.,

$$\boldsymbol{\alpha}_r = [0.1\mathcal{F}_0, \ldots, 0.1\mathcal{F}_0],$$

where $\mathcal{F}_0 = 1.8(U_J^2/D)$, and T_{pm} is the preferred mode period. The observation domain is described in Section 6.3. The calculation of e_g for each time horizon requires one primal solution for the evaluation at the reference point $\boldsymbol{\alpha}_r$, ten additional primal solutions to calculate the finite-difference gradient $\nabla\tilde{\mathcal{J}}_{fd}(\boldsymbol{\alpha}_r)$

Table 6.3: Initial conditions for two optimization cases. Case *OC2* has additional random forcing components that are not shown here, see the text for the description.

Case	*A0*	*A4*	*A8*
OC1	$\mathcal{F}_0 \cos(2\pi \mathrm{St}_{pm} t)$	$\mathcal{F}_0 \cos(2\pi \mathrm{St}_{pm} t)$	$\mathcal{F}_0 \cos(2\pi \mathrm{St}_{pm} t)$
OC2	$\mathcal{F}_0 \cos(2\pi (2\mathrm{St}_{pm}) t)$	$\mathcal{F}_0 \cos(2\pi (2\mathrm{St}_{pm}) t)$	$\mathcal{F}_0 \cos(2\pi (2\mathrm{St}_{pm}) t)$

Table 6.4: Summary of optimization results. The subscripts 0 and f denote the values at initial and final iterations respectively.

Case	# outer iterations	$\tilde{\mathcal{J}}_f / \tilde{\mathcal{J}}_0$	$\|\boldsymbol{\alpha}_f\| / \|\boldsymbol{\alpha}_0\|$
OC1	18	1.1049	1.0038
OC2	9	1.0560	1.0317

and one adjoint solution to compute $\nabla \tilde{\mathcal{J}}_a(\boldsymbol{\alpha}_r)$. Therefore, this verification study covering five different time horizons requires 60 PDE solutions in total.

The results are presented in the Table 6.2. The direction of the adjoint gradients are in very good alignment with the direction of the finite-difference gradients. We also observe that the norm of the adjoint gradients remains lower in magnitude compared to the norm of the finite-difference gradients. We believe that this is due to the fact that the high implicitness parameter ($\theta = 0.9$), employed in the temporal discretization of the adjoint equations introduces strong numerical diffusion.

6.3 Optimization of the distributed controls

In this section, the results of the optimization study are presented. The aim is to maximize the enstrophy measured in an observation domain Ω_s over a time window $T = (0, T]$. The cost functional with a penalization on controls is given in Eq. (5.4) in Chapter 5. The observation domain Ω_s is selected to be $\Omega_s = [0, 5D] \times [0, 2\pi] \times [0.6D, 6D]$, in the radial, azimuthal and axial directions respectively. The optimization horizon $T = 4T_{pm}$. This value of T requires the storage of 400 velocity time steps, which occupy an overall storage space of approximately 4 terabytes. The simulations are run using 200 processors on the *Thinking* cluster of Flemish Supercomputer Center (VSC). A primal solution lasts approximately 12 hours, and an adjoint solution lasts approximately 15 hours.

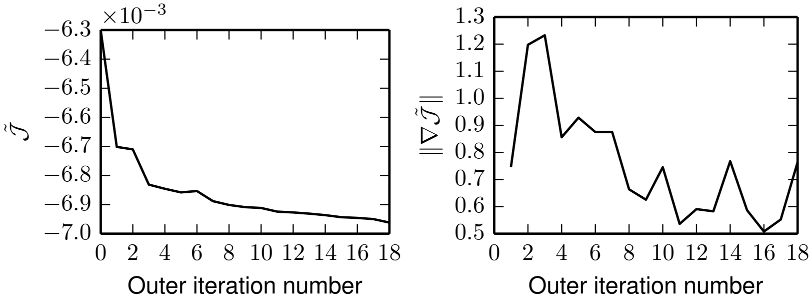

(a) Case *OC1*

(b) Case *OC1*

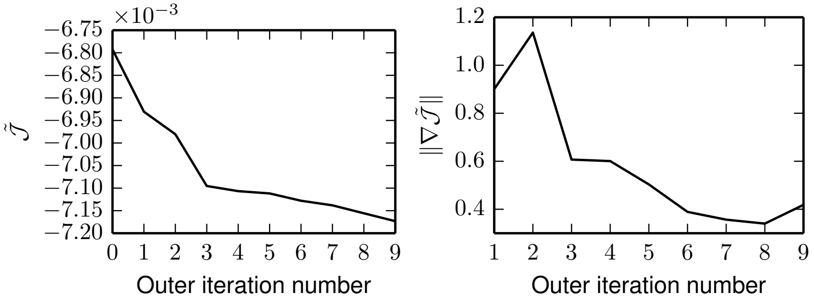

(c) Case *OC2*

(d) Case *OC2*

Figure 6.3: Optimization results for Cases *OC1* and *OC2*. (a),(c): cost functional; (b),(d): norm of the reduced gradient,

Since gradient-based methods are known to converge to local optima [31], two optimization cases with different initial conditions are considered. These cases are presented in Table 6.3. In the Case *OC1*, the initial condition is inspired from the Case *C1* in Chapter 4, i.e, only three actuators, *A0*, *A4*, *A8*, are active and are driven in phase with the preferred mode frequency St_D. The magnitude of the actuation is $\mathcal{F}_0 = 1.8(U_J^2/D)$. This forcing magnitude is found to deliver a radial perturbation of the velocity reaching up to the values comparable to the jet exit velocity U_J. In the second case, i.e. Case *OC2*, the same actuator configuration with different control frequency, i.e. $2\mathrm{St}_{pm}$, is considered. Additionally, for this case we superimposed a random component with a maximum magnitude of $0.005\mathcal{F}_0$ on every element of the forcing vector $\boldsymbol{\alpha}$.

The optimization results are summarized in Table 6.4 and illustrated in Figure 6.3 using normalized cost functionals and norm of the gradients. For both cases, the decrease in the cost functional saturates after a few iterations. We observed that (not shown here) each outer iteration corresponds on average to approximately 4 PDE solutions with DNS, where a PDE solution requires around 2500 CPU hours, as described above. Therefore, optimizations are stopped if a minimum reduction of around 5% is obtained and relative improvements in the cost functional at each outer iteration are found not cost-efficient. For Case *OC1*, a reduction of 10.5% is observed after 18 outer iterations. The norm of the gradient decreases from $\nabla\tilde{\mathcal{J}} \approx 1.2$ to $\nabla\tilde{\mathcal{J}} \approx 0.6$ showing that the local minimum is not reached yet. In the Case *OC2*, the cost functional is reduced around 5.6% after 9 outer iterations. In the final outer iteration, $\nabla\tilde{\mathcal{J}} \approx 0.4$, again showing that the local optimum is still not reached.

The relative reduction in the cost functional of Case *OC2* is lower compared to the one of Case *OC1*. Furthermore, this limited reduction is achieved by increasing the norm of the controls more than 3% where this increase is only 0.3% in Case *OC1* (cf. Table 6.4). This result suggests that the addition of a random component on the controls makes the problem more challenging for the optimizer. On the other hand, the final value of $\tilde{\mathcal{J}}$ in Case *OC2* is 10% less than the one of Case *OC1* thanks to the more efficient initialization, i.e., initialization with the double of the preferred mode increases the global sum of enstrophy more efficiently than the initialization with the preferred mode. This is in qualitative agreement with the discussion at the start of this chapter, where actuation with the preferred mode is claimed to be stabilizing the larger scales, and therefore inefficient for the smaller scale transition.

The resulting optimized control signals are first converted into the phase angle form, such that

$$\overline{\alpha}_n \cos(2\pi(nf_o)t + \varphi_n) = \alpha_{2n-1}\sin(2\pi(nf_o)t) + \alpha_{2n}\cos(2\pi(nf_o)t), \qquad (6.6)$$

and plotted subsequently on the polar axes $r = \overline{\alpha}_n/\mathcal{F}_0$ and $\theta = \varphi_n$ in Figure 6.4 and 6.5. Control regions that are $2\pi/3$ away from each other in the azimuthal direction, are plotted together, as their signals exhibit similar distributions.

The signals of the initially active forcing regions, i.e., *A0*, *A4*, *A8*, remain approximately unchanged after optimization, as we can see in Figure 6.4a and 6.5a. The optimized amplitudes in other regions remain in low magnitude compared to the initial forcing $\mathcal{F}_0$. Especially the neighbouring regions to *A0*, *A4*, *A8*, i.e., *A1*, *A5*, *A9* and *A3*, *A7*, *A11*, have the lowest energy content for both optimization cases, cf. Figure 6.4b,d and 6.5b,d. For these regions, the amplitudes of frequency components remains approximately below $0.02\mathcal{F}_0$ for Case *OC1* and $0.04\mathcal{F}_0$ for Case *OC2*. Moreover, there are no obvious trends in the distribution of phase angles. In contrast, for forcing regions *A2*, *A6*, *A10* in Figure 6.4c and 6.5c, phase angle values concentrate in the region $-\pi/4 < \theta + \pi < \pi/4$, which suggests a $\varphi_n \approx \pi$ out-of-phase behaviour with respect to the initially active actuators *A0*, *A4*, *A8*. Moreover, forcing in these regions, is more pronounced compared to regions neighbouring them. In Case *OC1*, the most amplified frequency component is $2\mathrm{St}_{pm}$ for the actuators *A2*, *A6*, *A10*, and its amplitude corresponds to approximately $0.04\mathcal{F}_0$ (cf. dashed circles in Figure 6.4c). Furthermore, the most amplified frequency component in Case *OC2* is $3\mathrm{St}_{pm}$ for the actuators *A2*, *A6*, *A10*, and with an amplitude that corresponds to approximately $0.08\mathcal{F}_0$ (cf. dashed circles in Figure 6.5c).

Figure 6.6 presents streamwise snapshots of $|\boldsymbol{\omega}|$ in Case *OC2* for initial and final optimized controls in the forcing plane of *A0*, i.e. a cutplane passing through the centroid of *A0*. Furthermore, Figure 6.7 illustrates the instantaneous snapshots of $|\boldsymbol{\omega}|$ on various cross-section planes. We observe that the distributed actuation is able to produce some characteristic primary and secondary vortex features of ZNMF actuated jets. At $x = D$, we see the cross section of a tilted vortex ring, which is marked with a solid line in Figure 6.6a. These asymmetric rings are typical for flows that lose their axisymmetry due to cross-stream perturbations, as discussed in Chapter 4. This primary vortex ring is unaffected by optimization and develops approximately with the same structure in the unoptimized flow as in the optimized flow (cf .Figure 6.6a and Figure 6.6b).

Looking further at the forcing plane of *A0* in Figure 6.6a, we note the presence of a streamwise vortex filament in the unoptimized flow (cf. dashed line). These secondary structures are first formed between the peak sides of primary rings (cf. Chapter 4 for a detailed discussion). A secondary structure is also evident in the optimized flow but somewhat less organized (see Figure 4.6b). This can be seen more clearly on the cross-section plane at $x/D = 2$ in Figure 6.7. For the unoptimized flow, a very regular characteristic hexagram pattern, which is produced by tilted vortex rings and streamwise vortex filaments, can be seen in Figure 6.7a. The same pattern appears also in the optimized flow but in a somewhat perturbed fashion (cf. Figure 6.7d). The differences between optimized and unoptimized flows increase moving downstream, as we can see on cutplanes at $x/D = 4$ in Figures 6.7b and 6.7e. The optimized jet develops the characteristic pattern of an azimuthally perturbed jet but has much more irregularity and has more vorticity content. At $x/D = 6$ in Figures 6.7c and 6.7f, we see three streamwise vortex pairs in a braid region, which are located at the corners of triangular patterns.

6.4 Conclusions

In this chapter, an enstrophy maximization study for an axisymmetric jet at $\mathrm{Re}_D = 2000$ was performed. The controls were modelled as twelve

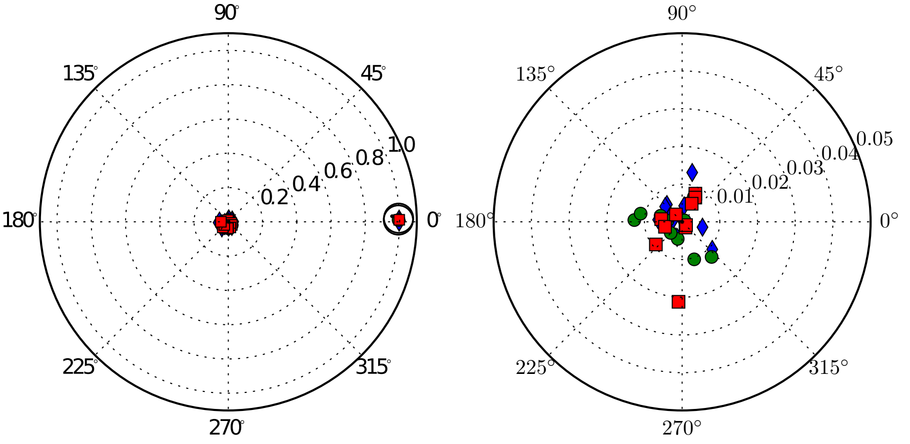

(a) *A0*, *A4*, *A8* (b) *A1*, *A5*, *A9*

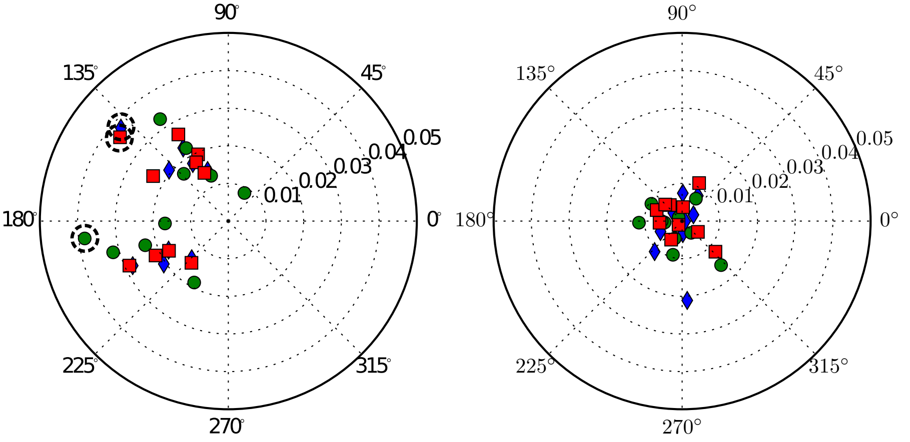

(c) *A2*, *A6*, *A10* (d) *A3*, *A7*, *A11*

Figure 6.4: Optimized controls for Case *OC1* using a polar graph with axes $r = \overline{\alpha}_n/\mathcal{F}_0$ and $\theta = \varphi_n$. (◇): regions *A0*, *A1*, *A2*, *A3*; (○): *A4*, *A5*, *A6*, *A7*; (□): *A8*, *A9*, *A10*, *A11*. The frequency information is not given. Only the frequency components with higher amplitude of forcing are marked by circles of (—): St_{pm} in (a); (−−): $2\mathrm{St}_{pm}$ in (c).

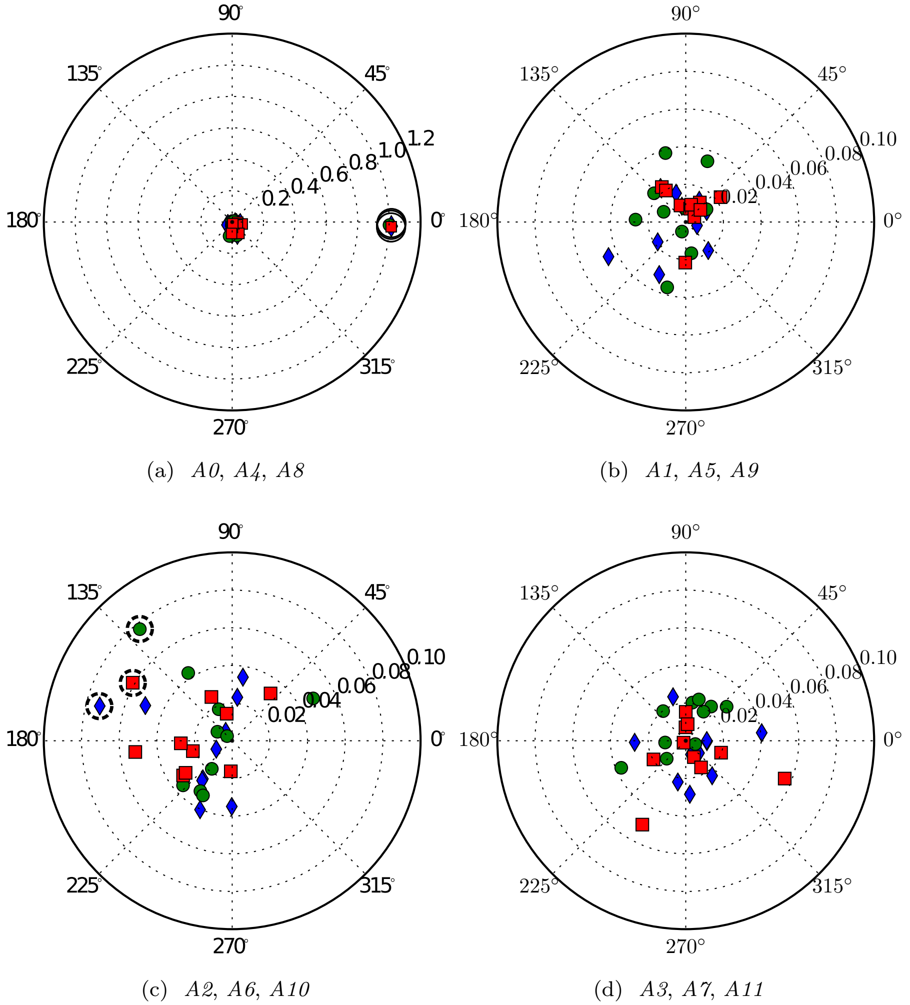

(a) *A0*, *A4*, *A8*
(b) *A1*, *A5*, *A9*
(c) *A2*, *A6*, *A10*
(d) *A3*, *A7*, *A11*

Figure 6.5: Distribution of the optimized controls for Case *OC2* using a polar graph with axes $r = \overline{\alpha}_n/\mathcal{F}_0$ and $\theta = \varphi_n$. See Figure 6.4 for captions. The frequency components with higher amplitude of forcing are marked by circles of (—): $2\mathrm{St}_{pm}$ in (a); (−−): $3\mathrm{St}_{pm}$ in (c).

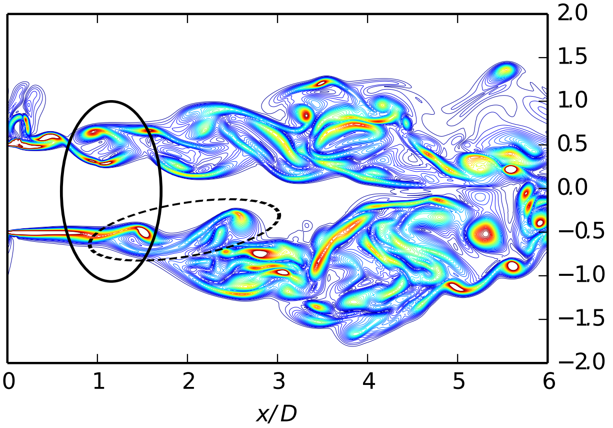

(a) iteration=0

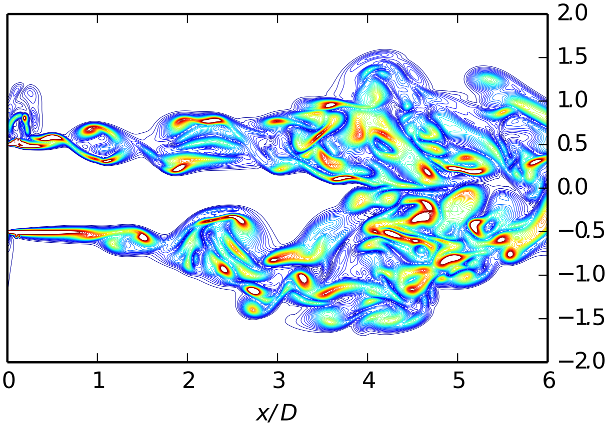

(b) iteration=9

Figure 6.6: Instantaneous snapshots of $|\boldsymbol{\omega}|$ on the forcing plane of *A0* for unoptimized (a) and optimized (b) jet flows in Case *OC2*.

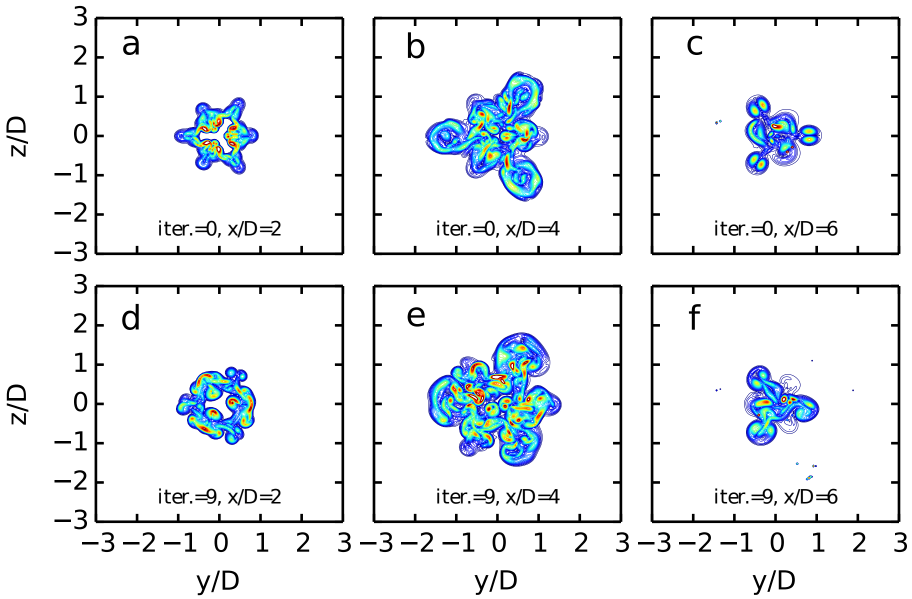

Figure 6.7: Instantaneous snapshots of $|\boldsymbol{\omega}|$ on various cross-section planes for unoptimized (a, b, c) and optimized (d, e, f) jet flows in Case *OC2*.

small hexahedral regions around the jet circumference with a uniform forcing distribution. Forcing is applied only in the radial direction. The signal of controls is designed as a finite Fourier series with 10 frequency components varying between $0.5\mathrm{St}_{pm}$ and $5\mathrm{St}_{pm}$. Optimization is carried out for these Fourier coefficients in the Fourier series, yielding a total size of 240 for the control space. The optimization method is the steepest descent method described in Algorithm 5.1 in Chapter 5. Two different initial conditions, referred to as Case *OC1* and Case *OC2*, are considered for optimization. These initial controls are inspired from Case *C1* and Case *C2* in Chapter 5, where three actuators are driven in phase with a frequency of St_{pm} and $2\mathrm{St}_{pm}$ respectively. For Case *OC2*, an additional random component with a low amplitude is added on every element of the control vector.

First of all, the directional accuracy of the adjoint-based gradient was verified by performing a comparative study using finite-difference based gradients. The gradients are evaluated only with respect to the Fourier coefficients of cosine components in the actuator *A0*. The tests were run for five different optimization horizons and required 60 PDE solutions in total. The direction of the adjoint-based gradients are in very good alignment with the direction of the finite-difference based gradients. In addition, we observed by calculating the norm of the gradients that the magnitude of adjoint-based gradients are lower than the magnitude of finite-difference based gradients. We believe that this is due to the fact that the high implicitness parameter ($\theta = 0.9$) employed in the adjoint equations introduces strong numerical diffusion.

Optimizations were conducted, and reductions of 10.5% and 5.6% are observed for Case *OC1* and Case *OC2* respectively. For both cases, the decrease in the cost functional saturated after a few iterations. Optimizations were stopped prematurely for resource reasons, before local optima were formally reached. The relative reduction in Case *OC2* was lower compared to the one of Case *OC1*. Furthermore, this limited reduction was achieved by increasing the magnitude of controls more than for Case *OC1*. We believe that this due to the fact that the addition of a random component on the controls makes the problem more challenging for the optimizer. The final value of enstrophy in Case *OC2* is 10% higher than the one of Case *OC1* thanks to the more efficient initialization with $2\mathrm{St}_{pm}$.

Finally, the optimized signals and fields are discussed. We observed that optimizations did not cause dramatic changes in the controls. Modifications were mainly minor, where low energy modifications (less than 10% of the initial forcing amplitude) are observed in forcing amplitudes of initially passive actuators. However, these minor changes in controls were capable of altering the evolution of the jets downstream as demonstrated by the snapshots of vorticity fields in Case *OC2*. In the optimized flow, primary and secondary vortex features were more unstable compared to the ones in unoptimized flow, and therefore the typical geometric patterns in jet-cross sections were more irregular.

Chapter 7

Conclusions and outlook

7.1 Summary of results

In this dissertation, we numerically studied a flexible, high-bandwidth active control method using ZNMF actuation to improve the mixing rate in axisymmetric jet flows. ZNMF actuation can be realized in the laboratory by using synthetic-jet actuators which are cheap, easy-built, lightweight control devices. The main challenge for the applicability of these fluidic actuators in jet-flow control is the very complicated interaction of the control means with the main jet flow. The understanding on control effects resulting from this interaction is still very limited. Therefore, the optimal configurations for best performance is still to be explored. We tackled this problem and first developed a numerical flow control and optimization framework in OpenFOAM®. Subsequently, we performed a set of high-fidelity DNS simulations of a low-speed round jet using various actuation frequencies. We identified typical flow patterns resulting from the control-main flow interaction and investigated the mechanisms generating these patterns. We demonstrated that the control effect is strongest when the jet is excited with natural jet frequency, also called the jet preferred mode, and strong large-scale vortices are produced. Such an actuation yields favourable changes in key mixing measures like entrainment and centreline decay rate. However, we noted that increased coherence in the flow delays the fine-scale transition and can be detrimental to molecular mixing. This result suggested a need for multi-frequency actuation in jet mixing. We addressed this issue by conducting an optimal control study with high-bandwidth control signals. To this end, we performed optimization with a gradient-based method, where gradients are calculated with the continous adjoint method. Optimized control signals are found to be composed of multi-frequency components, and they produced flow fields with slightly enhanced irregularity and mixedness. These primary results and computational efforts enabling them are discussed in more detail below.

During the first phase of this study, OpenFOAM®'s original solver for unsteady flows was found inefficient for the planned DNS simulations and an improvement regarding the time-stepping cost is made. OpenFOAM® employs a version of the PISO scheme for the segregated solution of incompressible Navier–Stokes simulations. This scheme requires an iterative solution of the Pressure–Poisson equation. In this study, it is replaced with a classical incremental projection scheme, which does not require any iterative solution. This projection scheme is implemented into OpenFOAM®and its second order temporal accuracy in velocity is verified using an analytical test case. Subsequently, it is employed in a DNS of round jet test case, and a 45% cost reduction in time-stepping is obtained.

Another challenge in DNS studies was OpenFOAM®'s limited applicability on high performance computing clusters due to its poor parallel scaling properties. OpenFOAM® employs a non-overlapping grid partitioning for parallel computations. This method suffers a communication overhead with increasing number of processors. This is demonstrated by a performance test using DNS of a round jet on the *Tier1* supercomputer of the Flemish Supercomputer Center (VSC). The parallel speed-up of OpenFOAM® strongly diverts from the ideal linear speed-up when the number of processors $p > 500$. In order to overcome this limitation a parallelization of statistical averaging in DNS simulations was proposed. The method is based on ensemble averaging applied on a set of statistically independent simulations. If the statistically independent set of simulations is constructed by imposing random perturbations on their initial mean fields, the approach leads to about 20% performance improvement on 624 processors.

Subsequently, Direct Numerical Simulations were carried out to study a moderate Reynolds number ($\mathrm{Re}_D = 2000$) axisymmetric jet subject to single frequency ZNMF actuation with a low momentum ratio. Three ZNMF actuators are distributed evenly in the circumferential direction and directed towards the main jet with an inclination angle of $\alpha = 30$ to the jet axis. We find that the ZNMF actuation leads to strong deformations of the near-field jet region that are very similar to those observed for non-circular jets. At the end of the jet's potential core ($x/D = 5$), the jet-column cross section is deformed into a hexagram-like geometry that results from strong modifications of the vortex structures. Two mechanisms lead to these modifications, i.e., (i) self-deformation of the jet's primary vortex rings started by distortions in their azimuthal curvature by the actuation, and (ii) production of side jets by the development and subsequent detachment of secondary streamwise vortex pairs. Further downstream ($x/D = 10$), the jet transforms into a triangular pattern, as the sharp corner regions of the hexagram entrain fluid and spread. We further investigated the global characteristics of the actuated jets. In particular when using the jet preferred frequency, i.e. $\mathrm{St}_D = 0.33$, parameters such as entrainment, centerline decay rate, and mean turbulent kinetic energy are significantly increased. Furthermore, high frequency actuation, i.e. $\mathrm{St}_D = 1.32$, is found to suppress the mechanisms leading to large-scale structure growth and turbulent kinetic energy production. The simulations further include a passive scalar equation, and passive scalar mixing is also quantified and visualized.

In order to explore the jet's response to an extended number of actuators with complicated control signals, an optimizer using a continuous adjoint methodology was developed in OpenFOAM®. To this end, a steepest-descent algorithm and the adjoint version of the incremental projection scheme are implemented. In the adjoint projection algorithm, the additional cross-convection term is treated with the Adams-Bashforth method, as OpenFOAM® does not support the implicit treatment of coupled velocity terms. It is found that this form $-u_j \partial \xi_j / \partial x_i$ of transposed-convection term delivers unstable results. Furthermore, using a 2D Bickley jet example, it is demonstrated that the adjoint method fails to provide gradient information in long time horizons for chaotic and noise-amplifier flows.

Finally, the developed optimization framework was applied to a transitional jet at $\mathrm{Re}_D = 2000$ by performing an enstrophy maximization study. The controls in this study were modelled as twelve small hexahedral regions in the domain, that are distributed evenly around the jet circumference with a uniform forcing distribution. Forcing is applied only in the radial direction. The signal of controls is designed as a finite Fourier series with 10 frequency components varying between $0.5\mathrm{St}_{pm}$ and $5\mathrm{St}_{pm}$. Optimization is carried out for coefficients in the Fourier series, yielding a total size of 240 for the control space. Two optimization cases with different initial conditions are considered. One of the cases contains an additional low magnitude random forcing component in its initial condition.

The directional accuracy of the adjoint-based gradient is tested first by performing a comparative study using finite-difference based gradients, and a very good agreement between both gradients is found. Subsequently, optimizations are conducted, and reductions of 10.5% and 5.6% are obtained for two different cases. For both cases, the decrease in the cost functional saturated after a few iterations. The case with an additional random forcing component has less reduction with higher energy control input. We believe that this inefficiency is caused by the additional random component producing more challenging optimization landscape. We further observed that optimizations did not impose dramatic changes in the controls. Modifications were mainly minor, where low energy modifications (less than 10% of the initial forcing amplitude) are observed in forcing amplitudes of initially passive actuators. Finally, it is demonstrated that minor changes in controls were capable of modifying the evolution of the jets downstream.

7.2 Suggestions for future research

7.2.1 Jet-flow control with ZNMF actuators

The results of this dissertation mark the versatility of ZNMF actuators by showing their effectiveness to promote or suppress turbulence in axisymmetric jet flows. Obviously the considered Reynolds number is low compared to many practical applications, and, e.g. mixing properties of turbulent jets are known to be Reynolds-number dependent [35]. Nevertheless, we have shown that the mechanisms creating strong side jets, are mainly inviscid, and therefore only a weak Reynolds number dependence is to be expected. Indeed, it is well appreciated in experiments with low-density jets, that side jet formation occurs for intermediate Reynolds number up to approximately $\mathrm{Re}_D = 25000$ [89].

For very high Reynolds numbers the noise amplifier nature of the jet becomes extremely dominant, and the growth of strong primary rings is inhibited as the jet becomes very sensitive to unorganized perturbations. Thus, our results remain only relevant for Reynolds number regimes where the formation of strong azimuthal rings can be achieved. Exploring these Reynolds-number regimes in more detail, e.g., using large eddy simulations, is an interesting subject of further study.

Furthermore, we mainly focused on the objective of jet-mixing enhancement, which requires the promotion of turbulence-generating mechanisms in the flow. In the case of high-frequency ZNMF actuation, we discussed also briefly the mechanisms suppressing the turbulence. The practical value of such an actuation remained unexplored. The inhibition of large-scale structure growth and turbulent kinetic energy production can be beneficial for suppressing the jet noise and enhancing the jet-thrust. Therefore, jet-flow control with high frequency ZNMF actuation is a promising area of research for future studies.

7.2.2 Adjoint-based optimal flow control

The optimization framework developed in this work is one of the very first for optimization of unsteady flows in generic geometries. It can be applied to numerous engineering and scientific cases. In the domain of jet flows, improving the hydrodynamic and thermodynamic properties in combustion chambers, nozzle exhausts or chemical processes can be very interesting applications. In order to employ this framework in such applications of engineering relevance, further evolution in computer resources is needed, and the following extensions are also required.

First of all, the framework supports only distributed controls due to the erroneous pressure boundary conditions imposed in the segregated projection solver. Therefore, an improved projection scheme with accurate pressure boundary conditions is required to solve optimal boundary control problems. To the authors knowledge, such a projection scheme does not exist yet, and therefore can be an exciting area of research. An alternative solution to this issue is implementing a coupled Navier-Stokes framework in OpenFOAM®. Such an extension will be also beneficial for the temporal discretization of the additional transposed-convection term.

Secondly, the adjoint solver in the framework only supports DNS solutions, and therefore does not contain any adjoint subgrid-scale models. As most of the engineering flows are high-Reynolds number, these models have to be derived for each application and verified. This derivation may not be straightforward if adjoint subgrid-scale terms are derived from advanced LES subgrid-scale terms using the continous adjoint method. Another option is developing original adjoint subgrid-scale models for the incompressible adjoint Navier–Stokes equations.

Furthermore, we discussed that adjoint-based gradients fail to predict sensitivities in longer time horizons because of chaotic behaviour of turbulence. This is an important limitation, as short time horizons may not efficiently represent the dynamics of interest in the flow. Developing methods to overcome this limitation is a highly exciting area of research. Lea et al. [79] initially proposed an ensemble-adjoint method for a chaotic system. Several researchers applied and extended this methodology afterwards. This method is relatively straightforward and based on calculating adjoint variables in an ensemble of simulations, and therefore allowing shorter time horizons. Very recently, Blonigan et al. proposed a Least-Squares Shadowing method [12]. The method is based on approximating the shadow trajectory in phase space, and preventing the high sensitivity to the initial conditions. This approach is very new, and therefore is subject to promising research.

In this work, we employed a simple steepest-descent method for the solution of the optimization problem. This method is known with its slow convergence to local optima. Therefore, more advanced optimization algorithms, e.g. the method proposed by Badreddine et al. [7], can be studied and integrated into the developed optimization framework. Badreddine et al. proposed an algorithm based on Sequential Quadratic Programming (SQP) in combination with a limited-memory BFGS method for the optimization of turbulent flows with DNS and LES, and demonstrated that an order of magnitude faster convergence compared to a conventional nonlinear conjugate-gradient method can be achieved with this method.

Finally, the optimization landscape in turbulent flow optimization studies can be highly non-convex. Therefore, solutions are strongly dependent on the selection of initial conditions, as gradient-based methods converge to local optima. In order to avoid this problem and improve the solutions in a global sense, a hybrid approach can be employed. In this approach, a globally convergent method, e.g. genetic algorithms, does initial iterations and its solution can be used as an initial condition for the gradient-based optimizer.

Bibliography

[1] Scotch. `http://www.labri.fr/perso/pelegrin/scotch/`. Accessed: 2014-10-02.

[2] J. S. Agashe, D. P. Arnold, and L. Cattafesta. Development of compact electrodynamic zero-net mass-flux actuators. In *47th AIAA Aerospace Sciences Meeting*, pages 2009–1308, 2009.

[3] J. C. Agüí and L. Hesselink. Flow visualization and numerical analysis of a coflowing jet: a three-dimensional approach. *Journal of Fluid Mechanics*, 191:19–45, 1988.

[4] V. Arakeri, A. Krothapalli, V. Siddavaram, M. Alkislar, and L. Lourenco. On the use of microjets to suppress turbulence in a Mach 0.9 axisymmetric jet. *Journal of Fluid Mechanics*, 490:75–98, 2003.

[5] H. Aref. Stirring by chaotic advection. *Journal of Fluid Mechanics*, 143:1–21, 1984.

[6] S. Badia and R. Codina. Algebraic pressure segregation methods for the incompressible Navier–Stokes equations. *Archives of Computational Methods in Engineering*, 15(3):1–52, 2007.

[7] H. Badreddine, S. Vandewalle, and J. Meyers. Sequential quadratic programming (SQP) for optimal control in direct numerical simulation of turbulent flow. *Journal of Computational Physics*, 256:1–16, 2014.

[8] C. Ball, H. Fellouah, and A. Pollard. The flow field in turbulent round free jets. *Progress in Aerospace Sciences*, 50(0):1 – 26, 2012.

[9] G. K. Batchelor. *An introduction to fluid dynamics.* Cambridge university press, 2000.

[10] L. Bernal and A. Roshko. Streamwise vortex structure in plane mixing layers. *Journal of Fluid Mechanics*, 170:499–525, 1986.

[11] T. R. Bewley, P. Moin, and R. Temam. DNS-based predictive control of turbulence: an optimal benchmark for feedback algorithms. *Journal of Fluid Mechanics*, 447:179–225, Nov. 2001.

[12] P. Blonigan, S. Gomez, and Q. Wang. Least squares shadowing for sensitivity analysis of turbulent fluid flows. *arXiv preprint arXiv:1401.4163*, 2014.

[13] B. Boersma, G. Brethouwer, and F. Nieuwstadt. A numerical investigation on the effect of the inflow conditions on the self-similar region of a round jet. *Physics of Fluids*, 10(4):899–909, 1998.

[14] C. Bogey and C. Bailly. Turbulence and energy budget in a self-preserving round jet: direct evaluation using large eddy simulation. *Journal of Fluid Mechanics*, 627:129–160, 2009.

[15] A. Borz and V. Schulz. *Computational optimization of systems governed by partial differential equations*, volume 8. SIAM, 2012.

[16] P. Brancher, J. Chomaz, and P. Huerre. Direct numerical simulations of round jets: vortex induction and side jets. *Physics of Fluids*, 6(5):1768–1774, 1994.

[17] R. Breidenthal. Structure in turbulent mixing layers and wakes using a chemical reaction. *Journal of Fluid Mechanics*, 109:1–24, 1981.

[18] G. L. Brown and A. Roshko. On density effects and large structure in turbulent mixing layers. *Journal of Fluid Mechanics*, 64:775–816, 6 1974.

[19] B. Callender, E. Gutmark, and S. Martens. Near-field investigation of chevron nozzle mechanisms. *AIAA Journal*, 46(1):36–45, 2008.

[20] B. Callender, E. J. Gutmark, and S. Martens. Far-field acoustic investigation into chevron nozzle mechanisms and trends. *AIAA Journal*, 43(1):87–95, 2005.

[21] C. Canuto, M. Y. Hussaini, A. Quarteroni, and T. A. Zang. *Spectral methods: evolution to complex geometries and applications to fluid dynamics*. Springer, 2007.

[22] D. Carati, M. Rogers, and A. Wray. Statistical ensemble of large-eddy simulations. *Journal of Fluid Mechanics*, 455:195–212, MAR 25 2002.

[23] T. Castelain, M. Sunyach, D. Juvé, and J.-C. Bera. Jet-noise reduction by impinging microjets: an acoustic investigation testing microjet parameters. *AIAA Journal*, 46(5):1081–1087, 2008.

[24] L. N. Cattafesta III and M. Sheplak. Actuators for active flow control. *Annual Review of Fluid Mechanics*, 43:247–272, 2011.

[25] H. Choi, M. Hinze, and K. Kunisch. Instantaneous control of backward-facing step flows. *Applied Numerical Mathematics*, 31(2):133–158, 1999.

[26] A. J. Chorin. Numerical solution of the Navier-Stokes equations. *Mathematics of Computation*, 22(104):745–762, 1968.

[27] A. J. Chorin. On the convergence of discrete approximations to the Navier-Stokes equations. *Mathematics of Computation*, 23(106):341–353, 1969.

[28] J. Citriniti and W. George. Reconstruction of the global velocity field in the axisymmetric mixing layer utilizing the proper orthogonal decomposition. *Journal of Fluid Mechanics*, 418:137–166, 2000.

[29] S. C. Crow and F. H. Champagne. Orderly structure in jet turbulence. *Journal of Fluid Mechanics*, 48:547–591, 7 1971.

[30] J. R. Debonis and J. N. Scott. Large-eddy simulation of a turbulent compressible round jet. *AIAA journal*, 40(7):1346–1354, 2002.

[31] S. Delport. *Optimal Control of a Turbulent Mixing Layer*. PhD thesis, KU Leuven, 2010.

[32] S. Delport, M. Baelmans, and J. Meyers. Constrained optimization of turbulent mixing-layer evolution. *Journal of Turbulence*, 10:18, 2009.

[33] S. Delport, M. Baelmans, and J. Meyers. Maximizing dissipation in a turbulent shear flow by optimal control of its initial state. *Physics of Fluids*, 23(4):045105, 2011.

[34] D. Demare and F. Baillot. The role of secondary instabilities in the stabilization of a nonpremixed lifted jet flame. *Physics of Fluids*, 13(9):2662–2670, 2001.

[35] P. E. Dimotakis. The mixing transition in turbulent flows. *Journal of Fluid Mechanics*, 409(1):69–98, 2000.

[36] P. E. Dimotakis, R. C. Miake-Lye, and D. A. Papantoniou. Structure and dynamics of round turbulent jets. *Physics of Fluids*, 26(11):3185–3192, 1983.

[37] R. E. Drubka and H. M. Nagib. Instabilities in near field of turbulent jets and their dependence on initial conditions and Reynolds number. Technical Report AFOSR-TR-82-0962, DTIC Document, 1981.

[38] J. Elliott and J. Peraire. Practical three-dimensional aerodynamic design and optimization using unstructured meshes. *AIAA Journal*, 35(9):1479–1485, 1997.

[39] J. H. Ferziger and M. Perić. *Computational methods for fluid dynamics*. Springer Berlin, 2002.

[40] H. Fiedler. Control of free turbulent shear flows. In M. Gad-el Hak and A. Pollard, editors, *Flow Control*, volume 53 of *Lecture Notes in Physics monographs*, pages 335–429. Springer Berlin / Heidelberg, 1998.

[41] J. B. Freund. Noise sources in a low-Reynolds-number turbulent jet at Mach 0.9. *Journal of Fluid Mechanics*, 438:277–305, 2001.

[42] D. Gaitonde and M. Samimy. Coherent structures in plasma-actuator controlled supersonic jets: Axisymmetric and mixed azimuthal modes. *Physics of Fluids*, 23:095104, 2011.

[43] M. B. Giles and N. A. Pierce. An introduction to the adjoint approach to design. *Flow, Turbulence and Combustion*, 65(3-4):393–415, 2000.

[44] A. Glezer and M. Amitay. Synthetic jets. *Annual Review of Fluid Mechanics*, 34(1):503–529, 2002.

[45] K. Goda. A multistep technique with implicit difference schemes for calculating two-or three-dimensional cavity flows. *Journal of Computational Physics*, 30(1):76–95, 1979.

[46] J. P. Goit and J. Meyers. Analysis of turbulent flow properties and energy fluxes in optimally controlled wind-farm boundary layers. In *Journal of Physics: Conference Series*, volume 524, page 012178. IOP Publishing, 2014.

[47] P. M. Gresho. On the theory of semi-implicit projection methods for viscous incompressible flow and its implementation via a finite element method that also introduces a nearly consistent mass matrix. part 1: Theory. *International Journal for Numerical Methods in Fluids*, 11(5):587–620, 1990.

[48] P. M. Gresho, R. L. Sani, and M. S. Engelman. *Incompressible flow and the finite element method: advection-diffusion and isothermal laminar flow*. Wiley New York, 1998.

[49] F. F. Grinstein. Vortex dynamics and entrainment in rectangular free jets. *Journal of Fluid Mechanics*, 437:69–101, 2001.

[50] F. F. Grinstein and C. DeVore. Dynamics of coherent structures and transition to turbulence in free square jets. *Physics of Fluids*, 8(5):1237–1251, 1996.

[51] J. Guermond, P. Minev, and J. Shen. An overview of projection methods for incompressible flows. *Computer Methods in Applied Mechanics and Engineering*, 195(44):6011–6045, 2006.

[52] M. Gunzburger. *Perspectives in Flow Control and Optimization.* Society for Industrial and Applied Mathematics, 2002.

[53] E. Gutmark and C.-M. Ho. Preferred modes and the spreading rates of jets. *Physics of Fluids*, 26(10):2932–2938, 1983.

[54] A. Hilgers and B. Boersma. Optimization of turbulent jet mixing. *Fluid Dynamics Research*, 29(6):345–368, 2001.

[55] M. Hinze, R. Pinnau, M. Ulbrich, and S. Ulbrich. *Optimization with PDE constraints.* Springer, New York, 2009.

[56] C. Hirsch. *Numerical Computation of Internal and External Flows: The Fundamentals of Computational Fluid Dynamics: The Fundamentals of Computational Fluid Dynamics*, volume 1. Butterworth-Heinemann, 2007.

[57] M. W. Hirsch, S. Smale, and R. L. Devaney. *Differential equations, dynamical systems, and an introduction to chaos.* Academic press, 2004.

[58] C.-M. Ho and P. Huerre. Perturbed free shear layers. *Annual Review of Fluid Mechanics*, 16(1):365–422, 1984.

[59] P. Huerre and M. Rossi. Hydrodynamic instabilities in open flows. In C. Godrèche and P. Manneville, editors, *Hydrodynamics and Nonlinear Instabilities*, pages 81–294. Cambridge University Press, 1998. Cambridge Books Online.

[60] J. C. R. Hunt, A. A. Wray, and P. Moin. Eddies, streams, and convergence zones in turbulent flows. In *Proceedings of the 1988 Summer Program*, pages 193–208, Dec. 1988.

[61] A. K. M. F. Hussain. Coherent structures and turbulence. *Journal of Fluid Mechanics*, 173:303–356, 11 1986.

[62] H. J. Hussein, S. P. Capp, and W. K. George. Velocity measurements in a high-Reynolds-number, momentum-conserving, axisymmetric, turbulent jet. *Journal of Fluid Mechanics*, 258:31–75, 1994.

[63] R. I. Issa. Solution of the implicitly discretised fluid flow equations by operator-splitting. *Journal of Computational Physics*, 62:40–65, Jan. 1986.

[64] R. James, J. Jacobs, and A. Glezer. Experimental investigation of a turbulent jet produced by an oscillating surface actuator. *Applied Mechanics Reviews*, 47(6S):S127–S131, 1994.

[65] H. Jasak. *Error analysis and estimation for the finite volume method with applications to fluid flows.* PhD thesis, Imperial College London (University of London), 1996.

[66] J. Jeong and F. Hussain. On the identification of a vortex. *Journal of Fluid Mechanics*, 285:69–94, 1995.

[67] R. Joslin, M. Gunzburger, R. Nicolaides, G. Erlebacher, and M. Hussaini. Self-contained automated methodology for optimal flow control. *AIAA Journal*, 35(5):816–824, 1997.

[68] R. D. Joslin and D. N. Miller. *Fundamentals and applications of modern flow control.* American Institute of Aeronautics and Astronautics, 2009.

[69] C. T. Kelley. *Iterative methods for optimization*, volume 18. Siam, 1999.

[70] J. Kim, D. J. Bodony, and J. B. Freund. Adjoint-based control of loud events in a turbulent jet. *Journal of Fluid Mechanics*, 741:28–59, 2014.

[71] J. Kim and H. Choi. Large eddy simulation of a circular jet: effect of inflow conditions on the near field. *Journal of Fluid Mechanics*, 620:383–411, 1 2009.

[72] J. Kim and P. Moin. Application of a fractional-step method to incompressible Navier–Stokes equations. *Journal of Computational Physics*, 59(2):308–323, 1985.

[73] K.-Y. Kim and S.-S. Kim. Shape optimization of rib-roughened surface to enhance turbulent heat transfer. *International Journal of Heat and Mass Transfer*, 45(13):2719–2727, 2002.

[74] S. Kimura and A. Bejan. The “heatline” visualization of convective heat transfer. *Transactions of the ASME: Journal of Heat Transfer*, 105:916–919, 1983.

[75] J. H. Konrad. *An experimental investigation of mixing in two-dimensional turbulent shear flows with applications to diffusion-limited chemical reactions.* PhD thesis, California Institute of Technology, 1977.

[76] L. D. Kral, J. F. Donovan, A. B. Cain, and A. W. Cary. Numerical simulation of synthetic jet actuators. *AIAA paper*, 1824:1997, 1997.

[77] O. A. Ladyzhenskaya and R. A. Silverman. *The mathematical theory of viscous incompressible flow*, volume 76. Gordon and Breach New York, 1969.

[78] J. C. Lasheras, A. Lecuona, and P. Rodriguez. Three-dimensional vorticity dynamics in the near field of coflowing forced jets. *Vortex Dynamics and Vortex Method, Lectures in Applied Mathematics*, 28:403–422, 1991.

[79] D. J. Lea, M. R. Allen, and T. W. N. Haine. Sensitivity analysis of the climate of a chaotic system. *Tellus A*, 52(5):523–532, 2000.

[80] S. K. Lele. Compact finite difference schemes with spectral-like resolution. *Journal of Computational Physics*, 103(1):16–42, 1992.

[81] D. Liepmann. *The near-field dynamics and entrainment field of submerged and near-surface jets.* PhD thesis, California Univ., San Diego, 1990.

[82] D. Liepmann and M. Gharib. The role of streamwise vorticity in the near-field entrainment of round jets. *Journal of Fluid Mechanics*, 245:643–668, 11 1992.

[83] S. Lin and G. Corcos. The mixing layer: deterministic models of a turbulent flow. part 3. the effect of plane strain on the dynamics of streamwise vortices. *Journal of Fluid Mechanics*, 141:139–178, 1984.

[84] G. Lipari and P. K. Stansby. Review of experimental data on incompressible turbulent round jets. *Flow, Turbulence and Combustion*, 87(1):79–114, 2011.

[85] D. Marinc and H. Foysi. Investigation of a continuous adjoint-based optimization procedure for aeroacoustic control of plane jets. *International Journal of Heat and Fluid Flow*, 38:200–212, 2012.

[86] J. E. Martin and E. Meiburg. Numerical investigation of three-dimensionally evolving jets subject to axisymmetric and azimuthal perturbations. *Journal of Fluid Mechanics*, 230:271–318, 1991.

[87] J. Meyers and C. Meneveau. Flow visualization using momentum and energy transport tubes and applications to turbulent flow in wind farms. *Journal of Fluid Mechanics*, 715:335–358, 0 2013.

[88] A. Michalke. Survey on jet instability theory. *Progress in Aerospace Sciences*, 21:159–199, 1984.

[89] P. A. Monkewitz, D. W. Bechert, B. Barsikow, and B. Lehmann. Self-excited oscillations and mixing in a heated round jet. *Journal of Fluid Mechanics*, 213:611–639, 1990.

[90] P. A. Monkewitz and E. Pfizenmaier. Mixing by side jets"in strongly forced and self-excited round jets. *Physics of Fluids*, 3(5):1356–1361, 1991.

[91] M. Mueller, L. Bernal, R. Moran, P. Washabaugh, B. Parviz, T. K. Chou, C. Zhang, and K. Najafi. Thrust performance of micromachined synthetic jets. In *Fluids 2000 Conference and Exhibit*, Reston, Virigina, Aug. 2000. American Institute of Aeronautics and Astronautics.

[92] I. Nastase and A. Meslem. Vortex dynamics and mass entrainment in turbulent lobed jets with and without lobe deflection angles. *Experiments in Fluids*, 48(4):693–714, 2010.

[93] G. Nathan, J. Mi, Z. Alwahabi, G. Newbold, and D. Nobes. Impacts of a jet's exit flow pattern on mixing and combustion performance. *Progress in Energy and Combustion Science*, 32(5–6):496 – 538, 2006.

[94] J. C. Neu. The dynamics of stretched vortices. *Journal of Fluid Mechanics*, 143:253–276, 1984.

[95] A. Önder and J. Meyers. Modification of vortex dynamics and transport properties of transitional axisymmetric jets using zero-net-mass-flux actuation. *Physics of Fluids*, 26(7):075103, 2014.

[96] OpenFOAM Foundation. *OpenFOAM- The Open Source CFD Toolbox, User Guide.*

[97] C. Othmer. A continuous adjoint formulation for the computation of topological and surface sensitivities of ducted flows. *International Journal for Numerical Methods in Fluids*, 58(8):861–877, 2008.

[98] J. M. Ottino. *The kinematics of mixing: stretching, chaos, and transport.* Cambridge University Press, 1994.

[99] L. G. Pack and A. Seifert. Periodic excitation for jet vectoring and enhanced spreading. *Journal of Aircraft*, 38(3):486–495, 2001.

[100] S. Pope. *Turbulent flows.* Cambridge University Press, 2000.

[101] J. J. Reuther, A. Jameson, J. J. Alonso, M. J. Rimlinger, and D. Saunders. Constrained multipoint aerodynamic shape optimization using an adjoint formulation and parallel computers, part 1. *Journal of Aircraft*, 36(1):51–60, 1999.

[102] W. C. Reynolds, D. E. Parekh, P. J. D. Juvet, and M. J. D. Lee. Bifurcating and blooming jets. *Annual Review of Fluid Mechanics*, 35(1):295–315, 2003.

[103] C. Rhie and W. Chow. Numerical study of the turbulent flow past an airfoil with trailing edge separation. *AIAA Journal*, 21(11):1525–1532, 1983.

[104] M. Samimy, J. Kim, J. Kastner, I. Adamovich, and Y. Utkin. Active control of high-speed and high-Reynolds-number jets using plasma actuators. *Journal of Fluid Mechanics*, 578(1):305–30, 2007.

[105] S. Scott Collis, R. D. Joslin, A. Seifert, and V. Theofilis. Issues in active flow control: theory, control, simulation, and experiment. *Progress in Aerospace Sciences*, 40(4):237–289, 2004.

[106] D. A. Tamburello and M. Amitay. Active control of a free jet using a synthetic jet. *International Journal of Heat and Fluid Flow*, 29(4):967 – 984, 2008.

[107] R. Temam. Une méthode d'approximation de la solution des équations de Navier-Stokes. *Bulletin de la Société Mathématique de France*, 96:115–152, 1968.

[108] R. Temam. Sur l'approximation de la solution des équations de navier-stokes par la méthode des pas fractionnaires (ii). *Archive for Rational Mechanics and Analysis*, 33(5):377–385, 1969.

[109] H. Tennekes and J. L. Lumley. *First Course in Turbulence*. MIT press, 1972.

[110] F. Thiesset, R. Antonia, and L. Djenidi. Consequences of self-preservation on the axis of a turbulent round jet. *Journal of Fluid Mechanics*, 748:R2, 2014.

[111] F. Tröltzsch. *Optimal control of partial differential equations: theory, methods, and applications*, volume 112. American Mathematical Soc., 2010.

[112] A. Tsinober. *An informal introduction to turbulence*. Springer, 2001.

[113] J. van Kan. A second-order accurate pressure correction scheme for viscous incompressible flow. *SIAM J. Sci. Stat. Comput.*, 7(3):870–891, July 1986.

[114] H. K. Versteeg and W. Malalasekera. *An introduction to computational fluid dynamics: the finite volume method*. Pearson Education, 2007.

[115] D. Violato and F. Scarano. Three-dimensional evolution of flow structures in transitional circular and chevron jets. *Physics of Fluids*, 23(12):124104, 2011.

[116] M. Wei and J. B. Freund. A noise-controlled free shear flow. *Journal of Fluid Mechanics*, 546:123–152, 2006.

[117] P. Wesseling. *Principles of computational fluid dynamics.* Springer Science & Business, 2009.

[118] S. E. Widnall and J. Sullivan. On the stability of vortex rings. *Proceedings of the Royal Society of London. A. Mathematical and Physical Sciences*, 332(1590):335–353, 1973.

[119] A. Yule. Large-scale structure in the mixing layer of a round jet. *Journal of Fluid Mechanics*, 89(03):413–432, 1978.

[120] K. Zaman, M. Reeder, and M. Samimy. Control of an axisymmetric jet using vortex generators. *Physics of Fluids*, 6:778, 1994.

Curriculum vitae

Asim Önder
Istanbul, Turkey, 1982.

Education

- October 2009 – December 2014, Ph.D. in Mechanical Engineering, KU Leuven, Belgium
- October 2006 – May 2009, Master in Computational Science and Engineering, TU München, Germany
- February 2002 – June 2006, Bachelor in Mechanical Engineering, Istanbul Technical University, Turkey

Experience

- October 2009 – September 2014, Doctoral researcher, teaching assistant at Numerical Techniques in Fluid Dynamics (2010-2014) and Numerical Modelling in Engineering (2013-2014), KU Leuven, Belgium
- July 2008 – December 2008, Student CFD engineer, InDeSa GmbH, Munich, Germany
- January 2007 – June 2008, Student software developer, Avionic Design Service, Munich, Germany
- August 2005 – June 2006, Intern, Daimler Chrysler, Istanbul, Turkey

Publications

International peer reviewed journal articles

- Önder, A., Meyers, J. (2014). Modification of vortex dynamics and transport properties of transitional axisymmetric jets using zero-net-mass-flux actuation, *Physics of Fluids*, 26, 075103.
- Önder, A., Meyers, J. (2014). Optimal control of a transitional jet using continuous adjoint method, *Computers and Fluids*, under review.

Papers at international scientific conferences and symposia

- Önder, A., Meyers, J. (2013). HPC realization of a controlled turbulent jet using OpenFOAM, *Proceedings of Open Source CFD International Conference 2013.* Hamburg, Germany.
- Önder, A., Wu, P., Meyers, J. (2012). Improving speed-up and efficiency in simulation of stationary turbulent flows by parallelization of statistical averaging, *Proceedings of 9th International ERCOFTAC Symposium on Engineering Turbulence Modeling and Measurements.* Thessaloniki, Greece.

Abstracts, presented at international scientific conferences and symposia

- Önder, A., Meyers, J. (2014). Optimal control of turbulent jets using an unsteady adjoint solver, 6th European Conference on Computational

Fluid Dynamics (ECFD VI). Barcelona, Spain.

- Önder, A., Meyers, J. (2012). DNS study of the active control of an axisymmetric jet with zero-net mass-flux (ZNMF) actuators, *the 9th European Fluid Mechanics Conference (EFMC9).* Rome, Italy.

FACULTY OF ENGINEERING SCIENCE
DEPARTMENT OF MECHANICAL ENGINEERING
DIVISION OF APPLIED MECHANICS AND ENERGY CONVERSION
Celestijnenlaan 300 box 2421
B-3001 Heverlee
Asim.Onder@kuleuven.be